NASA TECHNICAL REPORT

NASA TR R-369

C.1

NASA TR R-369

AN INVESTIGATION OF ATMOSPHERIC TURBULENCE BY STELLAR OBSERVATIONS

by Jack Lytle Bufton
Goddard Space Flight Center
Greenbelt, Md. 20771

NATIONAL AERONAUTICS AND SPACE ADMINISTRATION • WASHINGTON, D. C. • AUGUST 1971

1. Report No. NASA TR R-369	**2. Government Accession No.**	**3. Recipient's Catalog No.**

4. Title and Subtitle
An Investigation of Atmospheric Turbulence by Stellar Observations

5. Report Date
August 1971

6. Performing Organization Code

7. Author(s)
Jack Lytle Bufton

8. Performing Organization Report No.
G-1003

9. Performing Organization Name and Address
Goddard Space Flight Center
Greenbelt, Maryland 20771

10. Work Unit No.

11. Contract or Grant No.

12. Sponsoring Agency Name and Address
National Aeronautics and Space Administration
Washington, D.C.

13. Type of Report and Period Covered
Technical Report

14. Sponsoring Agency Code

15. Supplementary Notes
The information presented herein was submitted as a thesis in partial fulfillment of the requirements for the degree of Master of Science in Physics and Astronomy, University of Maryland, College Park, Maryland, 1970.

16. Abstract

This study of the optical effects of atmospheric turbulence concentrates on the stellar observation problem. When an infinite plane wave from an incoherent stellar source is sampled by an earth-based telescope, the resultant stellar image exhibits random fluctuations in intensity, position, and size due to turbulence-induced scattering in the intervening atmosphere. One familiar aspect of this problem is the scintillation of starlight apparent to the naked eye. The central aim is to express optical statistics in terms of refractive-index structure constant which pertains to strength of turbulence along the optical path. Data is presented on stellar and meteorological observations made between fall 1968 and spring 1969 with a 0.152-meter diameter refracting telescope. Data was recorded simultaneously on the three parameters of image intensity, motion, and size. The data is interpreted in terms of the theory and used to estimate strength of turbulence. The central result is a series of profiles for refractive-index structure constant along the vertical path. These are constructed using stellar data to calculate parameters of a model.

17. Key Words Suggested by Author
Scintillation
Turbulence
Atmospheric
Astronomy

18. Distribution Statement
Unclassified—Unlimited

19. Security Classif. (of this report)	**20. Security Classif. (of this page)**	**21. No. of Pages**	**22. Price***
Unclassified	Unclassified	175	3.00

*For sale by the National Technical Information Service, Springfield, Virginia 22151

TABLE OF CONTENTS

AN INVESTIGATION OF ATMOSPHERIC TURBULENCE BY STELLAR OBSERVATIONS*

by

Jack Lytle Bufton

Goddard Space Flight Center

CHAPTER I

INTRODUCTION

Light propagation through the atmosphere is a subject that until recently has received neither experimental nor theoretical treatment. Traditionally, the study of this phenomenon has been concentrated in astronomy where the collection of visible radiation from stellar sources is of utmost importance. Recently, the study of propagation has attracted the scientist interested in relating the physics of the atmosphere to observed effects, as well as the engineer interested in defining atmospheric limits for various optical systems. The advent of the laser and its implications for optical communication and ranging has spurred interest in the whole field of atmospherics.

Although to date there is no unified treatment of atmospheric effects at optical frequencies, several investigations have been partially successful in predicting experimental results. There exists a body of journal articles and research reports treating various propagation problems and estimating limits imposed by

---

*The information presented herein was submitted as a thesis in partial fulfillment of the requirements for the degree of Master of Science in Physics, University of Maryland, College Park, Maryland, 1970.

the atmosphere. The most important areas for future investigation lie in the relation of physical properties of the atmosphere to optical data and the determination of applicability and range of validity of the present theories. The purpose of this thesis research is to provide more information in the first area in order to shed some light on the second area. The approach is a study of a particular problem, the propagation of light from a star to an earth-based telescope receiver. Theoretical analysis is used to predict effects on starlight and experimental data is then used to evaluate the models and relationships behind this analysis.

At the outset an introduction to the physics of the problem is presented. This is followed by sample diffraction calculations for a thin layer of atmosphere and a more detailed introduction into the atmospheric physics. Statistical theories of recent years are then reviewed and the pertinent results for starlight propagation assembled. Where possible, formulae of other researchers are used intact. In several situations the theory must be extended or modified to more closely correspond to the experimental part of the thesis. In particular an analysis of stellar image intensity and motion-time behavior is presented here in a new form. A device developed at Goddard Space Flight Center to study stellar image quality in a telescope is used to provide quantitative data. Data is collected on stellar image intensity, motion, and size as observed in a 0.152-meter diameter refracting telescope.

The central contribution of the thesis research is the use of data to evaluate parameters of a model turbulence profile. Such a profile is of general interest to all researchers in the vertical propagation problem regardless of their specific optical systems. Data on stellar image intensity and image motion-time behavior is combined with upper altitude wind velocity and the theoretical analysis developed earlier to arrive at the model parameters. A concluding section discusses application of the model and directions for future research.

CHAPTER II

THEORETICAL BACKGROUND

Physics of the Problem, Part I

Optical propagation in the earth's atmosphere is influenced by absorbtion, molecular and aerosol scattering, and turbulence-induced scattering. The first two mechanisms result in effects that can be minimized by proper choice of locality and weather conditions for observations. In addition they are relatively stationary effects within a particular locality or in a period of several hours. The third mechanism, turbulence-induced scattering, results in the most serious optical problems from the viewpoint of this thesis. The turbulence process produces random fluctuations in refractive index along the optical path. This in turn distorts the phase or shape of the optical wavefront. After propagating a distance through the turbulent atmosphere an optical wavefront will exhibit phase and irradiance distortions. These distortions can change rapidly in magnitude over short periods of time and among different localities.

First attempts at solution of optical propagation problems, ranging from the work of Lord Rayleigh[1] to more recent investigators,[2,3] suggested that the observed optical effects may be explained by thin layers of turbulence in the atmosphere. Diffraction calculations relate optical effects to the statistics of the layers. In reality effects from many levels in the atmosphere are important in producing the observed results. Without considering, for the moment, the turbulence process in more detail, it is instructive to examine a highly simplified one-layer atmospheric model. Although far from rigorously correct, the single-layer model does develop the trends and reveal the optical physics involved.

Single-Layer Model

Consider the two-dimensional optical propagation problem, Figure 1, defined in the following manner. A unit amplitude plane wave (starlight) is incident upon a thin atmospheric layer that imparts a sinusoidal modulation to optical phase. The disturbed wave propagates to a ground-based telescope where an image is formed. The telescope is modeled by a one-dimensional aperture and thin diffraction limited lens. The quantities of interest are expressions for irradiance and phase of the wave in the aperture and image planes in terms of the various propagation parameters.

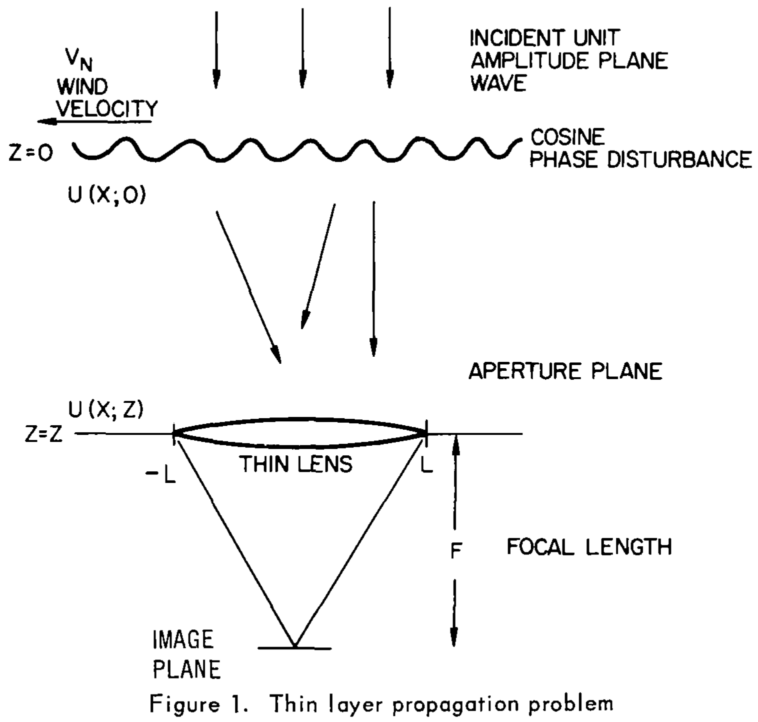

Figure 1. Thin layer propagation problem

The propagation parameters are as follows:

$\phi(x)$ = optical phase modulation imposed by thin layer

$\phi(x) = B \cos[2\pi(x/d + \Delta)]$

d = spatial wavelength of the phase pattern

$\Delta = \Delta(t)$ = relative phase

$\Delta = v_N t$

v_N = velocity of pattern (wind velocity)

B = depth of phase modulation

z = propagation distance from layer to aperture plane

$2L$ = aperture width

λ = optical wavelength

$k = 2\pi/\lambda$.

After passing through the phase modulation the plane wave disturbance is represented as follows:

$$U(x;0) = \exp[ikB \cos 2\pi(x/d + \Delta)]. \tag{1}$$

This can be written in terms of an infinite series using the Jacobi-Anger expansion,

$$U(x;0) = \sum_{m=-\infty}^{\infty} J_m(kB) \exp[2\pi im(x/d + \Delta + 1/4)].$$

The angular spectrum of $U(x;0)$ in terms of spatial frequency, f_x, is the Fourier transform of $U(x;0)$ as given by the expression

$$A_0(f_x) = \int_{-\infty}^{\infty} U(x;0) \exp(-2\pi i f_x x)\, dx \tag{2}$$

$$= \sum_{m=-\infty}^{\infty} J_m(kB) \exp[2\pi im(\Delta + 1/4)]\, \delta(f_x - m/d).$$

The angular spectrum, $A_z(f_x)$, after propagation the distance, Z, is just $A_0 \; (f_x)$ with phase delayed by the factor, $k\, z\, \sqrt{1-(\lambda f_x)^2}$,

$$A_Z(f_x) = A_0(f_x) \exp \left[i k z \sqrt{1-(\lambda f_x)^2} \right]. \tag{3}$$

The desired quantity is U(x; z), the complex disturbance in the aperture plane. This is the inverse Fourier transform of $A_Z \; (f_X)$.

$$U(x;\; z) = \int_{-\infty}^{\infty} A_0(f_x) \exp \left[i k z \sqrt{1-(\lambda f_x)^2} \right] \times \exp(2\pi i f_x x)\, d f_x \tag{4}$$

$$= \sum_{m=-\infty}^{\infty} J_m(kB) \exp[2\pi i m(\Delta + 1/4)].$$

$$\int_{-\infty}^{\infty} \delta(f_x - m/d) \exp \left[i k z \sqrt{1-(\lambda f_x)^2} \right] \times \exp(2\pi i f_x x)\, d f_x$$

$$= \sum_{m=-\infty}^{\infty} J_m(kB) \exp[2\pi i m(\Delta + 1/4)] \times \exp\left[i k z \sqrt{1 - \frac{\lambda m}{d}^{2}} \right] \exp\left(2\pi i \frac{x m}{d}\right).$$

The last result is obtained by substitution of equation (2) in equation (4) and performance of delta function integral. With the relations

$$J_{-n}(x) = (-1)^n J_n(x),$$

$$\sin x = \frac{\exp(ix) - \exp(-ix)}{2i},$$

and

$$\cos x = \frac{\exp(ix) + \exp(-ix)}{2},$$

U(x; z) can be rewritten

$$\begin{aligned} U(x;\ z) = {} & J_0(kB)\exp(ikz) \\ & + J_1(kB)\exp[ikz\ \ 1-(\lambda/d)^2]\cdot\times \\ & \qquad 2i\sin[2\pi(\Delta + 1/4 + x/d)] \\ & + J_2(kB)\exp[ikz\ \ 1-4(\lambda/d)^2]\times \\ & \qquad 2\cos[4\pi(\Delta + 1/4 + x/d)] \\ & + \cdot\ \cdot\ \cdot\ \cdot \end{aligned} \tag{5}$$

Under the assumption that the depth of phase modulation is much less than a wavelength, the argument of the Bessel functions is much less than one, that is,

$$kB = \frac{2\pi B}{\lambda} << 1.$$

Thus in the series expansion of U(x; z) only terms of order $(kB)^2$ or less should be retained. From the series expansions of the Bessel functions themselves, it is found that

$$\sum_{m=0}^{\infty} J_m (k\,B) \approx J_0 (k\,B) + J_1 (k\,B) + J_2 (k\,B),$$

where

$$J_0 (k\,B) \approx 1 - \left(\frac{k\,B}{4}\right)^2,$$

$$J_1 (k\,B) \approx k\,B/2,$$

and

$$J_2 (k\,B) \approx (k\,B/8)^2,$$

to order $(k\,B)^2$. An additional necessary assumption is that $\lambda/d << 1$, i.e., the wavelength of light is much, much smaller than the spatial wavelength of phase modulation. This is quite reasonable since the smallest dimensions of turbulent eddies are on the order of millimeters. Thus,

$$\sqrt{1 - (\lambda/d)^2} \approx 1 - \frac{1}{2} (\lambda/d)^2,$$

and

$$\sqrt{1 - 4\,(\lambda/d)^2} \approx 1 - 2\,(\lambda/d)^2.$$

Employing the above approximations, equation (5) results in

$$\begin{aligned} U(x;\ z) \approx \exp (i\,k\,z) \Bigg\{ 1 - \frac{k^2\,B^2}{4} & \qquad (6) \\ + k\,B\,i\ \cos\,[2\,\pi\,(\Delta + x/d)]\ \exp \left[- \frac{i\,k\,z}{2}\,(\lambda/d)^2\right] & \\ - \frac{k^2\,B^2}{4} \cos\,[4\,\pi\,(\Delta + x/d)]\ \exp\,[-\,i\,2\,k\,z\,(\lambda/d)^2] \Bigg\}. & \end{aligned}$$

Irradiance in the aperture plane is now formed, as follows:

$$I\ (x;\ z) = U^*\ (x;\ z)\ U(x;\ z)$$

$$I\ (x;\ z) = 1 - \frac{k^2\ B^2}{2} + 2\,k\,B\cos\left[2\,\pi\,(\Delta + x/d)\right]\left[\sin\frac{k\,z}{2}\,(\lambda/d)^2\right] \tag{7}$$

$$-\frac{k^2\ B^2}{2}\cos\left[4\,\pi\,(\Delta + x/d)\right]\cos\left[2\,k\,z\,(\lambda/d)^2\right]$$

$$+\frac{k^2\ B^2}{2} + \frac{k^2\ B^2}{2}\cos\left[4\,\pi\,(\Delta + x/d)\right].$$

To proceed further a small-angle requirement is imposed. Thus,

$$k\ z\ (\lambda/d)^2 < \pi/10,$$

$$\sin\left[k\ z\ (\lambda/d)^2\right] \approx k\ z\ (\lambda/d)^2,$$

and

$$\cos\left[k\ z\ (\lambda/d)^2\right] \approx 1.$$

For $z = 10$ meters and $\lambda = 0.5$ micron this forces d to be greater than one millimeter. For $z = 10$ kilometers and $\lambda = 0.5$ micron d must be greater than 10 centimeters. Thus the spatial wavelength, d, which corresponds to turbulence dimensions, must be larger than a certain minimum size which is near a millimeter at the earth's surface and rises to approximately a meter at the edge of the atmosphere. The data or estimates available on minimum turbulence sizes as a function of altitude suggest that these requirements are reasonable. Thus $I\ (x; z)$ reduces to

$$I\,(x;\ z) \approx 1 + \frac{4\pi^2 B z}{d^2} \cos\,[2\pi\,(\Delta + x/d)]\,. \tag{8}$$

The original sinusoidal modulation of phase has resulted in a sinusoidal irradiance modulation in the aperture. The depth of this modulation is

$$\frac{4\pi^2 B z}{d^2}$$

and thus increases with growth of z and B and decreases for larger pattern sizes at a given z.

Total intensity in the image is found by integration over the aperture as follows:

$$\begin{aligned} I_{TOT} &= \int_{-L}^{+L} I\,(x;\ z)\,dx \\ &= 2L + \frac{8\pi B z}{d} \cos\,(2\pi\Delta)\,\sin\left(\frac{2\pi L}{d}\right). \end{aligned} \tag{9}$$

Restriction to the dimensions of the aperture introduces the additional term

$$\sin\frac{2\pi L}{d}$$

that acts as an aperture-averaging term. Changes in 2L, the aperture size, are not as important in effecting I_{TOT} where $2/d >> 1$ as when $L/d \approx 1$. I_{TOT}, like I(x; z), is actually a function of time through the dependence of Δ on time,

$$\Delta = v_N\, t = \Delta\,(t)\,.$$

Thus, the frequency of image intensity variations (scintillation) is directly proportional to wind velocity at the particular altitude, z, of the phase modulation layer.

This same type of analysis can be applied to arrive at an expression for optical phase in the aperture plane. Together with irradiance information, a transformation to the image plane can then be made with the Fraunhofer diffraction approximation. The interesting quantities of image size, image motion, and their respective time dependences can be computed in terms of the initial propagation parameters. The interested reader is referred to the work of Ratcliffe[2] and Ramsay[4] for detailed treatments in this area. This analysis will not be presented here. Instead a presumably more accurate analysis based on current theories of propagation and the actual structure of turbulence is presented in Chapter III. Although inaccurate for specific results, the foregoing analysis is not without merit. As irradiance behavior in the aperture plane is again discussed in Chapter III in light of current theories, many of the concepts developed from the simple one-layer model will be recognized.

Physics of the Problem, Part II

Atmospheric optical index of refraction, N, is not sensibly affected by pressure independent of its change in density. In the visible region there is a weak dependence on wavelength. The following equation expresses these dependencies and includes empirical constants established[5] for the visible range of the spectrum:

$$N(\rho; \lambda) = 1.0 + \frac{\rho}{\rho_0}\left(288 + \frac{1.34}{\lambda^2}\right) \times 10^{-6}, \qquad (10)$$

where

ρ = atmospheric density,

ρ_0 = (standard temperature and pressure) density of dry air,

and

λ = optical wavelength in microns.

Atmospheric density at a given point undergoes rapid, small fluctuations around a relatively steady mean value. This is a result of turbulence mixing the air. The causal phenomenon for turbulence may be thermal or mechanical. Detailed analysis of these mechanisms is left to the meteorologist or atmospheric physicist. From the optical standpoint the important points are that turbulence results in quite serious optical problems and that its structure can be described with some success.

In typical turbulence, generation energy is input to the atmosphere in large-scale structures, with dimensions of meters or larger. Energy is then transferred to smaller and smaller turbulent eddies with little energy loss until finally it is dissipated into heat in the smallest eddies (dimensions near one millimeter at the earth's surface). Turbulence characteristics between these ill-defined outer, L_0, and inner, ℓ_0, scales which make up the "inertial subrange" can be treated in a reasonable fashion.

It is evident from the random nature of turbulence-induced fluctuations that a statistical approach is called for. The primary statistic of the random field is the structure function, defined as the mean square difference of a quality of the field for two points separated a distance $\vec{r}$. If the field can be considered homogeneous and isotropic the structure function depends only on the magnitude, $|\vec{r}|$, of $\vec{r}$. This will be denoted simply by r.

Analysis due to Obukhov[6] and Kolmogorov[7] concludes, primarily on the basis of dimensionality arguments, that the structure function for velocity fluctuations in the inertial subrange can be written

$$D_v (r) = \left\langle [v (\vec{r}_1) - v (\vec{r}_2)]^2 \right\rangle$$

$$= c (\epsilon r)^{2/3} , \qquad \ell_0 << r << L_0 ,$$

where

$D_v (r)$ = velocity structure function ,

r = separation of measurement points 1 and 2,

and

ϵ = energy dissipation rate per unit volume.

Associated with D_v (r) is its Fourier transform, F_v (κ), the velocity spectrum. In three dimensions F_v (κ) is proportional to $\kappa^{-11/3}$, where $\vec{\kappa}$ is a spatial frequency vector. This formulation has been verified experimentally[8,9] by measurements of small-scale velocity and temperature fluctuations in atmospheric surface layers and shown to be generally independent of the mechanism used to generate the turbulence. However, density, not velocity, is the important parameter from the optical viewpoint. One step away from density fluctuations and, thus, refractive is the temperature structure function, D_T(r). Obukhov concluded that D_T (r) can be written in a form similar to D_v (r). Thus,

$$D_T (r) = C_T^2 r^{2/3} , \qquad \ell_0 << r << L_0 , \tag{11}$$

where

C_T^2 = temperature structure constant.

Temperature and density statistics are directly related since the atmosphere will not support local pressure gradients. Warm segments of air are less dense than similar segments of cold air at the same altitude. Typical temperature fluctuations are less than a few tenths of a degree centigrade. The resulting density changes are of the order of hundreds of a mg/cm^3 and refractive index fluctuates by one part in 10^{-6}. The additive effect of many small changes of N (ρ; λ) along the optical path can result in serious wavefront distortion at the receiver.

Mathematically the connection is as follows. The variation, $\Delta\rho$, in density (at constant pressure) resulting from a small variation in temperature, ΔT, is

$$\Delta\rho = \frac{p}{R\Delta T}$$

from the ideal gas law. Further, since

$$\lim_{\Delta T \to 0} \frac{\Delta\rho}{\Delta T} = -\frac{p}{RT^2} = -\frac{\rho}{T},$$

then,

$$\Delta\rho \approx -\frac{\rho}{T}\Delta T.$$

From equation (10) the effect on refractive index of a small change in density, $\Delta\rho$, can be observed. Thus,

$$\Delta N(\rho;\lambda) = 1.0 + \frac{\Delta\rho}{\rho_0}\left(288 + \frac{1.34}{\lambda^2}\right) \times 10^{-6}.$$

Statistics of ΔN and ΔT are thus connected by the equation

$$\Delta N(\rho;\lambda) = 1.0 - \frac{\rho}{\rho_0}\frac{\Delta T}{T}\left(288 + \frac{1.34}{\lambda^2}\right) \times 10^{-6}. \qquad (12)$$

Structure functions relating N and T go as the square of ΔN and ΔT. Thus the two structure constants are related in the following manner:

$$C_N^2 = \frac{\rho}{\rho_0 T}\left[288 + \frac{1.34}{\lambda^2} \times 10^{-6}\right]^2 C_T^2, \qquad (13)$$

where

$$D_N^2 (r) = C_N^2 \, r^{2/3}, \qquad \ell_0 \ll r \ll L_0 . \tag{14}$$

These equations are the important results from turbulence theory. They relate the statistics of refractive index to a strength of turbulence factor, C_N^2 , and in turn to the strength of temperature fluctuations, C_T^2.

In the foregoing analysis isotropy has been assumed. For separations, r, well within the inertial subrange and at the same altitude this is not a bad assumption. Strength of turbulence, C_N^2, takes on different values as a function of altitude due to changes in absolute density, absolute temperature, and the strength of temperature fluctuations. For vertical propagation problems, altitude dependence must be taken into account. This is accomplished by assuming local isotropy at a given altitude, retaining the "2/3" law for D_N (r), and considering C_N^2 to be C_N^2 (h), a smoothly varying function of altitude, h, as follows:

$$D_N (r; h) = C_N^2(h) \, r^{2/3}, \qquad \ell_0 \ll r \ll L_0 . \tag{15}$$

Similarly sizes of inner and outer scales vary with altitude. The inner scale is thought to attain its smallest value near the ground and increase approximately as $h^{+1/3}$. The outer scale is less well understood but may be approximated by

$$L_0 \approx 2h^{1/2},$$

where

h = height in meters .

These rough values for ℓ_0 and L_0 were obtained from Hufnagel[10] and Fried[11]. Various estimates and data are also available on the C_N^2 (h) profile. These are presented as an introduction to Chapter V.

Finally, it must be noted that there exist turbulence regimes (particularly at night near the earth's surface under conditions of low wind) where the existence of an inertial subrange and the applicability of the "2/3" law are questionable. In these regimes there is insufficient energy input to have well-developed turbulence. For altitudes above the surface layer the existence of high Reynolds number flow and the associated well-developed turbulence argue for the existence of inertial subrange.

Introduction to Current Theories

Expression of optical effects in terms of the statistics of refractive index has been the subject of many current theoretical treatments. Since the earlier work in diffraction from single layers, researchers have employed geometrical optics and approximate solutions to the wave equation. In geometrical optics the usual starting point is integration of the "ray equation" as in Chernov[12], Beckmann[13], and Hodara[14]. Along the way, assumptions of no diffraction and small-angle scattering are made. Range of validity of this approach is restricted to the turbulence pattern near field. Since ℓ_0, inner scale of turbulence, is the smallest dimension of the pattern, the range constraint can be expressed

$$\ell_0 \gg \sqrt{\lambda z} \, ,$$

where

z = range of validity.

This is quite a severe constraint, of the order of a few meters near the ground. Recently a few authors, notably Taylor[15], have indicated that geometrical optics may apply for longer ranges, at least for predicting optical phase statistics. If a Gaussian form for refractive index structure function is assumed, the theory lends itself to use of geometrical optics. This is where considerable effort has been placed in the past. Here the important parameter becomes a correlation length, L_c, intermediate in length between ℓ_0 and L_0. Much evidence cited previously suggests that the Obukhov-Kolmogorov (OK) theory is more applicable especially near the earth's surface. In addition, geometric optics results for the Gaussian case have been shown to be somewhat in error by Kerr[16]. Application of geometrical optics and the OK turbulence spectrum to stellar observations is presented by Rieger[17] and discussed further by Young[18].

The most successful treatments of optical propagation through turbulence have been achieved by approximate solutions of the scalar wave equation

$$\nabla^2 u(\vec{r}) + k^2 N^2(\vec{r})\, u(\vec{r}) = 0. \tag{16}$$

For a plane wave incident on the turbulence, as in the case of starlight at the top of the earth's atmosphere, the complex field distribution is written

$$u(\vec{r}) = A(\vec{r}) \exp[i k \phi(\vec{r})]$$

or

$$u(\vec{r}) = \exp[\ln A(\vec{r}) + i k \phi(\vec{r})]. \tag{17}$$

As this disturbance propagates through the atmosphere it is randomly perturbed in a multiplicative manner. The end result is a product, not a sum, of the many intermediate actions of randomly fluctuating refractive index. Terms in the exponent of equation (17) are effected in an additive manner. As a consequence of the central limit theorem these terms should have a Gaussian distribution. Thus the conclusion follows that log-amplitude and phase obey Gaussian statistics.

Of the wave equation treatments use of the so-called "Rytov approximation" has achieved preeminence. The basis of this approximation is the neglect of a small term in the wave equation after the expression (17) is substituted in. This transforms it into a linear equation which can be solved for the desired optical statistics. Principal investigators of this method are Tatarski[19] and

Fried[20]. There is extensive literature devoted to these mathematical efforts. For a full mathematical treatment the interested reader is referred to Tatarski's "source book". While arguments are still raging over the validity of this method, it has been verified experimentally [21,22] at least for scintillation over ranges beyond the geometrical optics limit. Both American and Russian experimenters have, however, reported saturation effects for long paths and/or high turbulence conditions near the ground. For vertical propagation no such saturation effects have been observed and it is felt that the theory holds well. As with other optical propagation theories direct confirmation eludes the observer since the theory is really a two-step process. First the optical statistics of interest must be related to refractive index statistics of the field of turbulence, such as in the Rytov approach. Then the turbulence process must be adequately described. An error in either or both would have an adverse effect on the prediction of experimental data. This is especially true for the vertical case where the strength of turbulence changes with altitude.

Another school of investigators, notably Beran[23] and Hufnagel[24], while working from the wave equation, have modified it to a differential equation in statistics. Averages are taken before the equation is solved. The end result is a mutual coherence function for the atmosphere. This can be directly expressed in terms of Tatarsksi's wave structure function. Thus, at least in the area of average wavefront degradation, the two principal methods achieve the same end result. Once again prediction of experimental data depends on the form of the wave structure function. This in turn depends on the representation of turbulence.

In the following chapter results of theories applicable to stellar observations will be discussed. In several cases the present theory must be extended or modified.

CHAPTER III

ANALYSIS OF STELLAR IMAGE EFFECTS

Image Intensity

Total image intensity results from the irradiance pattern of starlight sampled by the telescope aperture. Irradiance varies with both position and time in the aperture plane. As indicated in Chapter II the quantity log-amplitude should obey Gaussian or normal statistics. Thus irradiance should have a log-normal behavior. Log-amplitude is defined in terms of irradiance, by the equation

$$\ell(\vec{x}, t) \equiv \frac{1}{2} \log_e \frac{I(\vec{x}, t)}{I_0}, \tag{18}$$

where

$\ell(\vec{x}, t)$ = instantaneous log-amplitude at position $\vec{x}$ in the aperture plane,

$I(\vec{x}, t)$ = corresponding irradiance at $\vec{x}$,

and

I_0 = ensemble average of $I(\vec{x}, t)$

$= \langle I(\vec{x}, t)\rangle$.

Variance of log-amplitude, σ_ℓ^2, has been shown[25] to equal the negative of average log-amplitude

$$\sigma_\ell^2 = -\langle \ell(\vec{x}, t)\rangle$$

under the assumptions of Gaussian statistics for log-amplitude and conservation of energy. A theoretical expression for σ_ℓ^2 has been proposed by Tatarski[19] on the basis of the Rytov approximation and Kolomogov turbulence spectrum. Thus,

$$\sigma_{\ell}^{2} = .56\ k^{7/6}\ \sec\theta^{11/6} \int_{0}^{\infty} C_{N}^{2}(h)\ h^{5/6}\ dh, \qquad (19)$$

where

k = optical wave number = $\frac{2\pi}{\lambda}$,

θ = stellar zenith angle,

and

$C_N^2(h)$ = refractive index structure constant as a function of altitude, h.

This formulation is also conditioned on an infinite plane-wave source (starlight) and a point detector. A telescope with small aperture such that instantaneous irradiance is constant over the aperture can be considered a point detector. The predicted wavelength dependence contained in $k^{7/6}$ is such that σ_{ℓ}^{2} is reduced by 20 percent in passing from $\lambda = 0.45\mu$ to $\lambda = 0.55\mu$. While σ_{ℓ}^{2} is reduced in magnitude at the higher wavelength, analysis[26] has shown that spectral correlation of σ_{ℓ}^{2} remains high for this separation of wavelengths.

Secant of zenith angle is simply the air mass through which starlight must pass before reaching the telescope. The above 11/6 power dependence has been shown to break down for large zenith angles when detection is not made under monochromatic conditions. A recent study[18] has attributed this to the increasing role of chromatic dispersion for large θ. Under such conditions different wavelengths of starlight suffer varying degrees of refraction in the atmosphere so that they follow different paths through spatially uncorrelated turbulence. The end result is a saturation-like effect for σ_{ℓ}^{2} at large θ. Dependence on strength of turbulence, $C_N^2(h)$, involves the 5/6 moment of altitude. Thus altitudes where

$$\int_{0}^{\infty} C_{N}^{2}(h)\ h^{5/6}\ dh$$

has its largest values are most important in determining σ_{ℓ}^2. The significance of this important relationship will be discussed in Chapter V.

A photomultiplier tube or other square-law device is normally used in field work to obtain data on the stellar image. Electric current out of this device is proportional to irradiance, not amplitude. Thus it is sometimes more convenient to handle the data in terms of irradiance statistics. The connection with log-amplitude statistics is easily made. Let the ratio of rms image intensity fluctions to their average value be the fundamental measure of irradiance statistics. This ratio, here called CIV, is the coefficient of irradiance variation. Thus,

$$\mathrm{CIV} = \frac{\sigma_I}{I_0}, \tag{20}$$

where

$$\sigma_I^2 = \text{irradiance variance}$$
$$= \langle (I - I_0)^2 \rangle .$$

Noting that

$$\ell = \frac{1}{2} \log_e \frac{I}{I_0}$$

and, thus,

$$I = I_0 \exp(2\ell), \tag{21}$$

σ_I^2 can be written

$$\sigma_I^2 = \langle [I_0 \exp(2\ell) - \langle I_0 \exp(2\ell) \rangle]^2 \rangle$$
$$= I_0^2 \langle [\exp(2\ell) - \langle \exp(2\ell) \rangle]^2 \rangle ,$$

where

$$\langle \exp(2\ell) \rangle = \exp[2\langle \ell \rangle + 2 \langle (\ell - \langle \ell \rangle)^2 \rangle]$$
$$= \exp[2\langle \ell \rangle + 2\sigma_{\ell}^2]$$
$$= 1, \text{since } \langle \ell \rangle = -\sigma_{\ell}^2 .$$

The last result follows from the Gaussian behavior of ℓ. Likewise,

$$\begin{aligned}\langle \exp(4\ell)\rangle &= \exp[4\langle \ell\rangle + 8\sigma_\ell^2] \\ &= \exp(4\sigma_\ell^2)\end{aligned}$$

and

$$\begin{aligned}\sigma_I^2 &= I_0^2 \,\langle [\exp(2\ell) - 1]^2\rangle \\ &= I_0^2 \,\langle \exp(4\ell) - 2\exp(2\ell) + 1\rangle \\ &= I_0^2 \,[\exp(4\sigma_\ell^2) - 1] .\end{aligned}$$

The ratio σ_I^2/I_0^2 is just CIV². Thus,

$$CIV^2 = \exp(4\sigma_\ell^2) - 1 . \qquad (22)$$

In actual experimental situations where equipment dynamic range or small departures from Gaussian behavior must be accounted for, the use of this equation is questionable[27]. For values of $\sigma_\ell^2 < 0.05$ where there is little difference between the normal and log-normal distributions the equation may be used safely, however. Furthermore, for these smaller values an approximation to equation (22) can be employed as follows:

$$\begin{aligned}CIV^2 &= \exp(4\sigma_\ell^2) - 1 \\ CIV^2 + 1 &= \exp(4\sigma_\ell^2) \\ \ln(CIV^2 + 1) &= 4\sigma_\ell^2 \\ &= CIV^2 - \frac{CIV^4}{2} + \frac{CIV^6}{3} - \cdots .\end{aligned}$$

For

$$CIV^2 < 1,$$

$$\ln(CIV^2 + 1) \approx CIV^2 .$$

Therefore,

$$CIV^2 \approx 4\sigma_\ell^2 . \qquad (23)$$

Experimental studies of starlight almost invariably employ telescopes of aperture dimension larger than several tens of centimeters. These optical systems cannot be considered point detectors. In the experimental phase of this thesis the aperture is circular and unobstructed with a diameter of 15.2 centimeters. This is intermediate between the point detector and a typical astronomical telescope of a meter or more in diameter. As diameter increases the strength of image intensity fluctuations, measured either by σ_{ℓ}^2 or CIV, decreases, slowly at first and then more rapidly as the spatial correlation distance of irradiance in the aperture plane is exceeded. In addition, the frequency content and zenith-angle dependence of the fluctuations are altered.

The interesting statistic now becomes covariance rather than variance. Covariance of log-amplitude, $\sigma_{\ell}^2(\rho)$, and covariance of irradiance, $\sigma_{I}^2(\rho)$, are functions of aperture plane dimension, ρ , where

$$0 \leq \rho \leq D$$

and

$$D = \text{aperture diameter} .$$

Explicit covariance results for the starlight propagation problem, based on the Rytov approximation and Obukhov-Kolmogorov turbulence spectrum, are limited to those of Fried[28]. He has achieved results only by assuming a specific form for $C_N^2(h)$ as a function of altitude. More general results corresponding to equation (19) are unavailable. The work of Fried and others, notably Tatarsksi[19] and Yura and Lutomirski[29] still provides a solid basis for understanding the problem. They all suggest that the aperture averaging effect can be described by a functional dependence involving diameter, D, correlation distance, $\sqrt{\lambda z}$, and strength of fluctuations for the point detector case. Thus the variances for log-amplitude and irradiance measured with a telescope of diameter, D , can be written

$$[\sigma_{\ell}^2]_D = A_{\ell} \left[\frac{D}{\sqrt{\lambda z}} ; \sigma_{\ell}^2(0)\right] \sigma_{\ell}^2(0)$$

$$\left[\frac{\sigma_I^2}{I_0^2}\right]_D = A_I \left[\frac{D}{\sqrt{\lambda z}} ; \frac{\sigma_I^2(0)}{I_0^2}\right] \frac{\sigma_I^2(0)}{I_0^2}$$

or

$$[\mathrm{CIV}^2]_D = A_I \left[\frac{D}{\sqrt{\lambda z}} ; \ \mathrm{CIV}^2\right] \mathrm{CIV}^2 . \tag{24}$$

The correlation distance, $\sqrt{\lambda z}$, is expressed as $\sqrt{\lambda H_0 \sec \theta}$ for stellar observations at zenith angle, θ. Altitude, H_0, can be considered a scale height for the atmosphere, the altitude below which most of the distortion-causing turbulence lies. The factor $\sqrt{\lambda z}$ arises from the relation of two-dimensional spectral density of amplitude, $F_A(\kappa)$, to three-dimensional spectral density of the structure function of refractive index, $\Phi_N(\kappa)$. As given by Tatarski[19] this relation is

$$F_A(\kappa) \approx 2\pi k^2 \int_0^\infty c_N^2(z)\, \Phi_N(\kappa) \sin^2\left(\frac{\kappa^2 z}{2k}\right) dz \tag{25}$$

for vertical propagation, subject to the condition that

$$\ell_0 \ll \sqrt{\lambda z} \ll L_0 .$$

$F_A(\kappa)$ has its maximum near $\kappa = 1/\sqrt{\lambda z}$. The two-dimensional Fourier Bessel transform of $F_A(\kappa)$ is log-amplitude covariance, $\sigma_\ell^2(\rho)$, in the telescope aperture plane. Thus,

$$\sigma_\ell^2(\rho) = 2\pi \int_0^\infty J_0(\kappa\rho)\, F_A(\kappa)\, k\, dk \tag{26}$$

$$= 4\pi^2 k^2 \int_0^\infty C_N^2(z) \int_0^\infty \Phi_N(\kappa)\, J_0(\kappa\rho) \times \sin^2\left(\frac{\kappa^2 z}{2k}\right) \kappa\, d\kappa\, dz ,$$

where

$$\Phi_N(\kappa) = 0.033\kappa^{-11/3}.$$

A peak near $\kappa = 1/\sqrt{\lambda z}$ in the spatial frequency domain means $\sigma_{\ell}^{2}(\rho)$ will have a correlation distance on the order $\sqrt{\lambda z}$. From Fresnel diffraction theory $\sqrt{\lambda z}$ will be recognized as the radius of first zone. Thus the general statement can be made that turbulence of dimensions $\sqrt{\lambda z}$ located a distance z from the receiving plane will have the largest effect on $\sigma_{\ell}^{2}(\rho)$.

The quantity $\sqrt{\lambda z}$ can be inferred from a direct measurement of $\sigma_{\ell}^{2}(\rho)$, although such data is difficult to obtain. A second method based on aperture dependence of CIV^2 will be used instead. Data of this form is available as reported in Chapter IV. Use is made of equation (24) for CIV^2 at aperture diameter D to obtain

$$[CIV^2]_D = A_I \left[\frac{D}{\sqrt{\lambda z}} ;\ CIV^2\right] CIV^2 . \tag{27}$$

The aperture averaging factor A_I is roughly determined by Tatarski's equation (13.28) for a quantity he labels G. Numerical integration of G as CIV^2 approaches zero is presented in his Figure 36. For values of $D/\sqrt{\lambda z}$ between 0.2 and 3.0, G can accurately be modeled by an exponential. Thus,

$$G = 1.20\ e^{-1.34\ D/\sqrt{\lambda z}}$$

and

$$[CIV^2]_D = 1.20\ e^{-1.34 D/\sqrt{\lambda z}}\ CIV^2 . \tag{28}$$

Experimental data for CIV^2 as a function of aperture, D, is then also fit with an exponential by the expression

$$[CIV^2]_D = A\ e^{-BD} . \tag{29}$$

Equating these two expressions for $[CIV^2]_D$ yields a solution for $\sqrt{\lambda z}$ in terms of the data-fit parameter, B. B has dimensions of length^{-1}, such that

$$\sqrt{\lambda z} = -\ 1.33/B .$$

This becomes

$$\sqrt{\lambda H_0} = \frac{-1.33}{B\sqrt{\sec\theta}} \tag{30}$$

when allowance for stellar zenith angle, θ, is made.

Since A_I also depends on θ as well as D through the term $\sqrt{\lambda H_0 \sec\theta}$, the zenith angle dependence of $[CIV^2]_D$ will change for various ranges of the ratio $D/\sqrt{\lambda H_0 \sec\theta}$. Tatarski points out that for small values of θ, $[CIV^2]_D$ can be approximated by $\alpha \sec^{\beta}\theta$, where β is a power dependent on aperture size. As D increases so should β from the point detector value of 11/6 to a value of 3.0 when $D \gg \sqrt{\lambda H_0 \sec\theta}$.

The effect of exceeding the correlation distance has been measured by Protheroe[30]. He obtained a 2.5 times reduction in CIV in going from a 2.54-cm diameter aperture to a 15.2-cm diameter. This corresponds to a reduction in $\sigma_{\ell}^2(\rho)$ of 6.25. For the 15.2-cm-diameter aperture he observed the following dependence on zenith angle:

$$CIV \propto \sec^{1.2}\theta$$

and

$$\sigma_{\ell}^2 \propto \sec^{2.4}\theta . \tag{31}$$

The calculated correlation distance was about 8 to 10 centimeters. Protheroe's actual CIV values must be corrected for this experimental technique in order to arrive at CIV for zenith viewing. When this is done the following average values can be presented; these in turn predict average σ_{ℓ}^2 values. All measurements were taken with a 15.2-cm aperture.

	CIV	σ_{ℓ}^2
Summer	0.14	0.0049
Winter	0.16	0.0064

The frequency spectrum of irradiance is determined by the same factors of correlation distance, wavelength, zenith angle, and aperture size. In addition, the velocity spectrum of upper altitude winds becomes very important. Increases in zenith angle or aperture size are reflected in a decrease in magnitude of high frequency components. These effects are observed in spectral densities of stellar image intensity and log-amplitude.

The physical basis of spectral-density aperture dependence can be understood by considering the structure of irradiance in the telescope aperture plane. The structure consists of a continuous size spectrum of bright and dark patches changing with respect to time and sweeping across the aperture. As the aperture becomes much larger than the correlation distance the small patches, which have dimensions of the order of the correlation distance and are responsible for the high frequency components, produce less of an effect due to aperture averaging. Larger particles and, therefore, lower frequency components do not suffer as much averaging. The rate at which the pattern or parts of the pattern are swept across the aperture is determined by upper altitude wind profile. In the middle latitudes wind velocity is strongly peaked in the 8- to 14- kilometer region of the tropopause. This is not surprising since turbulence generation is readily associated with high flow velocities. Typical velocities at the tropopause are from 20 to 100 meters per second and the flow is often referred to as a jet stream. On the basis of the above physical considerations, a proportionality to irradiance frequency can be asserted as follows:

$$f \propto \frac{V_N}{\sqrt{\lambda H_0 \sec \theta}} , \tag{32}$$

where

V_N = component of wind velocity normal to the propagation path.

Theoretical analysis of irradiance frequency behavior best proceeds in the manner revealed by Tatarski. His equation (13.38) expresses spectral density of image intensity in terms of an integral over the two-dimensional spatial spectrum of irradiance and a filter function for a circular unobstructed aperture

$$W_I(f) = \frac{8\pi}{I_0^2} \int_0^\infty \frac{1}{V_N} F_I\left(\sqrt{\kappa^2 + \frac{4\pi^2 f^2}{V_N^2}}\right) \left[\frac{2J_1\left(D/2\sqrt{\kappa^2 + 4\pi^2 f^2/V_N^2}\right)}{\left(D/2\sqrt{K^2 + 4\pi^2 f^2/V_N^2}\right)}\right]^2 d\kappa, \qquad (33)$$

where

V_N = component of wind velocity normal to the propagation path,

κ = spatial frequency in aperture plane ,

f = temporal frequency,

D = aperture diameter,

I_0 = average irradiance,

and

$F_I(\kappa)$ = two-dimensional spatial spectrum of irradiance.

To arrive at this point Tatarski has employed the "frozen in" theory of turbulence structure. The physical basis of the theory is the assumption that wind transports turbulent structure across the propagation path before the structure can itself change. In meteorology this would be equivalent to the assumption of Taylor's hypothesis.[9] The result is that irradiance, $I(\vec{x}, t + \tau)$, at point, $\vec{x}$, and time, t , plus a delay, τ, can be simply connected with $I(\vec{x}, t)$ displaced by a distance $\vec{V}_N\tau$ by the expression

$$I(\vec{x}, t + \tau) = I(\vec{x} - \vec{V}_N \tau, t). \qquad (34)$$

Autocorrelation of irradiance, $R_I(\tau)$, can then be expressed with this result as follows:

$$R_I(\tau) = \frac{\langle [I(\vec{x}, t + \tau) - I_0]\,[I(\vec{x}, t) - I_0] \rangle}{\langle I(\vec{x}, t)^2 \rangle} . \qquad (35)$$

Equation (13.38) then results when correction for circular aperture is made and κ is shifted by an amount $2\pi f/\vec{V}_N$.

Taylor's hypothesis has been verified experimentally by several researchers. For the particular case of vertical path the reader is referred to the work of Gossard[31]. A natural question at this point would concern the range of validity of Taylor's hypothesis. Tatarski[19] has shown that the condition for validity can be expressed as

$$\sqrt{\lambda z} \ll L_0 , \tag{36}$$

where

L_0 = outer scale of turbulence,

and

z = distance from detector to the turbulence generating region.

That is, the dimensions of turbulence structure that effect light propagation should be much less than the dimension of the flow as a whole. This is simply one side of the condition for operating within the inertial subrange.

Tararski development of $W_I(f)$ beyond equation (13.38) assumes a constant value for strength of turbulence and wind velocity, as might reasonably be expected for a horizontal path. Observations of starlight require a knowledge of the interaction of all regions in the vertical path. These regions contain different values of C_N^2 and V_N and must be weighted according to their distance from the receiver. This can be accomplished mathematically by obtaining the vertical propagation relation for $F_I(\kappa)$, inserting the expression into equation (33), and interchanging the order of integration so that the κ integration can be performed first. $F_I(\kappa)$ is obtained from $F_A(\kappa)$, the two-dimensional spectral density of amplitude in equation (25), by noting the relation

$$F_I(\kappa) \approx 4\, I_0^2\, F_A(\kappa) .$$

Thus,

$$F_I(\kappa) \approx 8\pi I_0^2 k^2 \int_0^\infty C_N^2(z)\, \Phi_n(\kappa) \sin^2\left(\frac{\kappa^2 z}{2k}\right) dz$$

$$= .264\, \pi\, I_0^2 k^2 \int_0^\infty C_N^2(z)\, \kappa^{-11/3} \sin^2\left(\frac{\kappa^2 z}{2k}\right) dz. \tag{37}$$

This is the vertical propagation relation for $F_I(k)$.

Inserting this approximation into equation (33) yields

$$W_I(f) \approx 2.11\, \pi^2 k^2 \int_0^\infty \frac{1}{V_N(z)} \int_0^\infty C_N^2(z) \left[\kappa^2 + \frac{4\pi^2 f^2}{V_N^2(z)}\right]^{-11/6} \times$$

$$\sin^2\left[\frac{(\kappa^2 + 4\pi^2 f^2/V_N^2(z))\, z}{2k}\right] dz \left[\frac{2J_1 (D/2 \sqrt{\kappa^2 + 4\pi^2 f^2/V_N^2(z)}}{D/2 \sqrt{\kappa^2 + 4\pi^2 f^2/V_N^2(z)}}\right]^2 d\kappa$$

$$= 2.11\, \pi^2 k^2 \int_0^\infty \frac{C_N^2(z)}{V_N(z)} \int_0^\infty [\kappa^2 + 4\pi^2 f^2/V_N^2(z)]^{-11/6} \times$$

$$\sin^2\left[\frac{(\kappa^2 + 4\pi^2 f^2/V_N^2(z))\, z}{2k}\right] \left[\frac{2J_1 (D/2 \sqrt{\kappa^2 + 4\pi^2 f^2/V_N^2(z)})}{D/2 \sqrt{\kappa^2 + 4\pi^2 f^2/V_N^2(z)}}\right]^2 d\kappa\, dz$$

$$= 2.11\, \pi^2 k^2 \int_0^\infty \frac{C_N^2(z)}{V_N(z)} F\{f,\ V_N(z),\ D,\ k\}\, dz. \tag{38}$$

This result shows that irradiance frequency spectrum is expressable in terms of an integral over the turbulence and velocity profiles and a non-linear function F $\{f\ , V_N(z), D, k\}$. The specific form of F depends on the interaction of wind velocity with aperture shape and the spatial spectrum of turbulence fluctuations. In Chapter V this result is used to construct a model for $C_N^2(h)$.

Image Motion

Fluctuations in the position of image center of gravity result from atmospherically induced changes in the phase or shape of the incoming wavefront. Most changes can be attributed to random linear phase shifts or tilts in the wavefront.[20] The other principal wavefront degradation is quadratic in form and leads to focusing errors, thus contributing to blurring of the image. For a point detector, wavefront tilt will result in displacement of the entire image. Tatarski[19] has related wavefront tilts to phase structure function by examining a two-point correlation (interferometer) experiment, Figure 2.

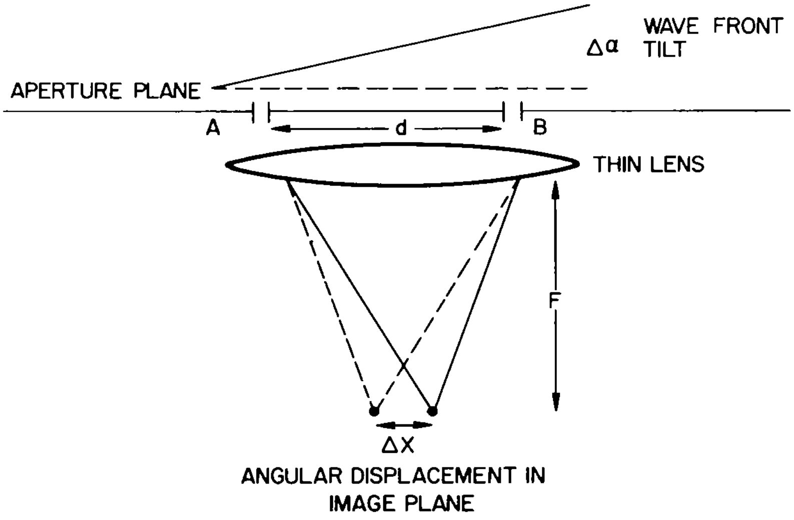

Figure 2. Interferometer case

Consider two point apertures, A and B, separated by a distance, d. Incoming starlight represented by a wavefront tilted with respect to d is brought to a focus after passing through the point apertures. Angle of tilt, $\Delta\alpha$ radians, is equal to the angular displacement of the diffraction pattern in the image plane. Optical phase shift, $\Delta\phi$, between A and B, can be expressed in terms of this tilt angle by

$$\Delta\phi = \phi_B - \phi_A = k\,d\,\Delta\alpha\,, \tag{39}$$

where

$$k = \frac{2\pi}{\lambda}\,.$$

Since the phase structure function, $D_\phi\,(d)$, is defined as the mean square difference of phase between two points,

$$\left\langle(\phi_B - \phi_A)^2\right\rangle = \left\langle(\Delta\phi)^2\right\rangle = D_\phi\,(d)\,. \tag{40}$$

Then, the above relation for tilt angle yields the expression

$$\left\langle(\Delta\alpha)^2\right\rangle = \frac{\left\langle(\Delta\phi)^2\right\rangle}{k^2\,d^2} = \frac{D_\phi\,(d)}{k^2\,d^2}\,. \tag{41}$$

The angular brackets once again denote an ensemble average. Tatarski[19] employs his expression for phase structure function based on the Rytov approximation and the (OK) turbulence spectrum as follows:

$$D_\phi\,(d) = K\,k^2\,d^{5/3}\int_0^\infty C_N^2\,(z)\,dz\,. \tag{42}$$

The value of K depends on the relationship of d to the correlation of irradiance fluctuations, so that

$$K = \begin{cases} 2.91 & d > \sqrt{\lambda z} \\ 1.46 & d < \sqrt{\lambda z} \end{cases}\,.$$

For stellar observations distance, z, along the propagation path becomes

$$z = h\sec\theta\,,$$

where

θ = zenith angle

and

h = altitude.

Then,

$$D_\phi\,(d) = K\,k^2\,d^{5/3}\sec\theta\int_0^\infty C_N^2\,(h)\,dh\,. \tag{43}$$

Substitution in equation (41) leads to the following expression for mean square angular fluctuations:

$$(\Delta\alpha)^2 = K d^{-1/3} \sec\theta \int_0^\infty C_N^2(h)\, dh \,. \tag{44}$$

This is just the variance of the center of gravity of the diffraction pattern about the optic axis. If the stellar observation is made with a telescope instead of an interferometer, wavefront tilt from all points in the unobstructed aperture will contribute to image motion. For large apertures, wavefront tilt in different regions of the aperture will be uncorrelated and lead to a reduction in image motion. In addition, a non-uniform irradiance distribution will give unequal weights to tilts in the different regions of the aperture. As the aperture dimensions exceed the irradiance correlation distance this effect will diminish in importance since the average irradiance pattern predominates over the fluctuating part. The resultant image for a reasonably large aperture telescope (diameter greater than a few centimeters) will be blurred and exhibit a center of gravity displacement.

In generalizing to such a case from the interferometer result above, Tatarski asserts that the maximum aperture dimension plays the role of the point aperture separation, d, with the only other change being in the value of proportionality constant, K. His intuitive feeling is apparently correct, as will be shown in the following analysis due to Hufnagel[32]. The analysis will be extended here to include a numerical prediction of image motion variance.

The instantaneous position of image center of gravity, $\vec{r}(t)$, is just the first moment of the image intensity pattern

$$\vec{r}\,(t) = \frac{\int_{-\infty}^{\infty} \vec{x}\, I\,(\vec{x},\ t)\, d\vec{x}}{\int_{-\infty}^{\infty} I\,(\vec{x},\ t)\, d\vec{x}}\ , \qquad (45)$$

where $\vec{x}$ is a two-dimensional vector in the image plane centered on the telescope optical axis. Starlight incident on the telescope is represented by the complex field distribution, $u\,(\vec{v}, t)$, in terms of $\vec{v}$, a two-dimensional vector in the aperture plane. Neglected here is the optical frequency time behavior of the incoming wavefront. The imaging process from aperture to image plane as performed by the telescope optics is described adequately by the Fraunhofer diffraction formula

$$U(\vec{x},\ t) = C \int_{-\infty}^{\infty} u\,(\vec{v},\ t)\, \exp\left(-\frac{2\pi i}{\lambda F}\, \vec{v} \cdot \vec{x}\right) d\vec{v}\,, \qquad (46)$$

where

$$I(\vec{x},\ t) = U^{*}(\vec{x},\ t)\, U(\vec{x},\ t)\,.$$

The normalization constant, C, is determined by the telescope geometry and incident light energy. For a lens of clear circular aperture and normalization to unit energy,

$$\int_{-\infty}^{\infty} I(\vec{x},\ t) = 1$$

and

$$C = \frac{2}{\lambda DF \sqrt{\pi}}\ ,$$

where

D = aperture diameter,

F = lens focal length,

and

λ = wavelength of light.

As demonstrated in Appendix A and discussed in the next section on image size, the optical transfer function in terms of image plane coordinates can be written

$$T(\vec{f},\ t) = \int_{-\infty}^{\infty} I(\vec{x},\ t) \exp(-2\pi i \vec{f} \cdot \vec{x})\, d\vec{x}, \tag{47}$$

where

$\vec{f}$ = two-dimensional spatial frequency vector.

Image center-of-gravity can be expressed in terms of $T(\vec{f}, t)$ by taking the first partial with respect to $\vec{f}$ and evaluation at $\vec{f} = 0$, as follows:

$$\frac{\partial T(\vec{f},\ t)}{\partial \vec{f}} = -2\pi i \int_{-\infty}^{\infty} \vec{x}\, I(\vec{x},\ t) \exp(-2\pi i \vec{f} \cdot \vec{x})\, d\vec{x}.$$

Since

$$\vec{r}(t) = \int_{-\infty}^{\infty} \vec{x}\, I(\vec{x},\ t)\, d\vec{x},$$

then

$$\vec{r}(t) = \frac{i}{2\pi} \left. \frac{\partial T(\vec{f},\ t)}{\partial \vec{f}} \right|_{\vec{f}=0} . \tag{48}$$

In order to express $\vec{r}(t)$ in terms of irradiance and phase in the aperture plane, it is first necessary to express $T(\vec{f}, t)$ in these quantities. The Fraunhofer formula, equation (46), can be inserted in equation (47) and the mathematics performed to achieve the desired result, as follows:

$$I(\vec{x},\ t) = U^*(\vec{x},\ t)\, U(\vec{x},\ t)$$

$$= C^2 \int_{-\infty}^{\infty}\int_{-\infty}^{\infty} u^*(\vec{w},\ t)\, u(\vec{v},\ t) \exp\left[\frac{2\pi i}{\lambda F} (\vec{w} - \vec{v}) \cdot \vec{x}\right] d\vec{w}\, d\vec{v}.$$

Hence,

$$T\,(\vec{f},\ t) = C^2 \iiint_{-\infty}^{\infty} u(\vec{w},\ t)\ u(\vec{v},\ t) \exp\left[\frac{2\pi i}{\lambda F}\,(\vec{w} - \vec{v} - \lambda F\,\vec{f}) \cdot \vec{x}\right] d\vec{w}\, d\vec{v}\, d\vec{x}$$

$$= C^2 \iint_{-\infty}^{\infty} u^*\,(\vec{w},\ t)\ u\,(\vec{v},\ t) \int_{-\infty}^{\infty} \exp\,[\ \cdot\ ]\ d\vec{x}\, d\vec{w}\, d\vec{v}$$

$$= C^2 \int_{-\infty}^{\infty} \int_{-\infty}^{\infty} u\,(\vec{w},\ t)\ u\,(\vec{v},\ t)\ \delta\left[\frac{\vec{w} - (\vec{v} + \lambda F\,\vec{f})}{\lambda F}\right] d\vec{w}\, d\vec{v},$$

or

$$T\,(\vec{f},\ t) = \frac{4}{\pi D^2} \int_{-\infty}^{\infty} u\,(\vec{v} + \lambda F\,\vec{f})\ u\,(\vec{v})\ d\vec{v}\,. \tag{49}$$

The complex disturbance in the aperture plane $u\,(\vec{v})$ is now expressed in terms of amplitude and phase by

$$u\,(\vec{v},\ t) = \sqrt{I\,(\vec{v},\ t)}\ \exp\,[i\,\phi\,(\vec{v},\ t)],$$

where

$\phi\,(\vec{v},\ t)$ = optical phase in radians

and

$$u^*\,(\vec{v} + \lambda F\,\vec{f},\ t) = \sqrt{I\,(\vec{v} + \lambda F\,\vec{f},\ t)}\ \exp\,[-\,i\,\phi\,(\vec{v} + \lambda F\,\vec{f},\ t)]\,.$$

The partial of $T(\vec{f}\,,\ t)$ with respect to $\vec{f}$ can be performed as follows:

$$\frac{\partial T\,(\vec{f},\ t)}{\partial \vec{f}} = \frac{4}{\pi D^2} \int_{-\infty}^{\infty} u\,(\vec{v},\ t)\ \frac{\partial}{\partial \vec{f}}\ u^*\,(\vec{v} + \lambda F\,\vec{f},\ t)\ d\vec{v}$$

$$= \frac{4}{\pi D^2} \iint_{-\infty}^{\infty} u\,(\vec{v},\ t) \left\{ -\,i\,\lambda F \sqrt{I\,(\vec{v} + \lambda F \vec{f},\ t)}\, \exp\,[-\,i\,\phi\,(\vec{v} + \lambda F \vec{f},\ t)]\, \frac{\partial \phi\,(\vec{v} + \lambda F \vec{f},\ t)}{\partial\,(\vec{v} + \lambda F \vec{f})} \right.$$

$$\left. +\, \exp\,[-\,i\,\phi\,(\vec{v} + \lambda F \vec{f},\ t)]\, \frac{\partial}{\partial \vec{f}} \sqrt{I\,(\vec{v} + \lambda F \vec{f},\ t)} \right\} d\vec{v},$$

$$\left| \frac{\partial T\,(\vec{f},\ t)}{\partial \vec{f}} \right|_{\vec{f}=0} = \frac{4}{\pi D^2} \int_{-\infty}^{\infty} \left\{ -\,i\,\lambda F\, I\,(\vec{v},\ t)\, \frac{\partial \phi\,(\vec{v})}{\partial \vec{v}} \right. \tag{50}$$

$$\left. +\, \frac{\partial}{\partial \vec{f}} \sqrt{I\,(\vec{v},\ t)\; I\,(\vec{v} + \lambda F \vec{f},\ t)} \right\} d\vec{v}\,.$$

The final form relating image center of gravity to irradiance and phase is obtained by noting that the integral over all $\vec{v}$ of the second term vanishes since $I(\vec{v},\, t)$ has a zero value outside the aperture and by substituting the remaining term in equation (48)

$$\vec{r}\,(t) = \frac{4\,k\,F}{\pi D^2} \int_{-\infty}^{\infty} I\,(\vec{v},\ t)\, \frac{\partial}{\partial \vec{v}}\, \phi\,(\vec{v},\ t)\, d\vec{v}\,. \tag{51}$$

Image position thus depends on the derivative of optical phase, which is the meaning of wavefront tilt, weighted by the irradiance pattern. At this point the variable, t, will be suppressed for ease of notation and the variance of $\vec{r}$ calculated.

The distribution of tilts is symmetrical about zero tilt, thus the average value of image motion, $\vec{r}$, will be zero. The variance of image motion expressed in radians squared, through division by F^2, is

$$\langle \vec{r}\cdot\vec{r}\rangle = \left\langle \frac{16\,k^2}{\pi^2 D^4} \int_{=\infty}^{\infty} \int_{-\infty}^{\infty} I(\vec{v})\, I(\vec{w})\, \frac{\partial\phi(\vec{v})}{\partial\vec{v}}\, \frac{\partial\phi(\vec{w})}{\partial\vec{w}}\, d\vec{v}\, d\vec{w} \right\rangle , \tag{52}$$

where

$\vec{r}$ is now measured in radians.

The angular brackets once again denote an ensemble average. In practice the ensemble is formed by the time behavior of $\vec{r}$ (t). Convincing evidence exists, both in the literature[33] and in the author's experimental work, that irradiance and image motion are sample functions of independent stochastic processes. In that event

$$\langle \vec{r}\cdot\vec{r}\rangle = \frac{16\,k^2}{\pi^2 D^4} \int_{-\infty}^{\infty} \int_{-\infty}^{\infty} I(\vec{v})\, I(\vec{w}) \left\langle \frac{\partial\phi(\vec{v})}{\partial\vec{v}}\, \frac{\partial\phi(\vec{w})}{\partial\vec{w}} \right\rangle \partial\vec{v}\, \partial\vec{w}.$$

If in addition, the processes are considered stationary, $\vec{w} = \vec{v} + \vec{y}$ and $d\vec{w} = d\vec{y}$. Thus,

$$\langle \vec{r}\cdot\vec{r}\rangle = \frac{16\,k^2}{\pi^2 D^4} \int_{-\infty}^{\infty} \int_{-\infty}^{\infty} I(\vec{v})\, I(\vec{v}+\vec{y}) \left\langle \frac{\partial\phi(\vec{v})}{\partial\vec{v}}\, \frac{\partial\phi(\vec{v}+\vec{y})}{\partial\vec{y}} \right\rangle d\vec{v}\, d\vec{y}.$$

Because of stationarity, the expression

$$\left\langle \frac{\partial\phi(\vec{v})}{\partial\vec{v}}\, \frac{\partial\phi(\vec{v}+\vec{y})}{\partial\vec{y}} \right\rangle$$

is invariant under translation to

$$\left\langle \frac{\partial\phi(0)}{\partial\vec{v}}\, \frac{\partial\phi(\vec{y})}{\partial\vec{y}} \right\rangle .$$

The expression for $\langle \vec{r} \cdot \vec{r} \rangle$ is of the form

$$\langle \vec{r} \cdot \vec{r} \rangle = \frac{16k^2}{\pi^2 D^4} \int_{-\infty}^{\infty} T_0(\vec{y})\, R_{\nabla\phi}(\vec{y})\, d\vec{y}\,, \tag{53}$$

where

$R_{\nabla\phi}(\vec{y})$ = autocorrelation of tilt, $\nabla\phi$
and
$T_0(\vec{y})$ = autocorrelation of irradiance.

The additional assumption of isotropy allows the autocorrelations to be expressed in terms of $|\vec{y}|$. Tilt autocorrelation is simply related to phase autocorrelation through the vector identity

$$R_{\nabla\phi}(|\vec{y}|) = -\nabla^2 R_\phi(|\vec{y}|). \tag{54}$$

$T_0(|\vec{y}|)$ can be modeled fairly accurately by the assumption of constant irradiance over the aperture. The integral

$$T_0(|\vec{y}|) = \int_{-\infty}^{\infty} I(\vec{v})\, I(\vec{v} + \vec{y}) \quad d\vec{v}$$

reduces to a result for the overlap of two circles of diameter, D. This is equivalent to the diffraction-limited modulation transfer function for the optical system,

$$T_0(|\vec{y}|) = \frac{D^2}{2} \left\{ \cos^{-1} \left(\frac{|\vec{y}|}{D}\right) - \left(\frac{|\vec{y}|}{D}\right) \left[1 - \left(\frac{|\vec{y}|}{D}\right)^2\right]^{1/2} \right\}. \tag{55}$$

Phase autocorrelation is obtained from

$$D_\phi(|\vec{y}|) = 2\,[R_\phi(0) - R_\phi(|\vec{y}|)]$$

and the Tatarski expression for the phase structure function,

$$D_\phi(|\vec{y}|) = 2.91\ k^2\ |\vec{y}|^{5/3} \sec\theta \int_0^\infty C_N^2(h)\, dh,$$

so that

$$\nabla^2 R_\phi(|\vec{y}|) = -\ \frac{10}{18}\ 2.91\ k^2\ |\vec{y}|^{-1/3} \sec\theta \int_0^\infty C_N^2(h)\, dh. \tag{56}$$

Insertion of equations (55) and (56) into equation (53), conversion to polar coordinates, and simplification leads to the following expression:

$$\left\langle r^2 \right\rangle = \frac{4.11}{D^2} \int_0^D \left[\cos^{-1}\left(\frac{y}{D}\right) - y/D\ (1 - (y/D)^2)^{1/2}\right]^{2/3} y\, dy \times \tag{57}$$

$$\sec\theta \int_0^\infty C_N^2(h)\, dh.$$

The first integral can be transformed into

$$D^{5/3} \int_0^1 [\cos^{-1}\rho - \rho(1-\rho^2)^{1/2}]\ \rho^{2/3}\, d\rho.$$

This has been evaluated numerically on a digital computer and found very nearly equal to

$$\frac{3}{8} D^{5/3}.$$

Up to this point, the analysis has been in terms of two-dimensional angular distance $\vec{r}$ in the image plane. For comparison with experimental work reported in Chapter IV the desired quantity is one-dimensional variance, given by

$$\langle x^2 \rangle = \langle r^2 \cos^2 \alpha \rangle ,$$

where

$\vec{r} = \vec{i}\, x + \vec{j}\, y$

$= \vec{i}\, r \cos\alpha + \vec{j}\, r \sin\alpha$

and

α = reference angle.

Isotropic behavior for optical phase tilts in the aperture plane guarantees isotropic image motion, r is independent of α, and

$$\begin{aligned}\langle r^2 \cos^2 \alpha \rangle &= \langle r^2 \rangle \langle \cos^2 \alpha \rangle \\ &= \langle r^2 \rangle \; 1/2 .\end{aligned}$$

The end result for $\langle x^2 \rangle$ is

$$\langle x^2 \rangle = 0.56\, D^{-1/3} \sec\theta \int_0^\infty C_N^2(h)\, dh, \tag{58}$$

where

$D \gtrsim \sqrt{\lambda Z}$

and x is expressed in radians.

Parameter dependence is the same as for the interferometer case but the constant multiplier is reduced. The important results are that $\langle x^2 \rangle$ is independent of optical wavelength and only weakly dependent on telescope aperture diameter. Irradiance fluctuations discussed previously exhibit a rather strong wavelength and aperture dependence. Zenith angle and turbulence dependence expressed by

$$\sec\theta \int_0^\infty C_N^2(h)\, dh,$$

where

θ = stellar zenith angle,

predict that $\langle x^2 \rangle$ is proportional to air mass ($\sec\theta$) between source and observer with the strength of turbulence at each altitude weighted equally. This one-dimensional result will be denoted σ_M^2, variance of image motion, so that

$$\langle x^2 \rangle = \sigma_m^2 .$$

For aperture diameter less than $\sqrt{\lambda z}$ the phase structure function (Tatarski) retains the same form but is reduced by a factor of about two. For this case, however, the assumption of a constant irradiance across the aperture could not be used. It is likely that the resultant aperture dependence would differ from $D^{-1/3}$. For $D < \ell_0$, the inner scale of turbulence, even the phase structure function departs from $D^{-1/3}$ dependence. In the other limit as D grows very large, the upper bound on the phase structure function and thus $<x^2>$ is determined by the outer scale of turbulence. This limit is ill-defined and may be encountered as close as a meter or as distant as a kilometer.

Time behavior of image motion is described statistically by autocorrelation analysis of a certain length sample record of data. As a first approximation consider the interferometer case discussed previously in the determination of image motion variance. Normalized phase difference autocorrelation, $R_{\phi_d}(\tau)$, for the spatial separation, d, and variable time lag, τ, is

$$R_{\phi_d}(\tau) = \frac{\langle (\phi_A - \phi_B)_t \, (\phi_A - \phi_B)_{t+\tau} \rangle}{\langle (\phi_A - \phi_B)_t^2 \rangle} . \tag{59}$$

The denominator is by definition phase structure function for separation, d. The numerator may, as outlined by Kolchinskii[34], be expanded into a sum of structure function terms.

Thus,

$$\left\langle (\phi_A - \phi_B)_t \, (\phi_A - \phi_B)_{t+\tau} \right\rangle =$$

$$\left\langle \phi_{A_t} \phi_{A_{t+\tau}} - \phi_{A_t} \phi_{B_{t+\tau}} + \phi_{B_t} \phi_{B_{t+\tau}} - \phi_{B_t} \phi_{A_{t+\tau}} \right\rangle \tag{60}$$

$$= \left\langle \frac{1}{2} \left(\phi_{B_t} - \phi_{A_{t+\tau}}\right)^2 + \frac{1}{2} \left(\phi_{A_t} - \phi_{B_{A+\tau}}\right)^2 \right\rangle \times$$

$$\left\langle -\frac{1}{2} \left(\phi_{A_t} - \phi_{A_{t+\tau}}\right)^2 - \frac{1}{2} \left(\phi_{B_t} - \phi_{B_{t+\tau}}\right)^2 \right\rangle .$$

In order to evaluate the structure functions, certain assumptions must be made.

(1) As in the analysis of irradiance time-dependence, consider "frozen-in" turbulence. The turbulence inhomogeneties are transferred by a wind of speed V_N parallel to the line connecting point apertures A and B.

(2) Assume a single-layer model. The turbulence is located at a distance z with strength C_N^2 and results in a phase structure function

$$D_\phi (d) = 2.91 \; k^2 \, d^{5/3} \, z \, C_N^2 .$$

(3) The turbulence process is assumed to be homogeneous and isotropic as before.

The value of phase at point A and the time $A + \tau$, $\phi_A (t + \tau)$, is the same as that at the point $A - V_N \tau$ and the time $t, \phi_{A - V_N \tau} (t)$. Likewise,

$$\phi_A (t) = \phi_{A + V_N \tau} (t + \tau),$$

$$\phi_B (t + \tau) = \phi_{B - V_N \tau} (t),$$

and

$$\phi_B (t) = \phi_{B + V_N \tau} (t + \tau) .$$

These relations allow the structure function terms in equation (60) to be expressed in terms of D_ϕ and an argument that includes $V_N \tau$ along with the point aperture separation, d, as follows:

$$\left\langle (\phi_{A_t} - \phi_{A_{t+\tau}})^2 \right\rangle = D_\phi (V_N \tau),$$

$$\left\langle (\phi_{B_t} - \phi_{B_{t+\tau}})^2 \right\rangle = D_\phi (V_N \tau),$$

$$\left\langle (\phi_{B_t} - \phi_{A_{t+\tau}})^2 \right\rangle = D_\phi (|d + V_N \tau|),$$

$$\left\langle (\phi_{A_t} - \phi_{B_{t+\tau}})^2 \right\rangle = D_\phi (|d - V_N \tau|),$$

and

$$R_{\phi_d}(\tau) = \frac{\frac{1}{2} D_\phi (|d + V_N \tau|) + \frac{1}{2} D_\phi (|d - V_N|) - D_\phi (V_N \tau)}{D_\phi (d)},$$

or

$$R_{\phi_d}(\tau) = \frac{\left(1 + \frac{V_N \tau}{d}\right)^{5/3} + \left(\left|1 - \frac{V_N \tau}{d}\right|\right)^{5/3}}{2} - {\frac{V_N \tau}{d}}^{5/3}.$$

The result is independent of strength of turbulence, distance to the turbulence, and optical wavelength and depends only on aperture separation, d, and the wind speed, V_N. The result, of course, holds only for τ values such that the phase structure function argument is within the inertial subrange.

The total effect of many such layers can be examined by adding the autocorrelation for each layer weighted by the strength of turbulence and wind velocity for that layer. Thus,

$$R_{\phi_d} = \sum_{i=1}^{\infty} \left\{ \left[\frac{1 + V_N(z_i)\tau}{2}\right]^{5/3} + \left[\frac{|1 - V_N(z_i)\tau|}{2}\right]^{5/3} - [V_N(z_i)\tau]^{5/3} \right\} C_N^2(z_i)\,\Delta z \Bigg/ \sum_{i=1}^{\infty} d^{5/3} C_N^2(z_i)\,\Delta z .$$

As with the single-layer result the phase difference autocorrelation is identical to image motion autocorrelation. This is evident since

$$\phi_B - \phi_A = k\ d\ \Delta\ \alpha$$

and

$$R_{\phi_d}\ (\tau) \equiv R_\alpha\ (\tau) = R_x\ (\tau),$$

where

α = wavefront tilt angle

and

x = diffraction pattern angular shift in one-dimension.

The Fourier transform of $R_x(\tau)$, the angular shift autocorrelation, may be expressed in a form similar to equation (38) for irradiance spectral density. The first step is to express $R_x(\tau)$ in terms of image motion variance, σ_m^2. From equation (58)

$$\sigma_m^2 = .560\ D^{-1/3} \int_0^\infty C_N^2\ (z)\ d\ z,$$

where

D = aperture diameter $\gtrsim \sqrt{\lambda\ Z}$.

Noting that

$$\sigma_m^2 = \frac{.56\ D_\phi\ (D)}{k^2\ D^2}$$

yields the new form for $R_x(\tau)$, as follows:

$$R_x(\tau) = R_{\phi_d} = \int_0^\infty \frac{\left[\frac{1}{2} D_\phi(|d + V_N\tau|) + \frac{1}{2} D_\phi(|d - V_N\tau|) - D_\phi(V_N\tau)\right]}{D_\phi(d)}\ dz,$$

or

$$R_x\ (\tau) = \frac{.57}{D^2\ \sigma_m^2} \int_0^\infty C_N^2\ (z) \left[\frac{1}{2}\ |\ D + V_N\ \tau\ |^{5/3} + \frac{1}{2}\ |\ D - V_N\ \tau\ |^{5/3} - |\ V_N\ \tau\ |^{5/3}\right] d\ z. \tag{61}$$

Here the wind velocity which depends on optical path distance, z, has been brought inside the integration. Once again the passage from summation to an integral over z has been made. The Fourier transform of $R_x(\tau)$,

$$w_x(f) = 4 \int_0^{\infty} \cos(2\pi f \tau) R_x(\tau)\, d\tau ,$$

can now be expressed as follows:

$$w_x(f) = \frac{2.28}{D^2 \sigma_m^2} \int_0^{\infty} C_N^2(z)\, F\{f, v_N(z), D\}\, dz , \tag{62}$$

where the τ and f integrations have been interchanged. This is the result used in Chapter V to construct turbulence profiles.

Image Size

Specification of image size or profile is the final step in a description of the atmospherically distorted stellar image. Size determination and the whole investigation of image quality are handled best through the use of optical transfer function techniques. The transfer function of an optical system, OTF, is defined as the two-dimensional spatial Fourier transform of the image spread function. In the situation examined here, optical system is composed of telescope optics and atmosphere. Magnitude of OTF is a measure of reduction in contrast suffered by each Fourier component of the object after transmission through the entire imaging system. It is a function of the transform variable, image plane spatial frequency, f. The variable, f, has dimensions of cycles per unit length. Multiplication by system focal length, D, allows spatial frequency to be expressed in cycles per radian field of view. This will be denoted, ω. This, of course, is easily related to cycles per arc second. Relationship between OTF and image intensity distribution are derived in Appendix A for the particular case of starlight, i.e., point source at infinity and incoherent light. The result, if $T(\vec{f})$ is the optical transfer function, OTF, is

$$T(\vec{f}) = \int_{-\infty}^{\infty} I(\vec{x}) \exp(-2\pi i \vec{f}\cdot\vec{x})\, d\vec{x}, \tag{63}$$

where $\vec{f}$ = spatial frequency vector,

$\vec{x}$ = position vector,

and $I(\vec{x})$ = image intensity.

In general, $T(\vec{f})$ is complex and can be written in terms of a modulus and phase as

$$T(\vec{f}) = M(\vec{f}) \exp i\, \phi(\vec{f}). \tag{64}$$

For real, symmetric images $T(\vec{f})$ is real and positive, and

$$T(\vec{f}) = M(\vec{f}). \tag{65}$$

Analysis may proceed in terms of the modulation transfer function, $M(\vec{f})$ or MTF. Both phase and amplitude effects in the atmospherically distorted wavefront contribute to MTF. Phase effects can be thought of as wavefront tilts or bends. These lead to image tilt and blurring respectively, as previously noted. Amplitude effects create a random apodization of the aperture, i.e., they weigh the phase effects non-uniformly.

Just as phase and amplitude of the optical wavefront are functions of time so is MTF. Thus,

$$M(\vec{f}) = M(\vec{f}, t). \tag{66}$$

This will continue to be denoted $M(\vec{f})$ with the time dependence understood. Over a long period of time, as in long exposure photography, the resultant image can no longer be described by the telescope diffraction pattern but will be a relatively large blur circle. Under this condition the symmetry assumption is not too severe. Time-averaging and the random character of the distortions tend to average out any non-symmetries that appear. For very short-exposure times, all effects of image motion are frozen out, leaving a sharper well-defined image. While this image may approach the diffraction limit it will in general exhibit a residual blur. A recent analysis due to Fried[35] has shown that this blur is primarily a focusing error. Near the optical axis this is a symmetric aberration caused by a quadratic term in the description of wavefront shape. Unsymmetrical abberations, similar to coma, are numbered third in order of importance. This argues in favor of retaining the symmetry assumption above. A much more serious question concerns the existence of spatial invariance in the image plane for the short-exposure case. This is the concept of an isoplanatism patch as mentioned in Appendix A. If such an area, in which image spread function depends only on the separation of two measurement points, does not exist the mathematical formalism breaks down and a transfer function cannot be defined. It is not necessary that the isoplanatic region encompass the entire telescope field, just the general vicinity of the image. This may be quite a reasonable assumption although further verification is needed.

For a cascaded optical system such as the combination of atmosphere and telescope, the resultant MTF is just the product of individual MTF's. Thus,

$$\left\langle M(\vec{f})_0 \right\rangle_{\text{time}} = M(\vec{f})_T \left\langle M(\vec{f})_A \right\rangle_{\text{time}} , \tag{67}$$

where

$\left\langle M(\vec{f})_0 \right\rangle_{\text{time}}$ = observed MTF averaged over a certain time,

$M(\vec{f})_T$ = telescope optics MTF which is constant in time,

and

$\left\langle M(\vec{f})_A \right\rangle_{\text{time}}$ = atmospheric MTF averaged over the same time as above.

Telescope MTF based on the assumption of diffraction-limited optics, as set forth in Appendix A, is

$$M(\omega) = \frac{2}{\pi}\left[\cos^{-1}\frac{\lambda\,\omega}{D} - \frac{\lambda\,\omega}{D}\left(1 - \frac{\lambda\,\omega}{D}\right)^2\right]^{1/2}, \qquad \lambda\,\omega \le D, \tag{68}$$

and

$$= 0,\ \lambda\,\omega > D, \tag{69}$$

where

$\bar{\omega}$ = polar coordinate spatial frequency in cycles per radian field of view

$= F\,|\vec{f}|$.

Once again the ensemble of systems necessary for a correct averaging process is formed by a certain time sample of data.

Several different theoretical approaches[24,36] have resulted in the same expression for the atmospheric part of the long-term MTF, namely,

$$\left\langle M(\omega)_A\right\rangle_{LT} = \exp\left[-\frac{1}{2}\,D_w(\omega)\right], \tag{70}$$

where

LT = long-term time average.

The wave structure function, denoted $D_W(r)$, is the statistical description of atmospheric effects on the propagating wave. It is the sum of log-amplitude and phase structure functions mentioned previously, i.e.,

$$D_w(r) = D_\ell(r) + D_\phi(r). \tag{71}$$

Tatarski's expression for $D_w(r)$ is very similar to $D_\phi(r)$ of equation (56). In fact, beyond the log-amplitude correlation distance, $\sqrt{\lambda z}$, they are equal. Thus,

$$D_w(r) = 1.46\,k^2\,r^{5/3}\int_0^\infty C_N^2(z)\,dz, \qquad \ell_0 \ll r \ll \sqrt{\lambda z}, \tag{72}$$

and

$$D_w(r) = 2.91\,k^2\,r^{5/3}\int_0^\infty C_N^2(z)\,dz, \qquad r \gtrsim \sqrt{\lambda z}. \tag{73}$$

In both cases the assumption is made that

$$\sqrt{\lambda z} \gg \ell_0 .$$

As Fried[36] has pointed out, the conditions on r may be replaced by the same conditions on telescope aperture diameter, D. The last equation applies in general for telescopes of diameter

$$D \gtrsim 10 \text{ centimeters},$$

and in particular for the telescope used in the observations reported in Chapter IV. Spatial variable, r, in the aperture can be expressed in terms of image plane spatial frequency, ω, by

$$r = \lambda \, \omega .$$

The final desired form for $D_w(\omega)$ is

$$\begin{aligned} D_w(\omega) &= 2.91 \, (4\pi^2) \, \lambda^{-1/3} \, \omega^{5/3} \sec\theta \int_0^\infty C_N^2(h) \, dh \qquad (74) \\ &= C \, \omega^{5/3} , \end{aligned}$$

where C is a constant for a particular set of data and expresses the parameter dependence. The long-term atmospheric MTF becomes

$$\left\langle M(\omega)_A \right\rangle_{LT} = \exp\left(-\frac{C}{2}\,\omega^{5/3}\right) .$$

Spatial frequency dependence is contained in the $\omega^{5/3}$ factor. Image size dependence on C is revealed by applying the Fourier transform result of Appendix A, so that

$$\begin{aligned} I(s) &= 2\pi \int_0^\infty \omega \left\langle M(\omega)_A \right\rangle_{LT} J_0(2\pi s \omega) \, d\omega \\ &= 2\pi \int_0^\infty \omega \exp\left(-\frac{C}{2}\,\omega^{5/3}\right) J_0(2\pi s \omega) \, d\omega . \qquad (75) \end{aligned}$$

Here for convenience ω is expressed in cycles per arc second and distance, S, in the image plane is expressed in arc seconds. The 5/3 power law is close to a square power law and this approximation will be made.* When this is done the rather complicated integral above can be easily evaluated as follows:

$$I(s) \approx 2\pi \int_0^\infty \omega \exp\left(-\frac{C}{2}\omega^2\right) J_0(2\pi s \omega)\, d\omega$$

$$= \frac{2\pi}{C} \exp\left(-\frac{s^2}{c/2\pi^2}\right) . \qquad (76)$$

This is a Gaussian shape with variance, σ_s^2 , such that

$$\sigma_s^2 = C/4\pi^2$$

$$= 2.91\, \lambda^{-1/3} \sec\theta \int_0^\infty C_N^2(h)\, dh .$$

Here σ_s^2 is seen to be proportional to the negative one-third power of wavelength, secant of zenith angle, and the integrated strength of turbulence. This is essentially the same result obtained for variance of image motion, σ_m^2, with the weak dependence on aperture replaced here with a weak dependence on wavelength.

Short-term MTF has also been treated in the literature. An expression that is similar to that discussed by Fried[36] is

$$\left\langle M(\omega)_A \right\rangle_{ST} = \exp\left\{-\frac{1}{2} D_w(\omega)\left[1 - 1.026\left(\frac{\lambda\, \omega}{D}\right)^{1/3}\right]\right\} \qquad (77)$$

$$= \exp\left\{-\frac{C}{2}\omega^{5/3}\left[1 - 1.026\left(\frac{\lambda\, \omega}{D}\right)^{1/3}\right]\right\},$$

---

*See Appendix C.

where

$$D \gtrsim \sqrt{\lambda z}$$

and

$$C = 2.91 \, (4\pi^2) \, \lambda^{-1/3} \sec\theta \int_0^\infty C_N^2(h) \, dh \, .$$

The $\omega^{5/3}$ factor is the same as that found in long-term MTF and dominates the behavior of $\langle m(\omega)_A \rangle_{ST}$ for $\omega << (\lambda/D)$. Inclusion of the second term with its $\omega^{1/3}$ factor modifies the behavior for large spatial frequencies, $\omega \lesssim (\lambda/D)$. The factor λ/D is the resolution cutoff spatial frequency for a telescope of diameter D. This may be observed by substitution in equation (68). Since short-term MTF depends on the particular telescope diameter used, $\langle m(\omega)_A \rangle_{ST}$ is not a true atmospheric MTF. As Fried has pointed out, an MTF can be assigned to atmosphere only in the long-term case.

Long-term MTF can be measured experimentally. The length of time must be long enough to include all the effects of image motion, however. This implies an averaging time of tens of seconds, while the typical MTF measuring device completes a scan in a fraction of a second. The experimental device described in Chapter V employs instead an average measurement of many short-exposure images. This data can then be combined with a simultaneous measure of image motion, through the analysis presented below, to achieve an estimate of long-term MTF. This is the desired result since it is independent of all lens parameters and may truly be assigned to the atmosphere.

Long-term MTF can be defined in terms of short-term MTF and a transfer function assigned to image motion by

$$\langle M(\omega)_A \rangle_{LT} = \langle \langle M(\omega)_A \rangle_{ST} \, M(\omega)_m \rangle_{LT} \, . \qquad (78)$$

If image motion and short-term blur can be considered uncorrelated, it follows that

$$\left\langle M(\omega)_A \right\rangle_{LT} = \left\langle \left\langle M(\omega)_A \right\rangle_{ST} \right\rangle_{LT} \left\langle M(\omega)_m \right\rangle_{LT} .$$

Following the lead of Hufnagel[37] the image motion MTF can be expressed in terms of one-dimensional image motion variance, σ_m^2 , by

$$\left\langle M(\omega)_m \right\rangle_{LT} = \exp -\left\{4\,\pi^2 \frac{\sigma_m^2}{2}\,\omega^2\right\}, \tag{79}$$

where σ_m^2 is determined from a sample of data whose length roughly corresponds to long-term time average.

A rough check on this procedure can be made by assuming that $\langle\langle M(\omega)_A \rangle_{ST} \rangle_{LT}$ can be adequately represented by equation (77) for $\langle M(\omega)_A \rangle_{ST}$ alone. Here the averaging over the long term is applied to the wave structure function appearing in the exponent of $\langle M(\omega)_A \rangle_{ST}$. Thus,

$$\left\langle M(\omega)_A \right\rangle_{LT} \approx \left\langle M(\omega)_A \right\rangle_{ST} \left\langle M(\omega)_m \right\rangle_{LT} ,$$

or

$$\exp\left\{-\frac{1}{2} D_w(\omega)\right\} \approx \exp\left\{-\frac{1}{2} D_w(\omega) \left[1 - 1.026 \left(\frac{\lambda\,\omega}{D}\right)^{1/3}\right]\right\} \left\langle M(\omega)_m \right\rangle_{LT} , \tag{80}$$

or

$$\left\langle M(\omega)_m \right\rangle_{LT} \approx \exp\left\{-\,.513 \left(\frac{\lambda\,\omega}{D}\right)^{1/3} D_w(\omega)\right\},$$

but

$$D_w(\omega) = 2.91\,(4\,\pi^2)\,\lambda^{1/3}\,\omega^{5/3}\,\sec \int_0^\infty C_N^2(h)\,dh .$$

Hence,

$$\left\langle M(\omega)_M \right\rangle_{LT} \approx \exp\left\{-\,4\,\pi^2\,\omega^2\,1.49\,D^{-1/3}\,\sec\theta \int_0^\infty C_N^2(h)\,dh\right\}. \tag{81}$$

Contents of the exponential are within a constant factor equal to the expression for one-dimensional image motion variance, σ_m^2 , derived earlier.

Accurate determination of long-term MTF affords the observer a unique opportunity to specify optical performance of the atmospheric channel. Here with one result, independent of the optical system used to determine it, resides a powerful tool for predicting the effects on larger and more complicated systems. In the following two chapters, the experimental part of this research will be discussed and data presented. An attempt will be made to construct a turbulence profile. The strength and shape of this profile remains as the largest single unknown in all of the preceeding theory.

CHAPTER IV

ACQUISITION OF EXPERIMENTAL RESULTS

Stellar Image Monitor Apparatus

Experimental data for this thesis research is provided by a device developed by the author and fellow workers at Goddard Space Flight Center during 1968 and 1969. It was designated the Stellar Image Monitor and was designed to provide quantative data for optical site selection. The Stellar Image Monitor, or SIM, is based on a design published by Ramsay[38] and a technique described by Lindberg[39]. Ramsay performed some experimental work with starlight and later Coulman[40, 41] used the device extensively for horizontal optical propagation studies. SIM hardware produces three analog voltages containing information on image intensity, size, and motion. These voltages can be analyzed for the desired statistics of the stellar image. The heart of the device is a modulation transfer function measurement performed by square-wave modulating or chopping in the telescope focal plane. Chopping is performed at a selected but variable spatial frequency. Operation at various spatial frequencies, detection of the chopped light, and electronic processing yield various points for an MTF curve. Image intensity is monitored by low-pass filtering of the chopped signal. Image motion information is derived from electrical phase comparison of signals generated in chopping the stellar image and a reference light source. The Goddard device differs from the original Ramsay design in the way spatial frequency is varied, in electronic processing, and in data collection and reduction. Data in the form of analog voltages is recorded in the field on magnetic tape. Off-line processing by digital computer results in a statistical record of the recorded data, facilitating comparison with theoretical analysis presented in the previous chapters. Data results presented in this Chapter were obtained between fall 1968 and spring 1969 while the SIM was being field tested at the Goddard Optical Research Facility. The device is presently in an operational program of site evaluation at the Smithsonian Astrophysical Observatory at Mt. Hopkins, Arizona. In reporting results, a concentration will be placed on those deemed most effective in estimating strength of turbulence along the vertical path and in testing the theory. Figure 3 illustrates the experimental concept and Figures 4 through 6 are photographs of the equipment used.

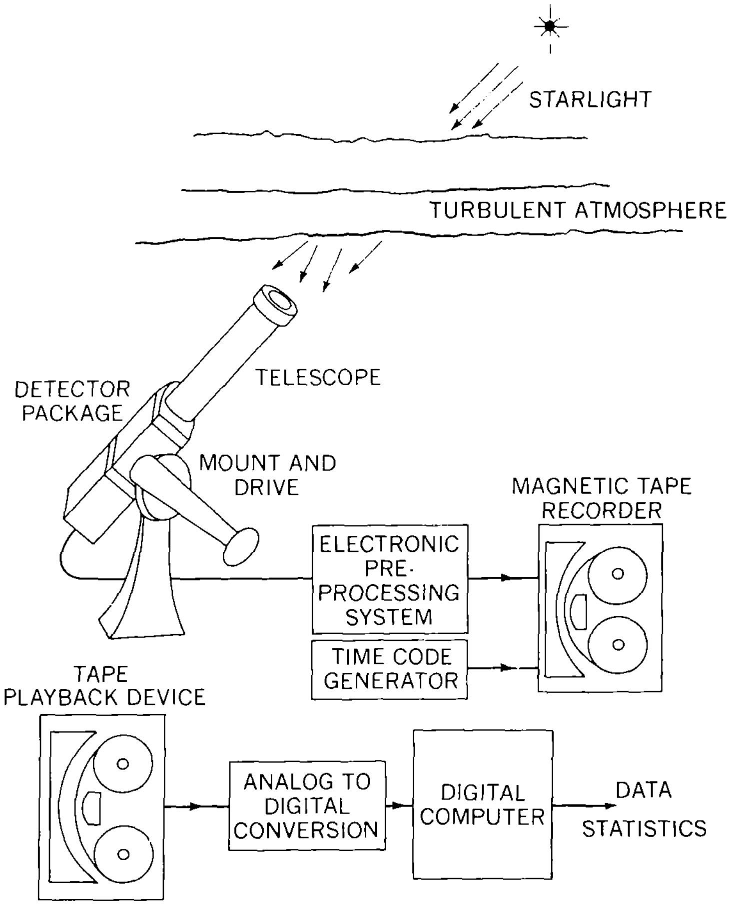

Figure 3. Stellar image monitor experiment concept

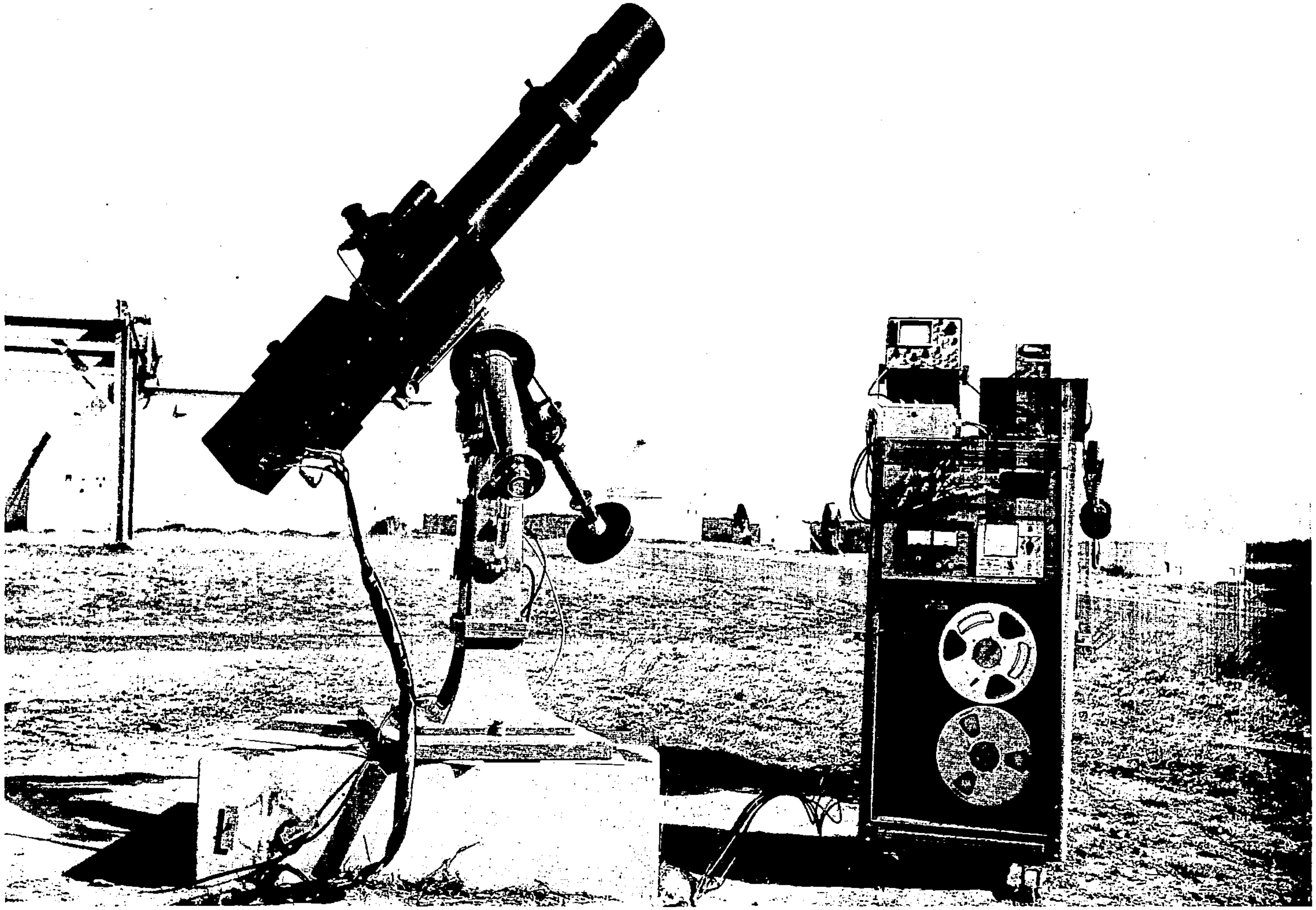

Figure 4. Stellar image monitor field equipment

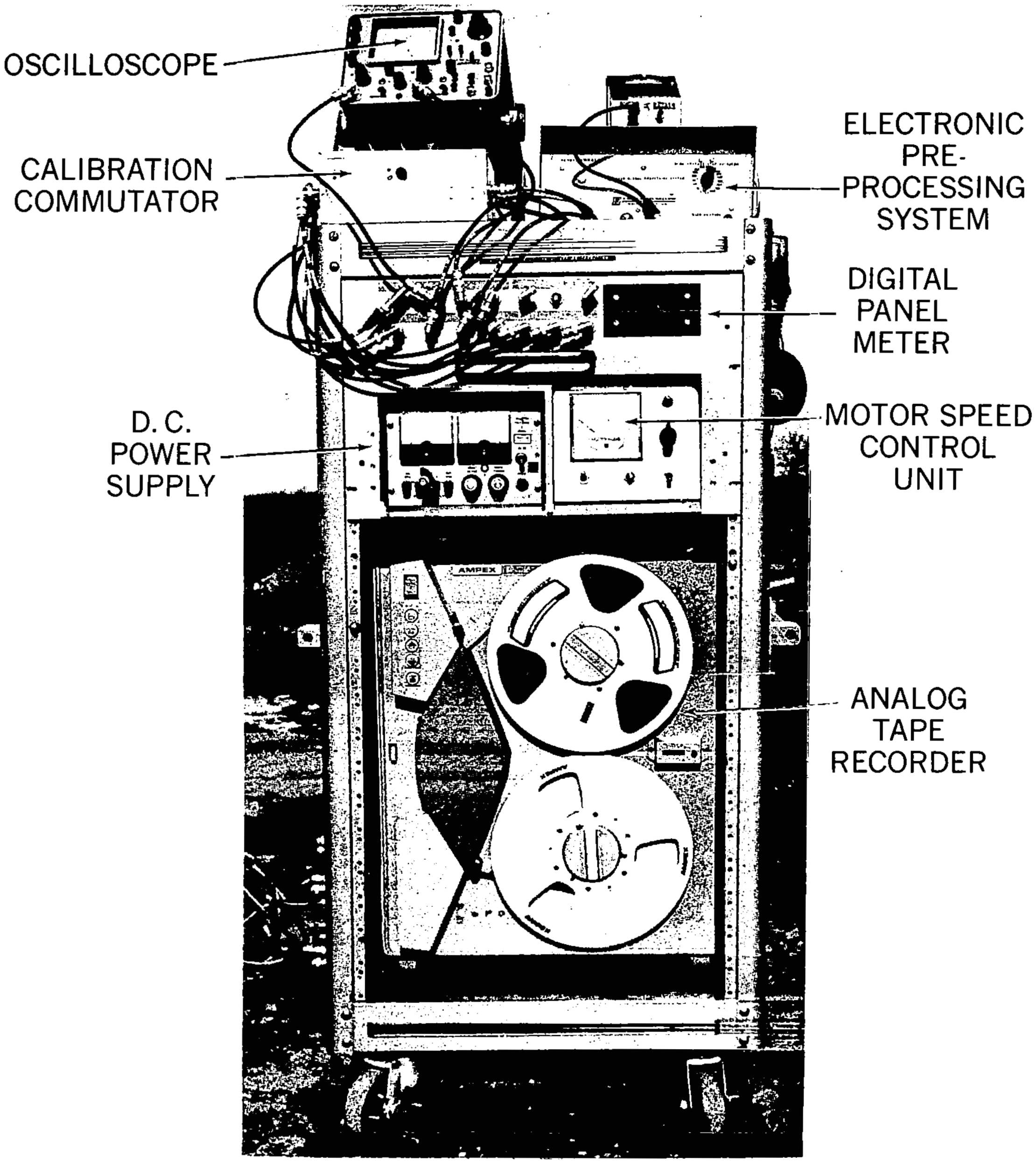

Figure 5. Detail of electronic data collection equipment

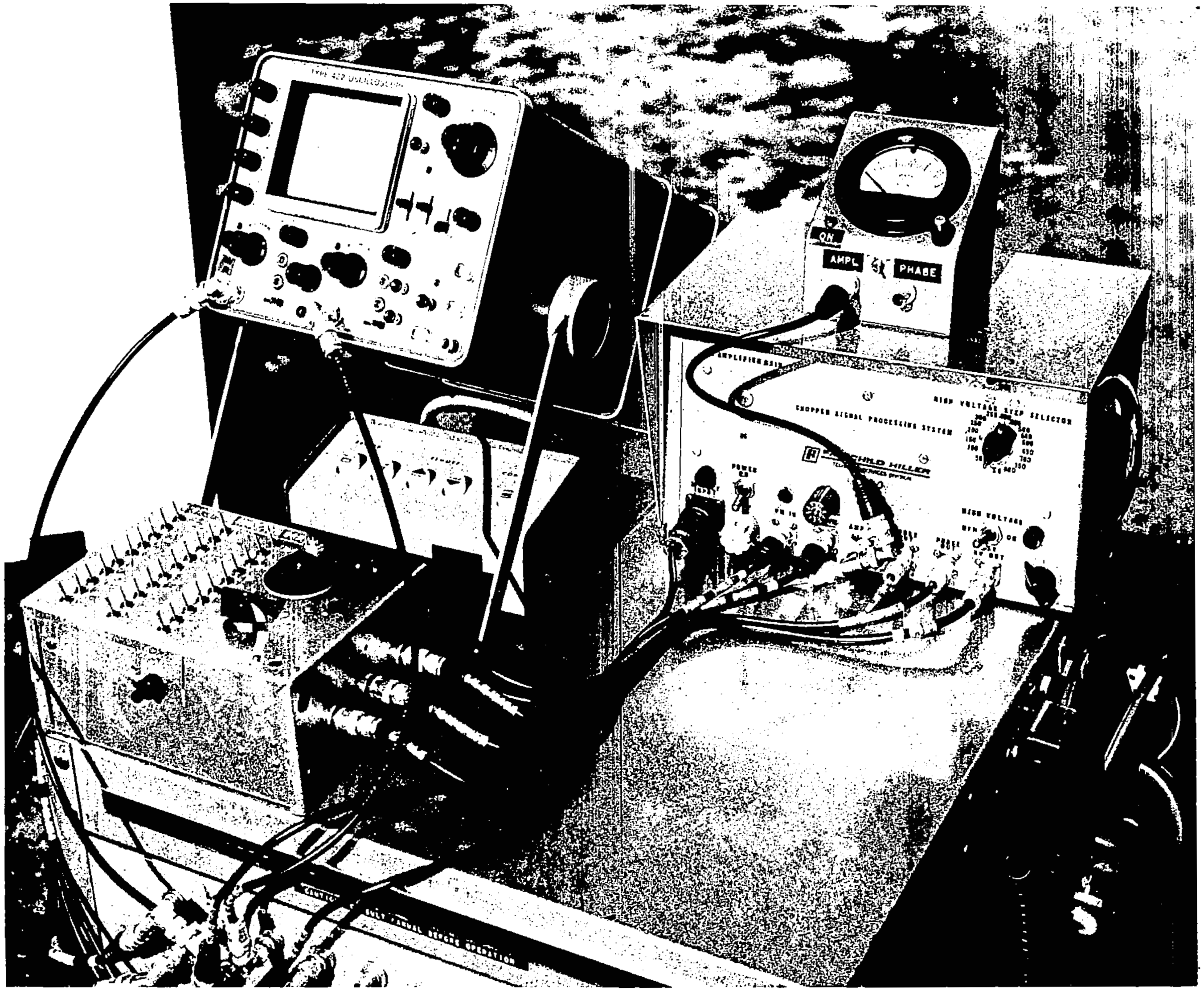

Figure 6. Detail of electronic data collection equipment

In the SIM, starlight is collected by a 6-inch diameter doublet lens system of 48-inches focal length. Figure 7 indicates the optical system components. As converging starlight enters the experiment package, it encounters a partially silvered mirror. This surface, acting as a beamsplitter, allows 30 percent of the light to pass through and reflects 60 percent. Transmitted light enters a pentaprism and is directed through a corrector plate to focus on a ring and crossline reticle. The field-of-view corresponding to the ring's diameter is 14 minutes of arc. Observation of the stellar image on the reticle allows pointing of the telescope to insure on-axis operation. Light reflected by the beamsplitter is reflected again by a front surface mirror and allowed to come to focus. A microscope objective serves as relay optics to focus an enlarged stellar image on a rotating glass disk. An eyepiece and mirror assembly mounted in a sliding tube are used to visually check image quality and insure proper alignment of the image on the glass disk. The disk is composed of alternate clear and opaque pie-shaped sectors as detailed in Figure 7. Each sector subtends one-half degree. The pattern was produced at Goddard by photographic-reduction and etching from a machine-drawn original. The disk is belt driven from a D.C. motor-servo system at a constant rate of 517 rpm. Speed regulation is better than 0.5 percent. Light passing through the disk is thus square-wave modulated with a time frequency of 3.1 KHz, determined by motor speed and number of sectors on the disk. The spatial frequency of chopping is inversely proportional to the distance from the center of the disk and is determined by sector width at a given distance. Since one clear and one opaque sector determine one cycle of chopping, the spatial frequency in cycles per millimeter is the reciprocal of the width of two sectors. Spatial frequency can be made independent of lens parameters by multiplication by system focal length. Cycles per millimeter become cycles per radian field-of-view or cycles per arc second. Starlight is brought to a focus one inch from the center of the disk.

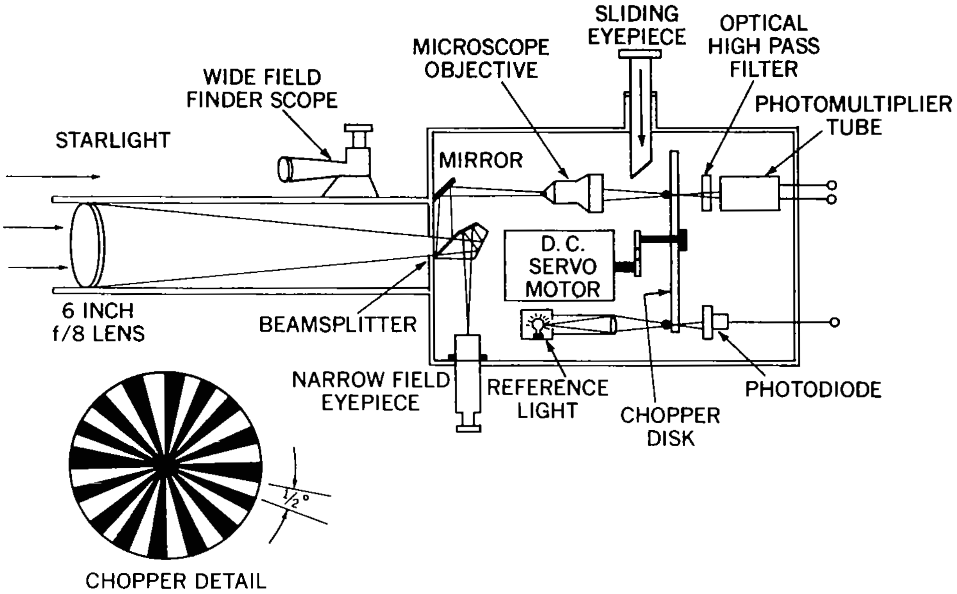

Figure 7. Optical system and detector package

For unity power relay optics the spatial frequency of chopping is 2.26 cycles per millimeter or 0.0134 cycles per arc second. Higher powers effectively increase the spatial frequency by enlarging the image on the disk. Below are listed the linear increases in spatial frequency achieved with various powers of microscope objective.

Light transmitted by the disk passes through an optical bandpass filter and is received by a photomultiplier tube. The photomultiplier tube is an EMI Model 9558B with S-20 response. The filter is a Corning glass filter, Number CS 3-71. The combined spectral half width is approximately 1200Å centered at 5000Å (Figure 8).

Table 1

Microscope Objective Power and Spatial Frequency

Microscope Objective Power	Spatial Frequency (Cycles/Arc Second)
1.0	0.0134
2.6	0.0348
3.5	0.0469
4.0	0.0536
6.0	0.0803
10.0	0.134
21.0	0.281
45.0	0.602
60.0	0.803
98.0	1.31

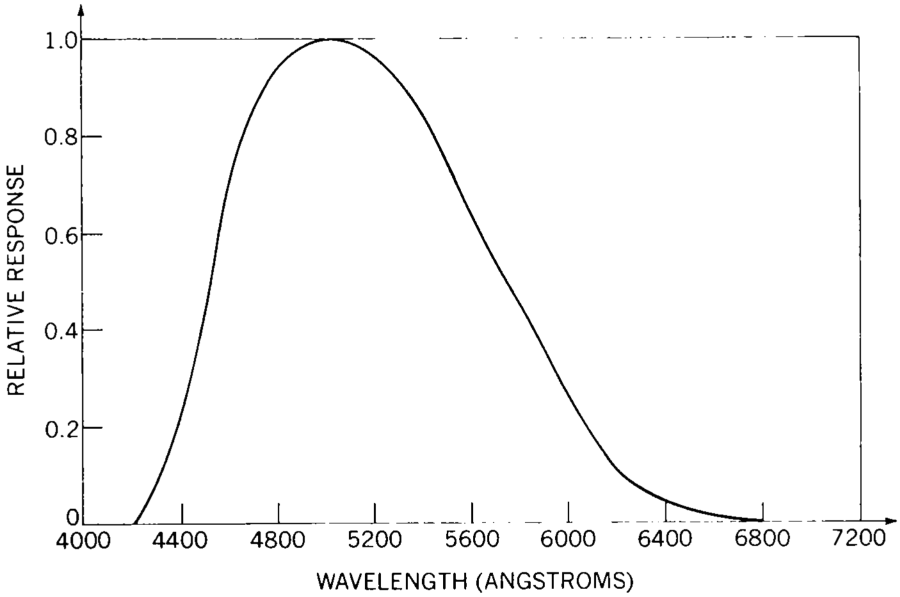

Figure 8. Combined relative spectral response

Light from a small D.C. powered lightbulb is also focussed on the disk to act as a phase reference source. A thin glass plate in the converging light from the bulb can be tilted to adjust the position of this image on the disk. Chopped light is received by a PIN-10 photodiode. A field effect transistor preamplifier and biasing network prepares the photodiode signal for entry into the electronic preprocessing system. The photomultiplier signal is developed across a one megohm load resistance and unity gain preamplifier stage.

Electrical signals from the two detectors are fed into an electronic preprocessing system (Figure 9). The main function of this device is to produce three voltages containing information on image intensity, modulation index, and motion. Operational amplifiers are the primary circuit constituents. The entire instrument is D.C. powered by a regulated power supply providing 27 volts at approximately 0.2 amps. Solid state voltage regulators provide the plus and minus 12 volts required for operational amplifier biasing. In addition, a programmable D.C.-to-D.C. converter provides up to 2000 volts for the photomultiplier tube.

The positive going input from the photomultiplier preamplifier stage is in the form of an amplitude-and frequency-modulated square wave at the chopping frequency, 3.1 KHz. This signal and the photodiode signal are not perfect square waves since image size is not negligible compared with sector width. Only the fundamental sine wave component of the square wave is of interest, however. As shown in Figure 9, the photomultiplier signal proceeds through two inverting D.C. amplifier stages. The first has a gain of 10 and the second incorporates a variable gain from one of 20. At this point, the amplified signal proceeds two ways. The first path is through a low-pass filter of the multiple feedback

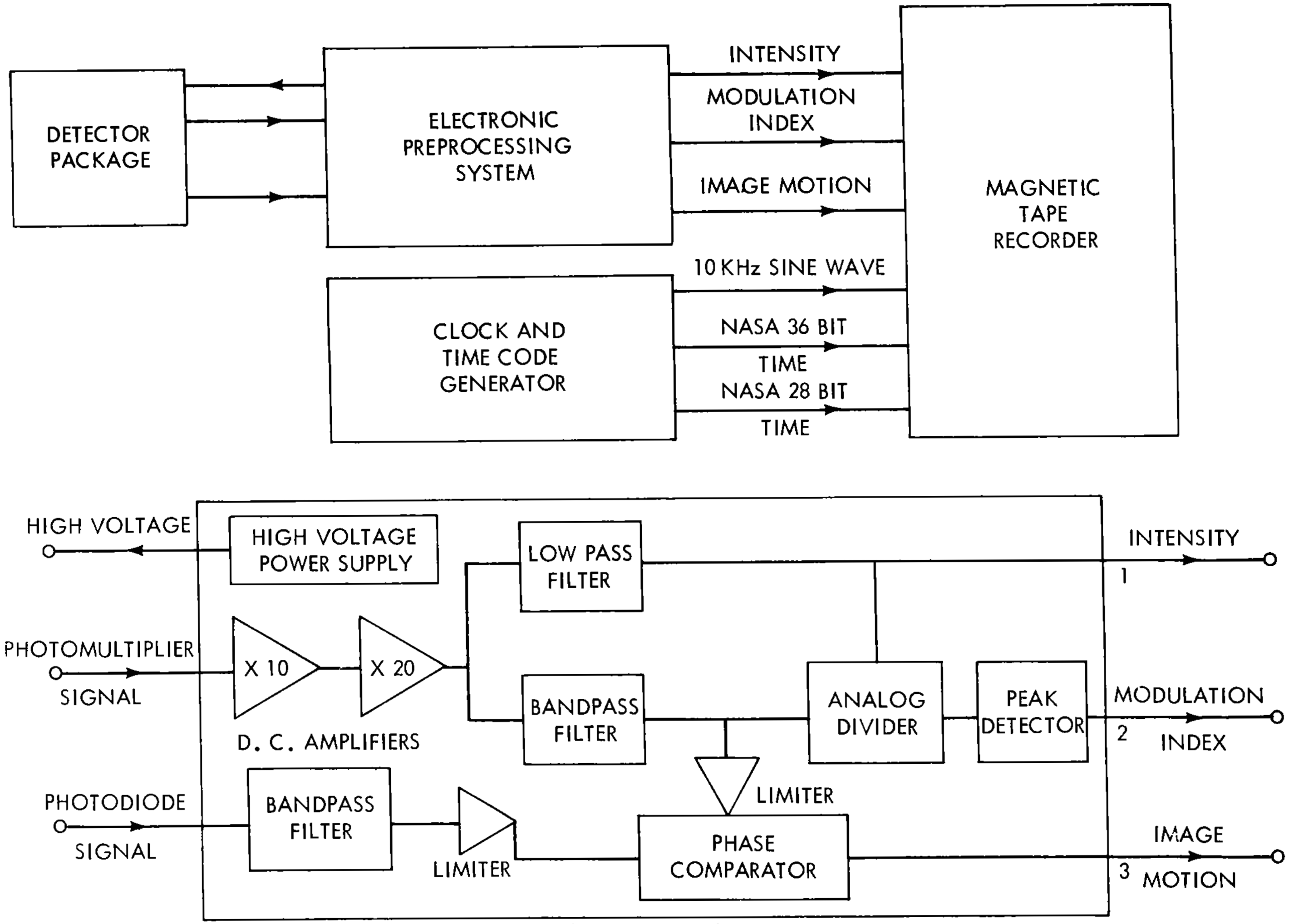

SYSTEM DETAIL

Figure 9. Electronic preprocessing system

design having a corner frequency of 200 Hz. The filter's output is just the measurement of total image intensity and its scintillation. This D.C. or low-frequency information output 1, is also used in the determination of modulation index. The second path is through a multiple feedback bandpass filter centered at the chopping frequency. This frequency belongs to the fundamental sinusoidal component in the square wave. The 3-db bandwidth of the filter is plus or minus 200 Hz around the center frequency. An analog divider receives the outputs of both filters and performs the operation A.C. divided by D.C. The output of the divider is the normalized chopping frequency component, that is, the strength of the component with respect to D.C. As the image size grows larger due to turbulence or as spatial frequency is increased, the A.C. component suffers a reduction. Size changes affect only the A.C. component while intensity changes or scintillation are present in both A.C. and D.C. components and cancel out in the division process. The divider's output is received by a peak detector which produces a D.C. voltage, output 2, proportional to the modulation index or relative strength of A.C. to D.C. Fluctuations in modulation index can be followed from D.C. to the corner frequency of 200 Hz. If the peak value of A.C. is equal to the D.C. signal strength, the modulation index is 1.0.

Motion of image center of gravity is determined by phase comparison of signals at the chopping frequency, 3.1 KHz, from the two detectors. As the stellar image moves on the chopping disk, it produces a waveform shifted in phase with respect to that from the phase reference source with its stationary image. The preamplified reference signal from the photodiode is first sent through a bandpass filter identical to that used in processing the phototube signal. The outputs of both bandpass filters are sent through limiter stages to provide good, clean square waves. An integrated-circuit phase comparator receives the square waves and outputs a pulse train whose duty cycle is proportional to the relative phase of the signals. An RC averaging network with response from D.C. to the corner frequency of 200 Hz measures the duty cycle. Relative phase of the two signals is just the relative position of the two images on the disk along a direction perpendicular to a disk radius. Thus, output 3 becomes a voltage proportional to one-dimensional motion of stellar image center of gravity.

The results of electronic and optical calibration tests of the preprocessing system are given in a following section. These tests were necessary to insure proper operation of the electronics and to relate the voltage outputs to parameters specifying image quality.

In order to preserve the output data of the electronic preprocessing system in a form suitable for data analysis, recordings are made on magnetic tape. For this purpose, an Ampex FR-1300 portable instrumentation tape recorder was incorporated into the system. This is a seven track machine equipped in a standard IRIG configuration for one-half inch wide magnetic tape. The three outputs of the electronic preprocessing system have bandwidths from D.C. to 200 Hz. The D.C. requirement means a frequency-modulation (FM) recording scheme must be used. Time signals are also recorded in order to properly characterize and identify the data. The NASA one-per-second and one-per-minute binary time codes are the ones used. These can be recorded in the direct (AM) mode. Recording is done at a tape speed of 7.5 inches per second. The FM and AM record bandwidths are from D.C. to 2.5 KHz and from 50 Hz to 38 KHz, respectively. A 10 KHz sine wave is also recorded in the direct mode as a reference signal. Tape speed errors made in data taking can be eliminated during automatic data processing by using the 10 KHz reference signal. Such errors would result from fluctuations in power-line frequency. Signal-to-noise ratio specifications for the tape recorder are greater than 40 db at the tape speed used.

Operation of the Stellar Image Monitor Experiment involves nighttime stellar observations at various zenith angles, azimuths, and different times of night. Two operating personnel are required, one to adjust telescope pointing and optical alignment and the other to monitor the electronics and operate the tape recorder. In acquiring a star, successive use is made of a wide field viewfinder and narrow field, high-power eyepiece. This insures operation of the telescope on-axis. The focussing and centering microscope objective holder is then used to bring the stellar image to the correct focus and position on the chopper wheel. This process is monitored by the sliding eyepiece. After proper alignment is achieved, the eyepiece is removed and starlight enters the detector package. Once the photomultiplier high voltage control and D.C. amplifier gain have been adjusted for the proper intensity output voltage, the instrument is ready for data recording.

Data-taking procedures are tailored closely to the demands of data reduction. To this end, calibration voltages, a star identification code, and background runs are recorded on magnetic tape along with the data, time, and reference signals (see Figure 9). A voice-edge track is used to note experimental parameters such as spatial frequency, telescope aperture, photomultiplier tube high voltage, and amplifier gain. Data taking is divided for convenience into four distinct categories. A tape is the largest category. It is the contents of one reel (2,500 feet) of magnetic tape and may include data from several nights, the second category. The third level is called a star. It includes all data taken in succession with a particular stellar source. Included here may be from one to ten data runs, the final category.

A data run begins when the tape recorder is turned on and ends with tape recorder off. It is characterized by a three-digit data run number and a particular spatial frequency. Nominal operation would include five data runs per star, each conducted at a different spatial frequency. Below is listed the format of a data run. An example is given in Figure 10.

Table 2

Data Run Format

Event Number	Event	Length (Seconds)
	START RECORDER	
1.	Tape leader at ground potential	20
2.	Positive 6 volts calibration	10
3.	Ground potential	5
4.	Negative 6 volts calibration	5
5.	Star number hundreds digit	3
6.	Star number tens digit	3
7.	Star number units digit	3
8.	Data	10 to 600
9.	Defocus data	5
10.	Background data	5
	STOP RECORDER	

The first seven events are fed automatically to the tape recorder by a commutator arrangement. The commutator selects the desired D.C. voltage level for the specified length of time. Tape leader allows time for the tape recorder transport mechanism to come up to speed and stabilize. Known calibration voltages are recorded to provide a voltage standard in data reduction. The three star numbers are the hundreds, tens, and units digits that comprise the number assigned to a particular star. This number may be found in Apparent Places of

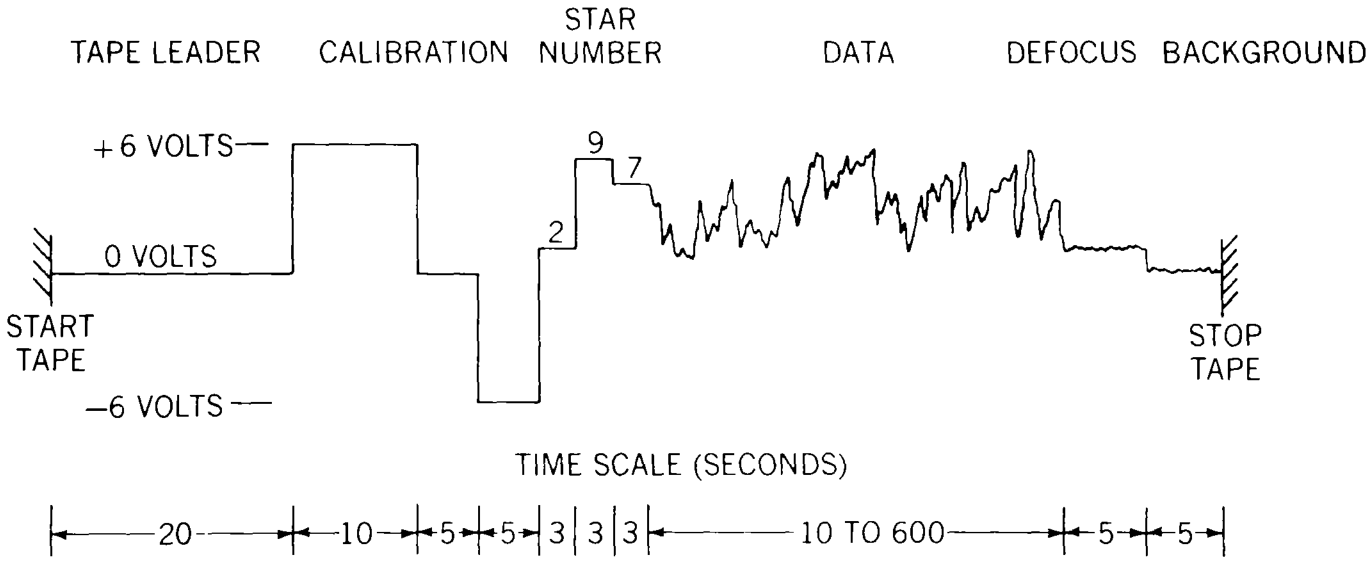

Figure 10. Data run format

Fundamental Stars. Each digit is a certain percentage of plus calibration voltage. For example, the star number 297 would comprise voltage levels 20, 90, and 70 percent, respectively, of plus calibration. Actual star data is taken from 10 seconds to 10 minutes. Defocus data is generated when the telescope operator deliberately defocuses the stellar image on the chopper wheel. This is used to characterize the modulation-index data. Background data requires the operator to point the telescope so that the star is just beyond the field-of-view. Thus, all the effects of stray light, sky background, and electronic offset can be recorded.

Data from the three outputs of the SIM is recorded simultaneously in each data run. Time and reference signals are recorded continuously without the calibration voltages and star code. Below is a listing of the seven tracks of the magnetic tape recorder, their functions, and modes of recording.

Table 3

Tape Recorder Format

Track Number	Function	Record Mode
1	Spare	FM
2	10 KHz reference	AM
3	Image motion data	FM
4	Intensity data	FM
5	Modulation index data	FM
6	BCD time code 36 bit	AM
7	BCD time code 28 bit	AM

The electronic equipment described above is mounted in a standard 5-foot instrumentation rack as shown in detail in Figures 5 and 6. The following items are included:

(1) Electronic preprocessing system.

(2) Calibration voltage commutator.

(3) Tektronix type 422 oscilloscope.

(4) Newport Labs series 200 digital panel meter.

(5) Trygon HR40-3B D.C. power supply.

(6) Electro-Craft E-650 motor speed control system.

(7) Ampex FR-1300 instrumentation tape recorder.

The oscilloscope and digital panel meter are used to monitor signal levels during data recording. Time and reference signals must be fed into the rack from an external time code generator.

The three outputs of SIM are randomly fluctuating voltage levels representing optical fluctuations in the stellar image being monitored. Similar to the atmospheric mechanisms responsible, these optical fluctuations have a large dynamic range and periods as short as several milliseconds. In Figure 11, sample chart recordings of each of the three data tracks are presented. Clearly, one must turn to statistics in order to characterize the data. Consideration must be given to averages, variances, correlations, and power spectrums.

Once data has been recorded on magnetic tape, the first step in data reduction converts the information into a digital format. For this, the facilities of the Information Processing Division at GSFC are used. Analog data tapes are played back through an analog to digital (A/D) conversion unit and digital tapes are produced. A/D sampling is at a rate of 4 KHz. A sample is taken every quarter millisecond. The data tracks are sampled sequentially with the net result that all of the three outputs of the SIM plus a spare fourth track are sampled every millisecond. Fundamental sampling theorems require that the sampling rate be twice the highest frequency component in the data. This insures correct

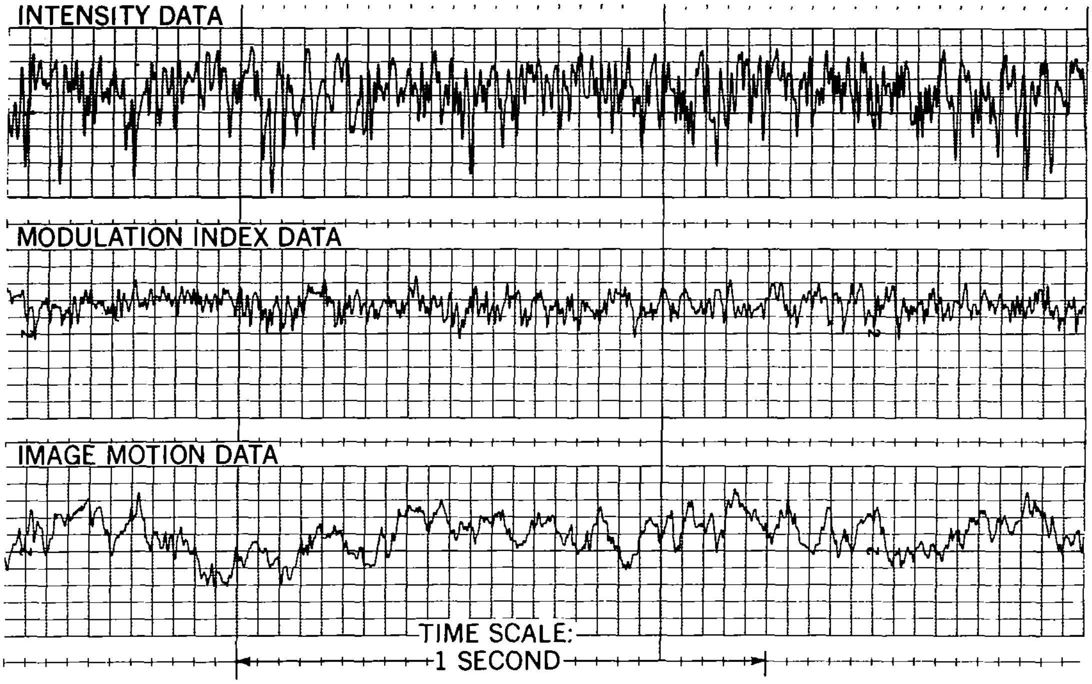

Figure 11. Typical data signals

representation in digital form of the original data. Sampling 1000 times per second allows the data to contain frequencies as high as 5000 Hz. This is more than enough to contain the 200 Hz bandwidths of the SIM electronics and, from previous experience, the expected bandwidths of optical fluctuations. The 36-bit one-per-second time code is also digitized and used primarily as a bookkeeping device. The digital tape contains information in binary coded decimal format and is ready for computer processing.

Processing is done on an IBM system 360/91 computer through programs written in the Fortran IV language. The following description of data analysis concentrates not on specific program instructions but rather on the method of statistical analysis. This method conforms to standard practices in statistical analysis. The method is best examined by following a sample data run.

The first information input to the computer for each data track is a series of samples of the positive, zero, and negative calibration voltages v_1, v_2, and v_3. As mentioned previously, $v_1 = +6.0$ volts, $v_2 = 0.0$ volts, and $v_3 = -6.0$ volts. The computer is programmed to determine average values x_1, x_2, and x_3 of the samples for each calibration voltage. A linear relation is assumed to exist between actual voltage v and sensed value x, that is,

$$v = A\,(x - B).$$

Two of the resulting three simultaneous equations can be solved for scale (A) and tare (B) factors. This calibration is used later in the data run to assign true voltage readings to the data. It serves to eliminate inevitable gain changes and D.C. offsets present in the recording and reproducing process from magnetic tape. The computer is next presented with samples of the three digit star number. Once again, average values are determined and are expressed in percentages of positive calibration. This serves to identify the star number. The computer has stored a list of over 100 stars according to star number, right ascension, and declination. Use of the following information allows calculation of stellar zenith angle and azimuth:

(1) Time of data run.

(2) Sidereal time at Greenwich, England, for zero hours Universal Time on the day of observation.

(3) Stellar coordinates, right ascension and declination.

(4) Longitude and latitude of observation site.

Data samples then begin to enter the computer. If 20 seconds of data is to be analyzed, the computer will be presented with a series of 20,000 data points for each of the three tracks. All statistics subsequently calculated from the data points will be time averaged over the length of the data run (20 seconds). It is necessary to average data over a time long enough to assure good statistical accuracy. Estimates based on equivalent bandwidth and resulting number of independent samples suggest at least a 10-second averaging time for SIM data. On the other hand, if averaging time is too long, atmospheric or other experimental conditions can change significantly, destroying the meaning of the data. Twenty seconds seems to be a reasonable compromise.

Each data point is assigned a voltage level, v, according to scale and tare factors determined by calibration. Method of analysis is then split into two main procedures. In the first procedure, the voltage range that includes all the data is divided into a large number, K, of class intervals. The width, Δv, of the class interval, i, may be chosen at will but has as its effective lower limit the voltage resolution of A/D equipment. The following are typical parameter values:

voltage range = 0.0 to 10.0 volts,

$K = 500$,

and

$\Delta v = 0.02$ volts.

The computer tabulates the number, $n(v_i)$, of occurrences of the data record in each class interval and also the percentage occurrences, $p(v_i)$. This in effect establishes a probability density histogram, $P(v_i)$, representing in digital form the probability density function, $P(v)$, by

$$p(v_i) = \frac{n(v_i)}{N},$$

where N = total number of data samples. Then,

$$P(v_i) = \frac{p(v_i)}{\Delta v}$$

and

$$\sum_{i=0}^{K} P(v_i)\,\Delta v = 1 \ .$$

The cumulative density histogram is related to $P(v_i)$ by

$$C(v_j) = \sum_{i=1}^{j} P(v_i)\,\Delta v \ .$$

This represents the total probability for voltage less than or equal to the given voltage, v_j. Probability density and cumulative density are related theoretically by

$$P(v) = \frac{d\,C(v)}{dv}$$

and

$$C(v) = \int_{-\infty}^{v} P(v)\,dv \ .$$

The computed probability density function is used to determine means, variances, and higher moments of the data record. Thus,

$$\text{Mean} = \bar{v} = \sum_{i=1}^{N} v_i\,P(v_i)\,\Delta v$$

$$j^{th} \text{ moment about the mean} = \sum_{i=1}^{N} (v_i - \bar{v})^j\,P(v_i)\,\Delta v$$

$$= m^j ,$$

where $j = 2$ is the variance, σ^2. The sample mean and sample moments thus computed are not unique for a given sequence of N data points, since they are determined by choice of voltage interval endpoints and by number of class intervals.

The parameters coefficient of kurtosis, k, and skewness, s, help to characterize the probability density function. These are given by

$$k = \frac{m^4}{\left(m^2\right)^2} - 3.0$$

and

$$s = \frac{m^3}{\left(m^2\right)^{3/2}} .$$

Coefficient of kurtosis relates to the width of the distribution and skewness relates to its symmetry. For a Gaussian distribution, both k and s will be zero. Random voltage statistics can best be summarized in one parameter, coefficient of variance, where

$$\text{Coefficient of variance} = \frac{\left(\sigma^2\right)^{1/2}}{\bar{v}} .$$

This parameter has the form of a percentage modulation. It is the ratio of standard deviation of the fluctuating signal to its average value.

The second main direction of analysis is based on data time series, the succession of data samples maintained in their original positions as a function of time. The basic tool in this analysis is the sample autocorrelation function,

$$R(\tau) = \frac{1}{T-\tau} \int_0^{T-\tau} v(t)\, v(t+\tau)\, dt ,$$

where

τ = lag time,

T = length of data sample,

and

v(t) = voltage level at time t.

The autocorrelation function for random data describes the general dependence of the values of the data at one time on the values at another time. An estimate of the autocorrelation between values of v(t) and times t and $t + \tau$ is just the product of the two values averaged over the length of data sample. Here, τ is the lag time or separation time. For computer analysis, the discrete representation is used. Thus,

$$R(\tau) = R(\ell\Delta t) = \frac{1}{N-\tau}\sum_{i=0}^{N-\tau} v_i' \, v_{i+\ell}' ,$$

where

ℓ = lag number = 0, 1, 2, . . . m,

m = maximum lag number,

N = total number of samples,

t = interval between samples,

and

$v_i' = v_i - \bar{v}$ = voltage level for the i^{th} sample minus the average voltage level.

For a good estimate of $R(\tau)$ m should be chosen one tenth of N or less. Typical parameters are

N = 20,000,

m = 200,

and

Δt = 1 millisecond.

Although $R(\tau)$ is a useful quantity by itself, it is more useful when applied to an estimate of spectral density, G(f), where

$$G(f) \equiv \lim_{\Delta f \to 0} \frac{\sigma^2(f)}{\Delta f} .$$

Spectral density can be thought of as voltage variance per unit bandwidth. In order to proceed from the time domain, $R(\tau)$, to the frequency domain, G(f), we must use the Fourier transform of $R(\tau)$ with respect to τ, so that

$$G(f) = 4\int_0^\infty R(\tau)\cos(2\pi f\tau)\,d\tau .$$

In discrete form for computer analysis, this becomes

$$G(f) = 4\Delta t\sum_{\ell=0}^{m} R(\ell\Delta t)\cos\frac{\pi\ell f}{f_c} ,$$

where

f = frequency (Hz)

and

f_c = 500 Hz = frequency cutoff of data.

The equivalent bandwidth or frequency resolution in this analysis is B_e , where

$$B_e = \frac{2f_c}{m} .$$

For the previously assumed parameters, B_e = 5 Hz. The raw estimate spectral density requires smoothing because the variability of the estimate does not decrease with increased sample size or record length. Smoothing or weighting nonuniformly can be accomplished by multiplication by the Hanning lag window, $D(\ell\Delta t)$,

$$D(\ell\Delta t) = \frac{1}{2}\left(1 + \cos\frac{\pi\ell}{m}\right) .$$

Thus,

$$G(f) = 4\Delta t\sum_{\ell=0}^{\infty} D(\ell\Delta t)\,R(\ell\Delta t)\cos\left(\frac{\pi\ell f}{f_c}\right) .$$

For graphical presentation of spectral density, normalization to unit variance may be employed. The variance of the signal in each frequency interval is divided by variance for the full signal. This insures that all spectral densities will have the same area under the curve regardless of the strength of turbulence fluctuations. This method aids in plotting strong and weekly fluctuating signals on the same graph. The unnormalized plot should be used to facilitate comparison of strength of signal in a given bandwidth for many different data runs.

Although both methods of statistical analysis apply in general to all data from the SIM, each data track must be handled in a particular way. The image intensity track represents irradiance fluctuations of starlight. Voltage produced by the monitor is directly proportional to irradiance, I, optical power per unit area at the receiver. Before the connection can be made, the effect of optical and electronic background must be removed from voltage statistics. The primary effect of background is the introduction of an unwanted D.C. offset into the data. Computer measurement of background data taken at the end of each data run allows the D.C. offset to be subtracted before calculations are made. The dimensionless parameter coefficient of variance, here called CIV, coefficient of irradiance variance, has been the most widely used measure of irradiance fluctuations. The standard format is a plot of $\log_e$ [CIV] versus $\log_e$ [secant (zenith angle)] of the stellar source. This plot is characterized by the diameter of the telescope aperture and, of course, the turbulence state of the atmosphere.

As indicated previously, log-amplitude and, thus, log-irradiance behave in a Gaussian manner. The logarithmic behavior of irradiance is evidenced by a low average value compared to high peaks, often many times the average value but of short duration. Thus, image intensity could be discussed in terms of log-amplitude statistics. Log-amplitude can be written as one-half the natural log of the ratio of instantaneous irradiance, that is, one-half log-irradiance, so that

$$\ell = \frac{1}{2} \log_e \frac{I}{\bar{I}} .$$

$I/\bar{I}$ is just equal to $v_i / \bar{v}$ since the proportionality constant cancels. Thus,

$$\ell_i = \frac{1}{2} \log_e \frac{v_i}{\bar{v}} .$$

Statistics of log amplitude can be computed in the same manner as voltage statistics with the substitution ℓ_i for v_i. Log amplitude variance, σ_ℓ^2, now becomes the central parameter. Summary information is a plot of log amplitude variance versus zenith angle. Spectral densities of both irradiance and log amplitude are particularly important for they reveal much about the atmosphere through their demonstrated dependence on zenith angle and upper altitude wind velocity.

The modulation-index track results in a voltage proportional to the modulus of the optical transfer function for the particular spatial frequency used in data taking. Voltage statistics are appropriate and require only a conversion factor to modulus statistics. Laboratory tests generate a plot of modulus versus modulation index voltage. Modulus is just the depth of modulation of the square wave input to simulate the waveform from the detection of chopped starlight. One-hundred-percent depth of modulation corresponds to a modulus of 1.0. As the depth of modulation is varied, the analog divider and peak detector respond with a change in voltage. Modulus values obtained from this curve are corrected for the effect of electronic and optical background. This is done with average voltage and average background data obtained from the image intensity track. The average value of defocus voltage serves as the zero reference for modulation index voltage. The variance of modulus is read directly from the calibration curve. Data reduction is incomplete without the time series information provided by autocorrelation function and spectral density. This analysis can be performed directly on modulation index voltage. Secant of stellar zenith angle, azimuth, and spatial frequency serve to characterize the data run.

The image motion track may be handled entirely in terms of voltage statistics, since optical phase, image motion, and output voltage of the electrical phase comparator enjoy a linear relationship. Image motion in the telescope focal plane is the result of random deviations or tilts in the angle of arrival of various parts, or all, of the incoming wavefront. These tilts are actually optical phase differences following a Gaussian distribution. Stellar image motion with respect to reference light image causes a change in the relative electrical phase of waveforms from the two detectors. Suitable laboratory calibration yields a conversion factor in volts per arc second for each spatial frequency. Voltage statistics are thus converted to image motion statistics. Present in the image-motion voltage output is a linear drift attributable to telescope tracking error. This is compensated by a computer generated least squares fit of a straight line to the data. The conversion to average image position is meaningless in data reduction, since it is not important to know precisely where the image is but how it fluctuates with respect to a fixed point. The important parameter is image-motion variance, σ_m^2. Either this number or rms value, σ_m, is plotted versus secant zenith angle of the star. The measured motion is only the component perpendicular to the chopper disk radius. Spectral densities of image motion can be scaled directly from voltage spectral densities.

At the conclusion of computer analysis of stellar data for a particular night, a data summary sheet is prepared. The following information is tabulated for each data run. In addition, data for different stars is combined to yield plots of $\log_e$ (CIV) versus $\log_e$ [secant (zenith angle)] and phase variance versus secant (zenith angle). A modulation transfer function is plotted for each star observed at four or more spatial frequencies. This places the data in a form suitable for interpretation.

Table 4

General Parameters for Each Data Run

1. Data run number
2. Star name and number
3. Zenith angle
4. Secant (zenith angle)
5. Log_e [secant (zenith angle)]
6. Azimuth
7. Time interval for data run
8. Spatial frequency
9. Aperture diameter

Table 5

Statistical Summary for Each Data Run

INTENSITY TRACK

1. CIV $= \sigma_v/\bar{v}$ = coefficient of irradiance variance
2. σ_{ℓ}^2 = log amplitude variance
3. $\bar{v}$ = signal mean
4. $\log_e$ (CIV)
5. $\bar{v}_B$ = background mean

MODULATION INDEX TRACK

1. $\sigma_v/\bar{v}$
2. $\bar{v}$ = signal mean
3. $\bar{v}_D$ = defocus mean

IMAGE MOTION TRACK

1. $\bar{v}$ = signal mean
2. σ_m^2 = motion variance
3. σ_m = motion rms

Prior to deployment of the Stellar Image Monitor Experiment in the field, a series of laboratory tests and calibration runs was performed. The first system component to be tested was the electronic preprocessing system. Figures 12 and 13 show measured frequency and phase response of the bandpass and lowpass filter sections. Bandwidths are 3100 ± 200 Hz and 200 Hz, respectively. Frequency response was measured by using a sine wave signal generator in place of inputs from photomultiplier and photodiode. Phase response was measured on an oscilloscope. Filter input and output were applied to the vertical deflection and horizontal sweep respectively. The resulting lissajous pattern displayed on a phase reticle gave readings of phase difference. Gain and linearity tests of the amplitudes were also performed. This served to calibrate the image intensity track.

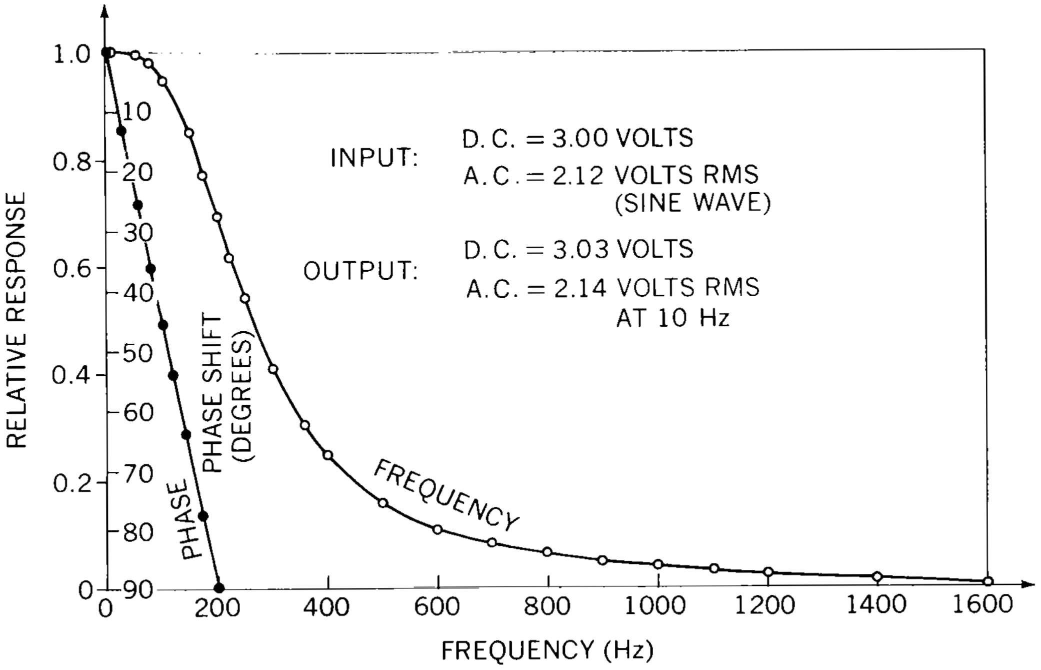

Figure 12. Low-pass filter frequency reponse

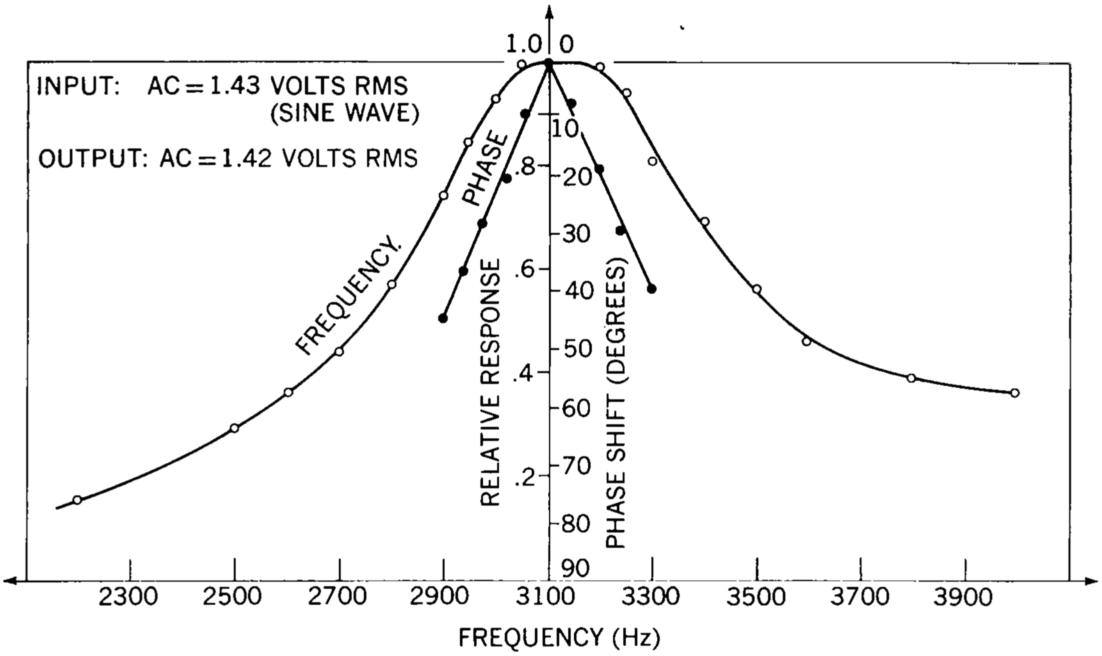

Figure 13. Bandpass filter frequency reponse

Modulation index calibration required a measure of combined response of analog divider and peak detector. Sine waves at the chopping frequency were input in place of signals from the photomultiplier. Modulation index (peak A.C. divided by D.C.) of this input was measured at the input terminals of the analog divider. Measured values of peak detector output voltage for the given modulation index or percent modulation are shown in Figure 14. This curve applies for D.C. voltage in the range -1.0 to -3.0 volts. It should be noted that linearity is not an important consideration in this output since the expected fluctuations will be small compared to their average value. Percent modulation determined from this curve must be multiplied by

$$\frac{\text{D.C.} + \text{BGND}}{\text{D.C.}}\left(\frac{\text{D.C. GAIN}}{\text{A.C. GAIN}}\right).$$

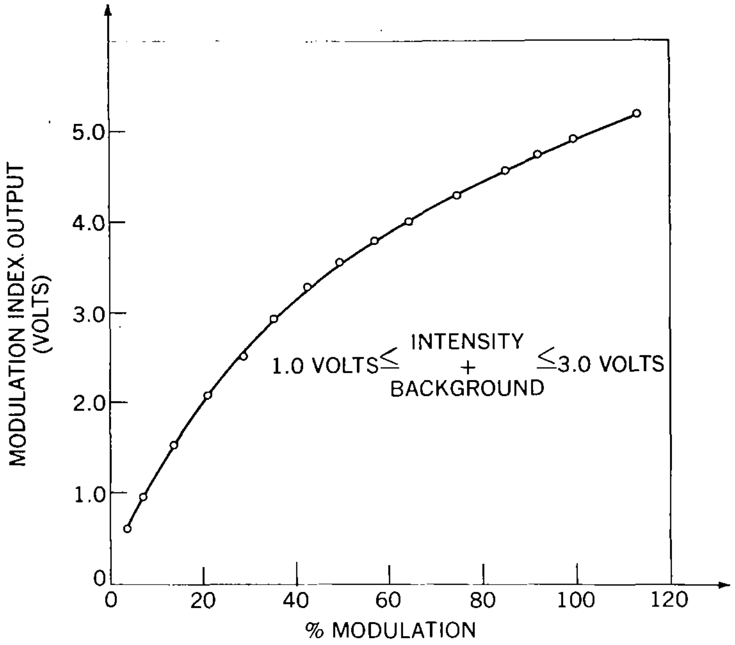

Figure 14. Laboratory calibration of modulation index

to correct for filter gains and any D.C. offset voltage. The symbol BGND, or background, represents this offset. D.C. + BGND information is available from the image intensity track. Filter gains were measured during calibration and their ratio is

$$\frac{\text{D.C. GAIN}}{\text{A.C. GAIN}} = 1.025 .$$

Calibration and testing of the image motion electronics employed an artificial star source, Figure 15. A point source at the focus of an f/10, 20-inch diameter collimating mirror represented the small angular size and parallel light of a star. The point source was either white light or 0.6328 micron red light from a Spectra Physics 131 helium-neon laser. Light from an incandescent lamp filament focused on a variable size pinhole served as the white light point source. In both cases a further reduction in spot size was achieved through microscope objectives.

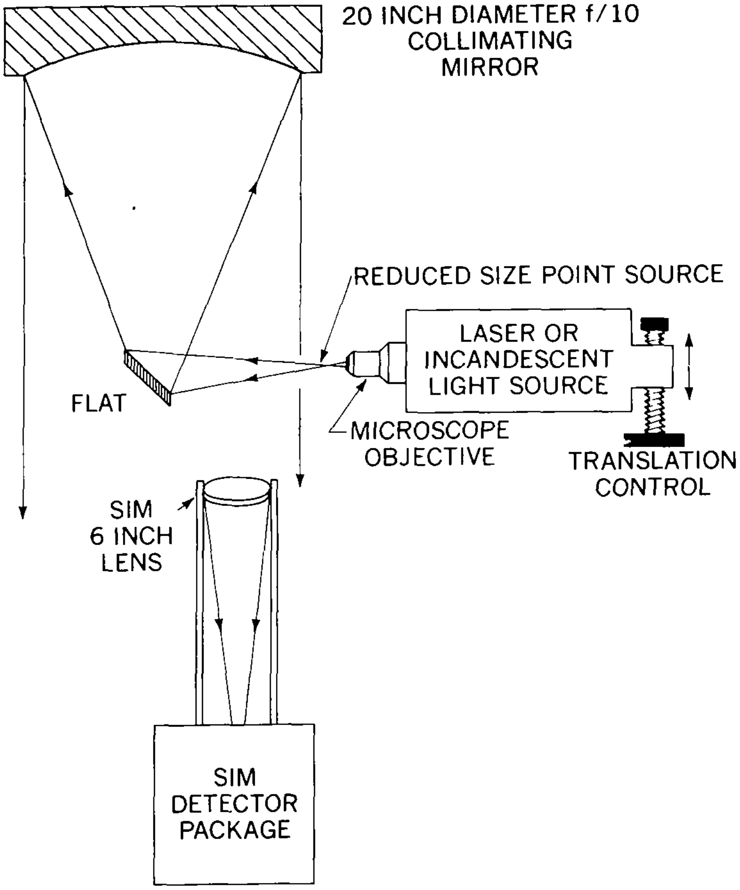

Figure 15. Laboratory optical test setup

Each thousandth of an inch in the focal plane of the 20-inch collimator corresponds to one arc second. Source sizes were kept smaller than the theoretical angular resolution of 6-inch diameter optics.

Collimated light produced by this test setup was allowed to enter the 6-inch diameter optics of the Stellar Image Monitor after traversing about 40 feet of laboratory air space. The point sources were mounted on an optical bench equipped with a translation slide. Movement of the point source in increments of 0.001 inch in the focal plane could be measured there and produced the corresponding number of arc seconds deviation. The D.C. voltage output of the SIM phase comparator was recorded as a function of this arc second displacement. The output of the phase comparator was not a pure D.C. voltage but contained frequency components due to room vibration, air path turbulence, and chopper pattern centering error. The resultant plot, Figure 16, yields the desired calibration factor in volts per arc second. This factor depends linearly on spatial frequency. For the spatial frequency used in the calibration the rms error was approximately 0.1 arc second. It should be noted that the calibration curve is cyclic with a linear response in the mid-range of voltages. Thus in actual data-recording the average value of phase comparator output should be maintained at approximately 3.5 volts. A check on spatial frequency was made by noting the number of cycles of the response curve per arc second. The results agreed with microscopic objective power being used and calculation of chopper wheel sector width.

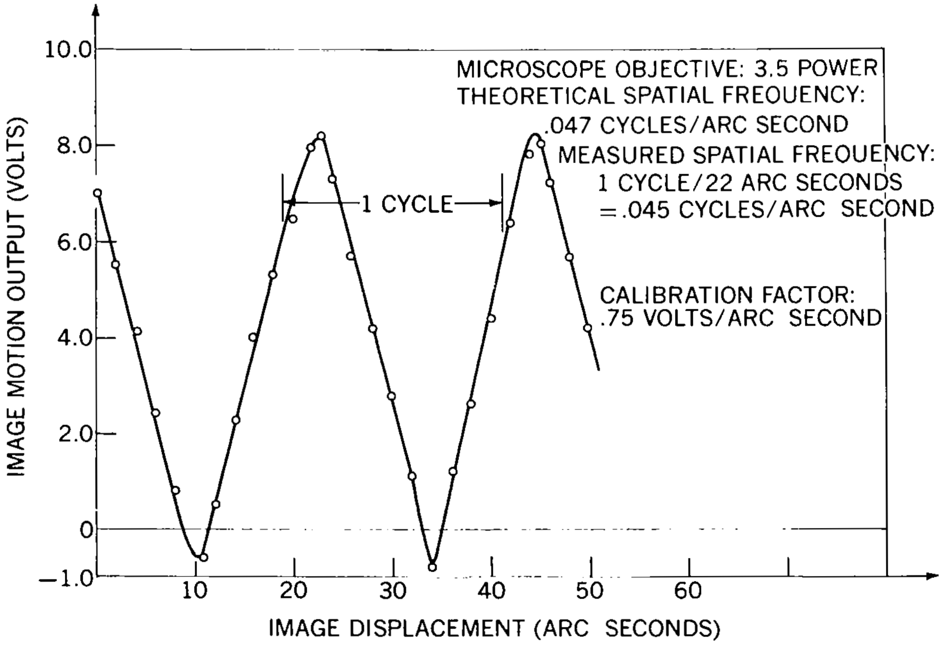

Figure 16. Laboratory calibration of image motion

Using the artificial star system described above optical transfer functions for the SIM in white light and red light were generated (Figure 17). This was done by varying microscope objective power in the SIM. Measured OTF shows a degradation of performance in white light while monochromatic red light performance is close to the diffraction limit. Chromatic aberration causing this effect must be present in the SIM optics since the collimating system is reflective.

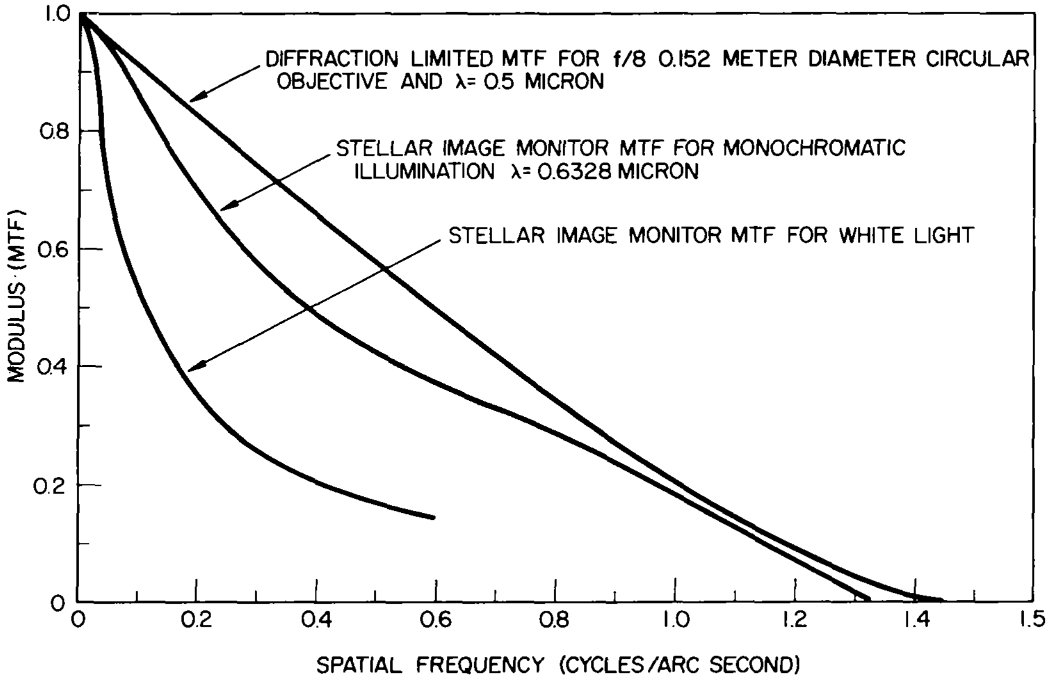

Figure 17. Optical transfer function modulus

Error Analysis

In examination of possible error sources to account for inaccuracies in the analyzed data and spread in data point values, three major factors have been determined. Listed in the order of importance of their effect on the data, they are—

(1) Nonstationarity of the atmospheric processes.

(2) Statistical sample size.

(3) Electronic signal-to-noise ratios.

To even the most casual observer of optical phenomena resulting from atmospheric turbulence, the most striking fact is their nonstationarity. Not only do these phenomena vary from night to day and season to season but over periods as short as several minutes, large departures from stationarity may be observed. In order to characterize the phenomena, the scientist must take samples of finite length and perform statistical analyses. He is limited on the lower end of the time scale by his desire to get enough data to form a reasonable statistical sample and on the upper end by nonstationarity effects and the fact that his equipment can only handle so much data. Estimates of the magnitude of nonstationarity are in dispute but it is generally conceded that the problem is much worse in the ground boundary layer of the atmosphere. Here local terrain effects become dominant. Lawrence, Ochs, and Clifford[42] have reported fluctuations in the ground strength of turbulence, C_N^2, by factors of 10 to 100 over periods of a few minutes. Image size and image motion data are mostly determined in the lower layers and thus may be expected to exhibit the greatest nonstationarity. Irradiance, determined by higher altitude effects where the turbulence field is more uniform, should show a corresponding increase in stationarity. Such assumptions are borne out by experimental evidence. Chart recordings of image motion and image intensity over long periods of time show little apparent change in degree of intensity fluctuations while image motion is observed to periodically increase and then decrease. Measurements of finite record length of these quantities are nevertheless true measurements. Unfortunately, they may bear no relation to measurements of the same quantities taken a few minutes later. Since assignment of error bars to nonstationary data points would be subjective at best, let it suffice to say that the data reported here should be considered typical rather than average and more representative than exact. Noticeable spread in plots of data values, especially for image motion may be due largely to this nonstationarity.

Standard statistical techniques provide a means to estimate the effect of finite data sample length. Data points obtained from the Stellar Image Monitor apparatus are random variables. A succession of these values represent a sample function of the stochastic processes of image intensity, motion, and size. The computed statistics are sample means, variances, and higher moments. For a number, N, of independent observations of a normally distributed random variable, x, it is known that the sample variance obeys a chi-square distribution with n degrees of freedom, i.e.,

$$\frac{n\, s^2}{\sigma_x^2} = \chi_n^2 , \tag{82}$$

where

$n = N - 1$,

S^2 = sample variance ,

σ_x^2 = actual variance ,

and

χ_n^2 = chi-square random variable.

Stellar image position at a particular time is an example of the normally distributed random variable. For weak irradiance fluctuations, as observed in the SIM data, image intensity can also be approximated by a normal distribution. Statistics of chi-square determine the $1 - \alpha$ confidence interval for sample variance, S^2, such that

$$\frac{n}{\chi^2_{n;\,\alpha/2}}\, s^2 \le \sigma_x^2 \le \frac{n}{\chi^2_{n;\,1-\alpha/2}}\, s^2 . \tag{83}$$

That is, the actual variance σ_x^2 is known to fall within the above interval with a confidence of 100 $(1 - \alpha)$ percent. The key parameter that determines the above interval is N, the number of independent samples. In the SIM data reduction, a sample is taken every millisecond. Only some of these are independent, however. N is given by the expression

$$N = 2B_{eq}\,T\,, \tag{84}$$

where

B_{eq} = equivalent white noise bandwidth

and

T = record length.

In turn, B_{eq} can be estimated from the relation

$$B_{eq} = \frac{R_x(0)}{2\int_{-\infty}^{\infty} R_x(\tau)\, d\tau}\,, \tag{85}$$

where

$R_x(\tau)$ = autocorrelation for random variable.

Typical values of $R_x(\tau)$ for image intensity and motion lead to estimates for B_{eq} and in turn N for a given sample record length, T. The value of chi-square for a particular N and α is obtained from standard tables. Results are given below for a 90-percent confidence interval for each signal and a sample record length of 20 seconds.

Table 6

Statistical Error Analysis

	B_{eq}	N	α	$\chi^2_{n;\alpha/2}$	$\chi^2_{n;1-\alpha/2}$
Image Intensity	50 Hz	2000	.10	2104	1896
Image Motion	1 Hz	40	.10	55	26
90-percent confidence intervals $[.95\ s^2 \le \sigma_I^2 \le 1.05\ s^2]$ $[.71\ s^2 \le \sigma_m^2 \le 1.5\ s^2]$					

It is apparent that from statistical considerations alone, a large range in image motion variance should be expected. On the other hand, the true irradiance variance is located in a narrow range (± 5 percent) of the measured value.

In modulation index statistics, the important parameter is mean value. In a similar manner a 90-percent confidence interval can be constructed around the true value of modulation index mean. In this case, the statistic of interest is the student t distribution in terms of random variable t_n, by

$$t_n = \frac{(\bar{x} - \mu_\chi)\sqrt{N}}{s}, \tag{86}$$

where

$\bar{x}$ = sample mean,

μ_x = actual mean ,

n = degrees of freedom = N - 1,

N = no. of independent samples,

and

s = square root of sample variance .

The interval becomes

$$\bar{x} - \frac{s\, t_{n;\alpha/2}}{\sqrt{N}} \le \mu_x < \bar{x} + \frac{s\, t_{n;\alpha/2}}{\sqrt{N}} . \tag{87}$$

The number of independent samples for modulation index is approximately twice that for image motion or about 100 for a 20-second record. Again consulting statistical tables, it is possible to construct the 90-percent confidence intervals in terms of x and S, so that

$$[x - .2\,s \le \mu_x < \bar{\chi} + .2\,s] .$$

In essentially all SIM data, S was found to be less than ±10 percent of $\bar{\chi}$. That is,

$$[.98\,\bar{x} \le \mu_x < 1.02\,\bar{x}] . \tag{88}$$

Thus from statistical considerations, modulation index mean should be attainable with ± 2 percent accuracy.

Tests of the electronic detection, processing, and recording subsystems identified the photomultiplier tube and the tape recorder-reproduce unit as providing the limiting signal-to-noise ratios. Noise sources in the photomultiplier were dark current and shot noise associated with the average stellar photocurrent. Dark current specifications for the EMI 9558B tube used were equivalent to 1.2×10^{-15} watts input. The average stellar signal (first magnitude star) for the full 0.152-meter aperture and optical bandwidth of 0.1 micron was approximately 5×10^{-11} watts indicating no trouble with dark current. A calculation including shot noise indicated that for the same parameters assumed above, the average photocurrent signal-to-noise ratio was 44 db. Thus for this case the analog tape system specification of 43 db was the limiting signal-to-noise ratio. If limiting signal-to-noise was taken as 40 db, instead, the associated noise error bars would be one percent For smaller apertures the shot noise contribution was significant, however. Reduction in aperture to 0.0245 meters results in an average signal-to-noise ratio of 28 db. This is the limiting ratio for smaller aperture data.

Presentation and Discussion of Results

Stellar data reported here was obtained on various clear evenings from fall 1968 to spring 1969. The observation point was the Goddard Optical Research Facility located approximately 4.5 miles from Goddard Space Flight Center in an open field. The Stellar Image Monitor apparatus was placed on a 12-inch high concrete slab about 20 feet from a 20- by 20-foot trailer. This building supplied the necessary power and support capability. Time and reference signals were available from a timing system located in an adjacent building. The telescope and tracking mount were not enclosed by a dome or other structure. Standard alignment procedures were followed to assure accurate stellar tracking. Listed below are the nights on which data was taken and analyzed.

Table 7

Nights of Stellar Observations

Night (universal time)	Date (local time)
269	24 Sep 68
292	7 Oct 68
297	12 Oct 68
301	16 Oct 68
324	18 Nov 68
036	4 Feb 69
037	5 Feb 69
045	13 Feb 69
053	21 Feb 69
063	3 Mar 69
064	4 Mar 69
065	5 Mar 69
077	17 Mar 69
087	27 Mar 69

Only representative data and summary information will be presented and discussed here since it would be impractical to supply everything available. As mentioned previously, a concentration will be placed on that data most useful in examining the theory.

A chart record of a typical data run is shown in Figure 18. Experimental parameters that characterize the data run are listed in Table 8. Timing marks at one second intervals are located along the top. Appropriate calibrations are indicated for the vertical scale on each recording. The modulation index track

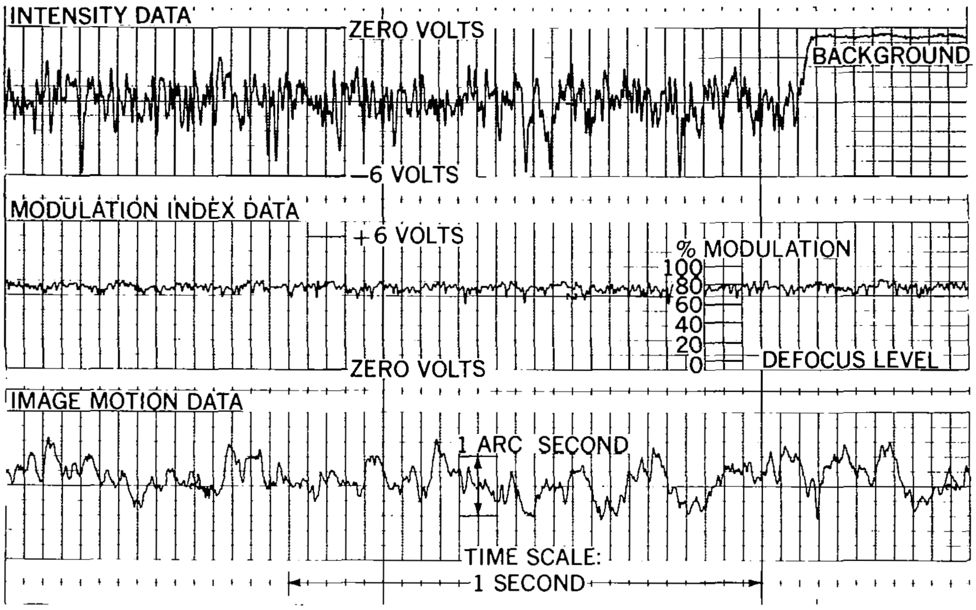

Figure 18. Chart recordings of data run

has indications of percent modulation and the image motion track is calibrated in arc seconds. The corresponding computer statistical record is summarized in Table 8. In addition to the statistics listed, information on the probability density, cumulative density, autocorrelation, and spectral density functions is available for each data run.

Probability density functions for irradiance and image motion statistics of data run 517 are plotted in Figures 19 and 20. Notice the Gaussian shaped curve for image motion and the long trail on the irradiance curve, indicating a log-normal behavior. An accurate test for normal behavior involves plotting the cumulative density distributions on Gaussian probability paper. This is done in Figures 21 and 22 where the ordinate is either log-irradiance in relative units or image motion in arc seconds. The abscissa is constructed so that a normal random variable would plot as a straight line. Both quantities exhibit good fits to normal behavior except for edge effects where system noise and dynamic range constraints become important. The slope of these curves may be used to calculate log-amplitude variance and image motion variance.

Table 8

Statistics for Data Run 118

GENERAL PARAMETERS:

1. DATA RUN 118
2. STAR: ALDEBARAN NO. 168
3. ZENITH ANGLE (ZA) = 29.7°
4. SEC (ZA) = 1.15
5. LOG_e [SEC (ZA)] = .141
6. AZIMUTH = 112°
7. 20 SECOND DATA RECORD: 301-08-46-36 → 56
8. SPATIAL FREQUENCY = 0.047 CYCLES ARC SECOND
9. APERTURE DIAMETER = 6 INCHES

STATISTICAL SUMMARY:

<u>INTENSITY</u>

1. CIV = 0.26
2. $\sigma_{\ell}^2 = 0.018$
3. $\bar{v} = 2.84$ VOLTS
4. LOG_e (CIV) = -1.34
5. $\bar{v}_B = 0.40$ VOLTS

<u>MODULATION INDEX TRACK</u>

1. $\sigma_v / \bar{v} = 0.05$
2. $\bar{v} = 3.9$ VOLTS
3. $\bar{v}_D = 0.47$ VOLTS

<u>IMAGE MOTION TRACK</u>

1. $v = 4.2$ VOLTS
2. $\sigma_m^2 = 0.18$ (ARC SECONDS)^2
3. $\sigma_m = 0.43$ ARC SECONDS

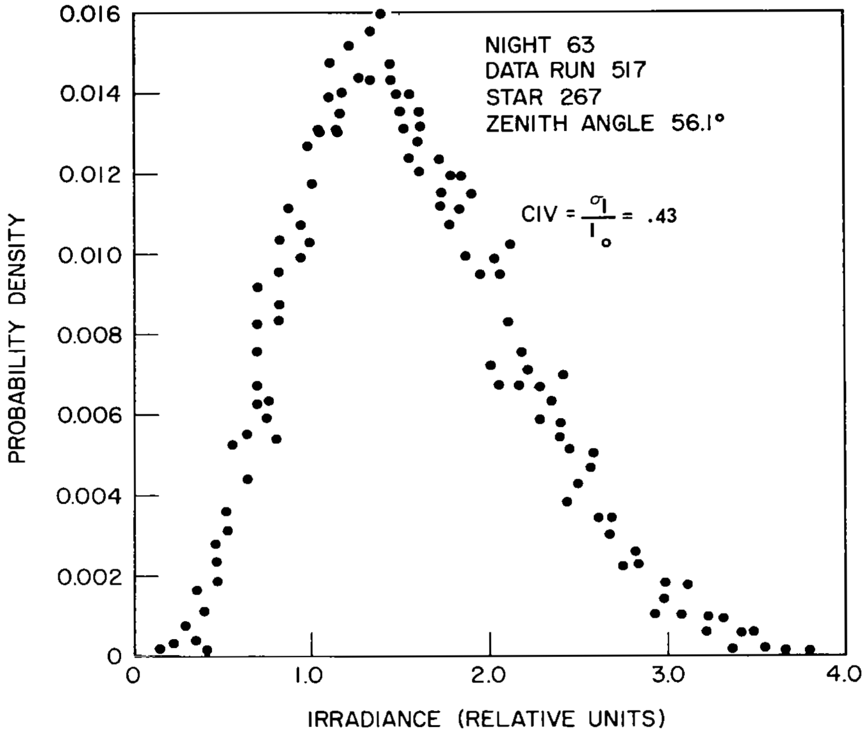

Figure 19. Irradiance probability density function

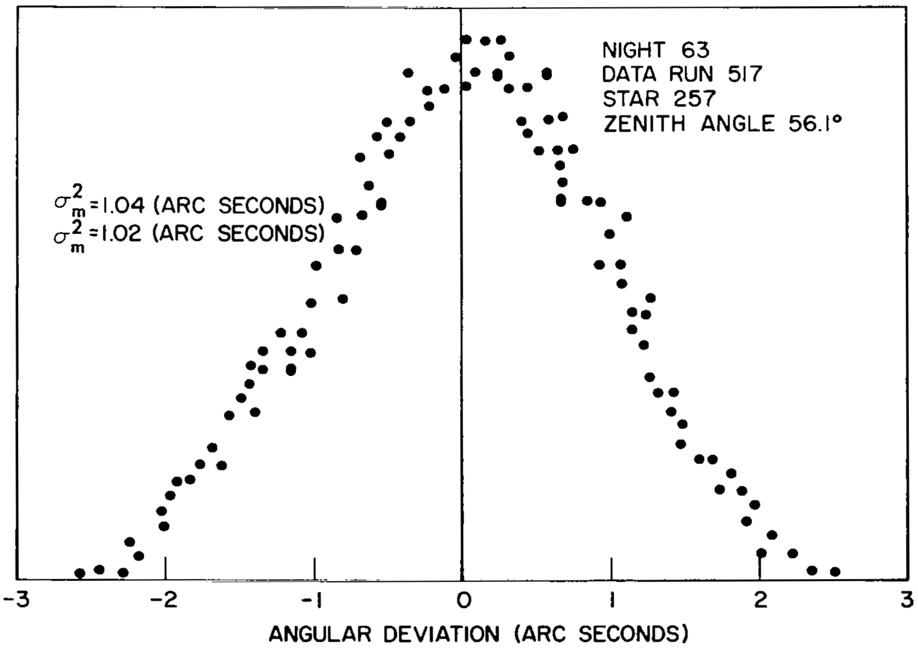

Figure 20. Image motion probability density function

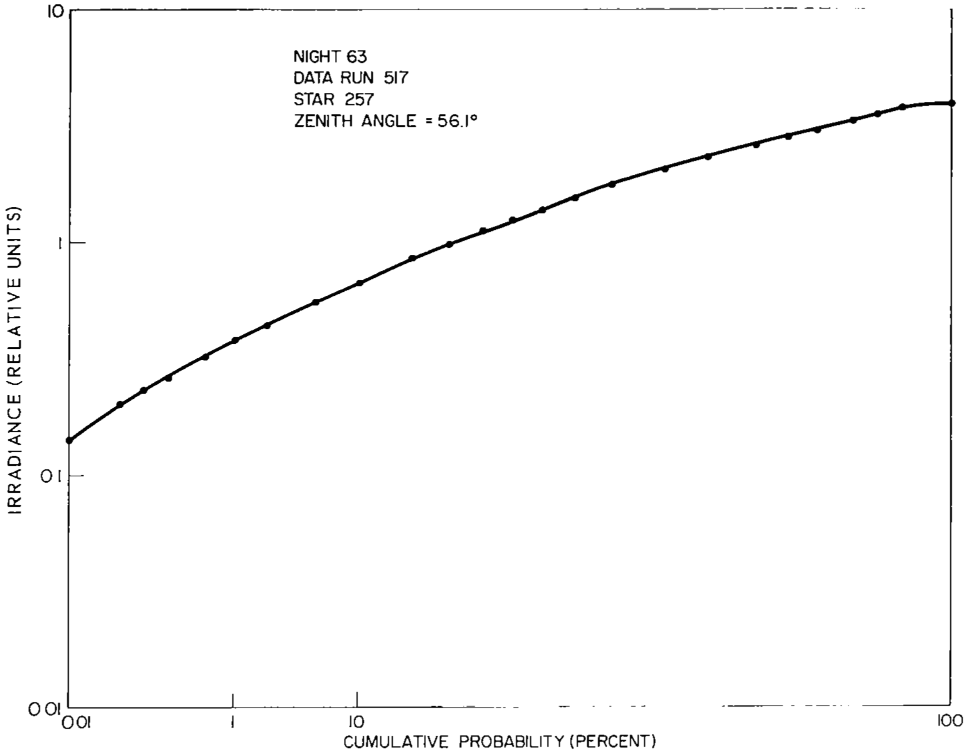

Figure 21. IRRADIANCE cumulative density function

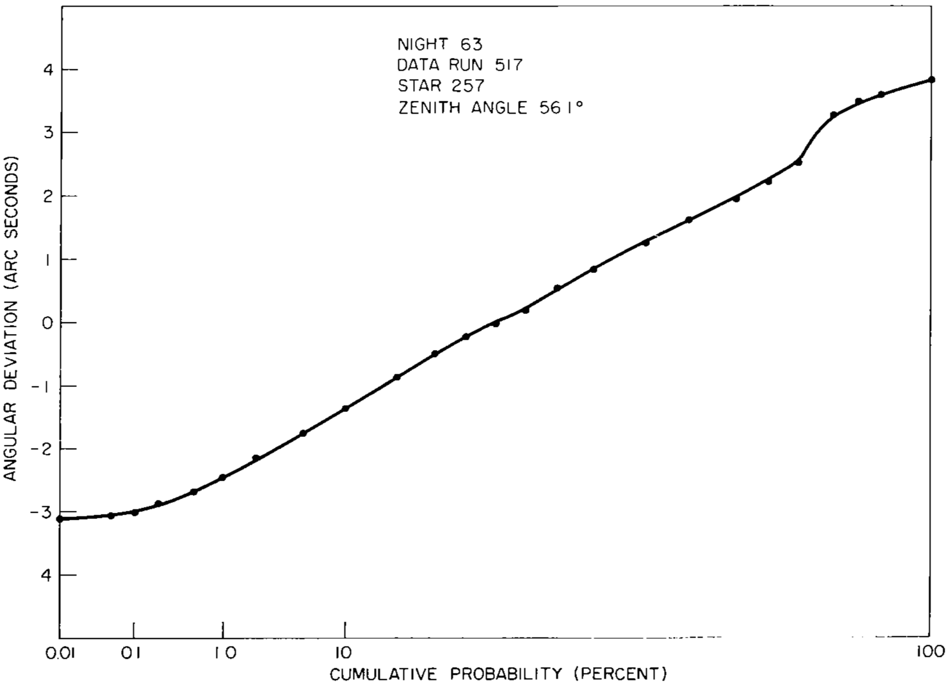

Figure 22. Image motion cumulative density function

A summary of irradiance statistics for all observations on nights 37 and 65 is presented in Figure 23. All data was taken with the full 0.152-meter aperture and is plotted in the form $\log_e$ (CIV) versus $\log_e$ [secant (zenith angle)]. The straight line represents the linear least squares fit to all data points with zenith angles less than 60 degrees. The calculated slopes agree well with the experimental value of $\sec^{1.2}$ (ZA) reported by Protheroe. For larger zenith angles the expected saturation and data scatter effects are evident. Vertical axis intercepts yield the values of CIV for zenith viewing, 20 percent and 14 percent respectively on the two nights. Protheroe reported average values of 14 percent and 16 percent for summer and winter viewing with the same size aperture. In Figure 24 zenith-angle dependence of log-amplitude variance, σ_ℓ^2, is plotted as well for night 65. Zenith angle dependence reflects the proportionality of σ_ℓ^2 to CIV^2. A typical error bar is shown for one point in each graph. The remaining data scatter is likely due to nonstationarity since observations encompassed a period of three or four hours on each night.

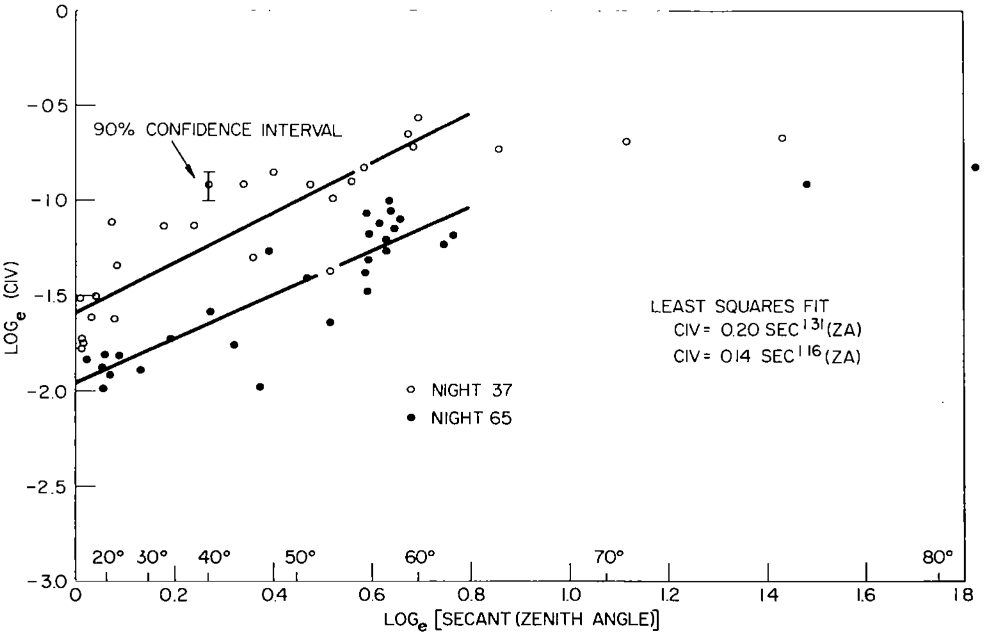

Figure 23. Irradiance statistics

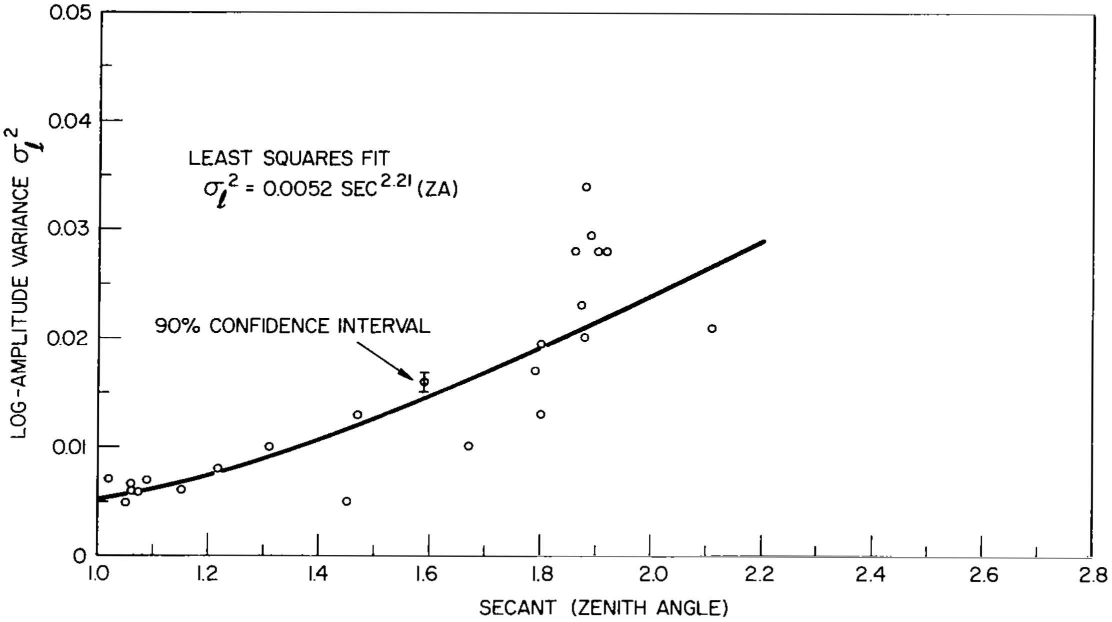

Figure 24. Log-amplitude statistics

Aperture dependence of irradiance statistics is reflected in the three series of observations in Figure 25. A series of five data runs with aperture diameters from 0.0508 meters to 0.152 meters was taken on each of the three successive nights in March. The solid line through each data set represents the best exponential least squares fit of the form

$$\mathrm{CIV}^2 = A \exp(-B \text{ diameter}).$$

The parameters of the fit are A, B, and R, a correlation coefficient representing the accuracy of data fit to the exponential. The parameter B has units of meters^{-1} and can be related to the irradiance correlation distance, $\sqrt{\lambda z}$, by the technique described in Chapter III. The calculated values must be corrected for zenith angle of observation in order to arrive at the desired quantity $\sqrt{\lambda H_0}$,

$$\sqrt{\lambda z} = \sqrt{\lambda H_0 \sec \theta},$$

where

θ = zenith angle

and

H_0 = altitude most significant in determining irradiance fluctuations.

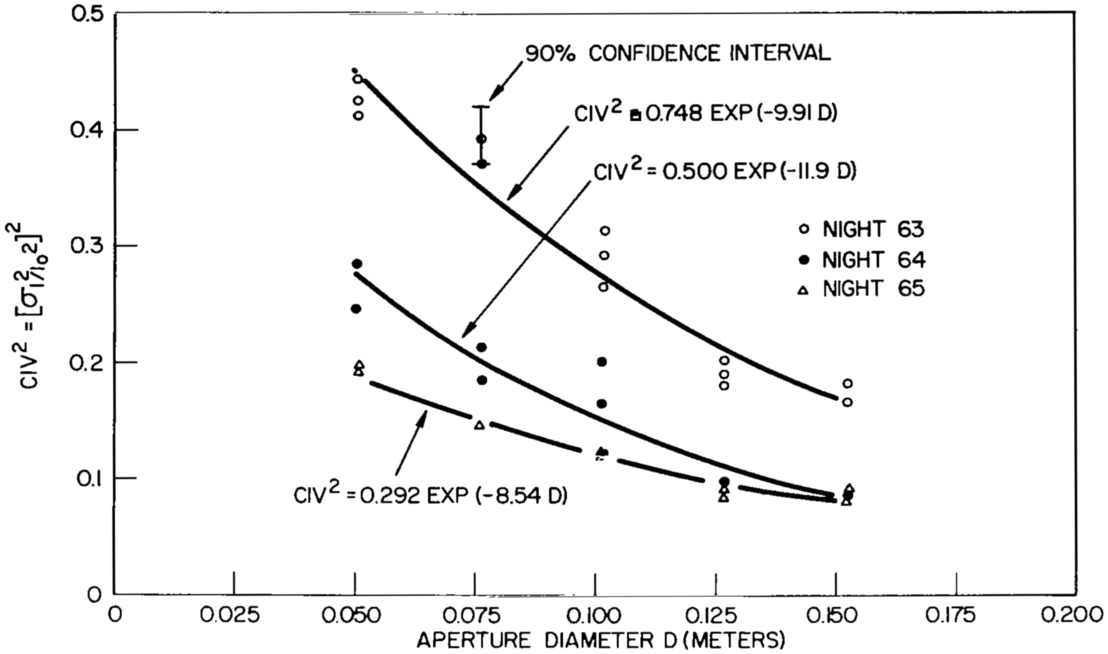

Figure 25. Irradiance aperture dependence

Results are tabulated below for the three series of runs. Height at which maximum wind velocity occurred is given, as is the height for the temperature inversion corresponding to the tropopause. The meteorological parameters were obtained from balloon rawinsonde probes launched from near Dulles International Airport within a few hours of each series of runs. Although the launching site is about 80 kilometers from the point of stellar observations, the upper altitude parameters can be considered fairly typical for the entire Washington, D.C., vicinity.

There is no clear correlation between measured height, H_0, and heights at which meterological evidence for turbulence exists. The statement about correlation distance was that it should be of the order of $\sqrt{\lambda H_0}$, not necessarily equal to it, however. All heights are within a factor of two of each other, indicating that effects located at these higher altitudes are contributing most significantly to irradiance statistics.

Table 9

Irradiance Correlation Distance and Meterological Parameters

Night	Exponential Fit				Meterological Parameters		
	B	$\sqrt{\lambda z}$	$\sqrt{\lambda H_0}$	H_0	height of tropopause (from temperature) data	height of max. wind velocity	max. wind velocity
	(meters^{-1})	(meters)	(meters)	(kilometers)	(kilometers)	(kilometers)	(meters/second)
63	9.91	0.134	0.096	18.4	10.1	9.2	40
64	11.9	0.112	0.083	13.8	10.0	14.5	18
65	8.54	0.156	0.106	22.5	11.6	10.8	66

Frequency domain behavior of irradiance is reflected in Figures 26 and 27 and also in the figures of Chapter V. The latter are of particular interest since they show spectrum shape for near-zenith viewing on several different nights. They will be discussed in connection with a model for strength of turbulence in the latter chapter. It has been shown[43] that frequency spectrum of log-amplitude is nearly identical to that for irradiance under the conditions of small σ_{ℓ}^{2}. For the starlight observations reported here this is certainly the case. Essentially all spectral densities of irradiance have the same type of shape. They tend to increase slowly from zero frequency to a broad peak at about 10 Hz to 20 Hz. Beyond that they obey a near exponential decrease to the system noise level (40 db) at a few hundred Hz. It is reasonable to assume that turbulence elements of size, $\sqrt{\lambda z}$, which are most responsible for the irradiance fluctuations also are responsible for the peak. Without prior knowledge of the proportionality constant relating frequency to $\sqrt{\lambda z}$, the height z cannot be determined here. As zenith angle increases, the peak moves toward the origin and bandwidth of the entire spectrum is reduced, roughly in proportion to $1/\sqrt{\sec \theta}$. As aperture diameter decreases the peak moves to higher frequencies and bandwidth increases. Samples of zenith angle and aperture dependence are shown in Figures 26 and 27 respectively. These spectral densities are normalized to unit variance for ease of comparison.

An exponential of the form

$$CIV^2 = A \exp(-B \text{ freq.})$$

can be fitted to the data beyond the low frequency peak and B^{-1} used as a measure of bandwidth. When this is done the ratio of bandwidths for the different zenith angles of Figure 26 is found to be 1.8. This compares with 2.0 for the ratio of

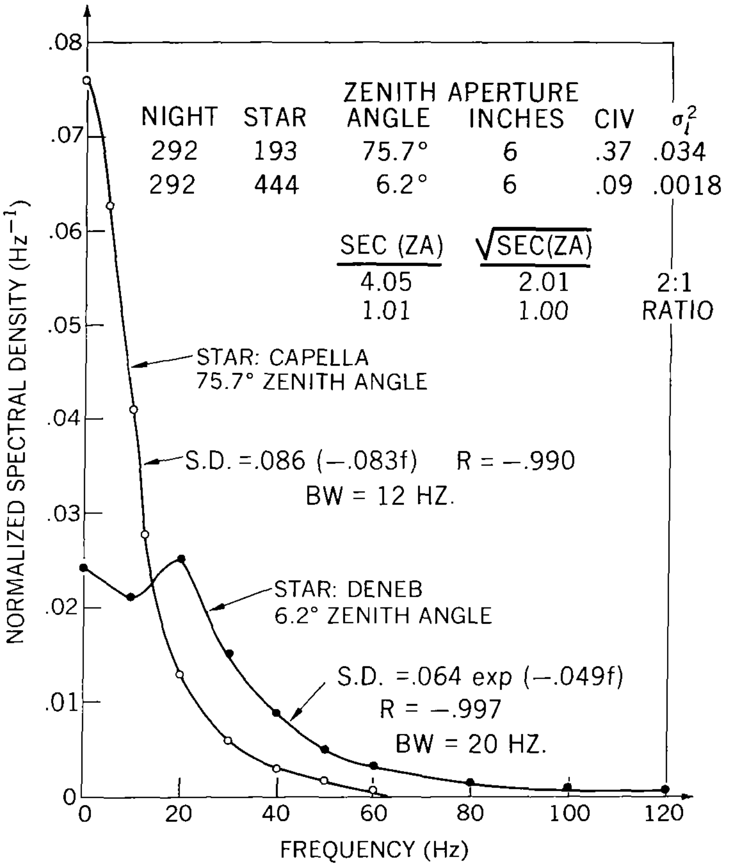

Figure 26. Example of irradiance spectral density zenith angle dependence

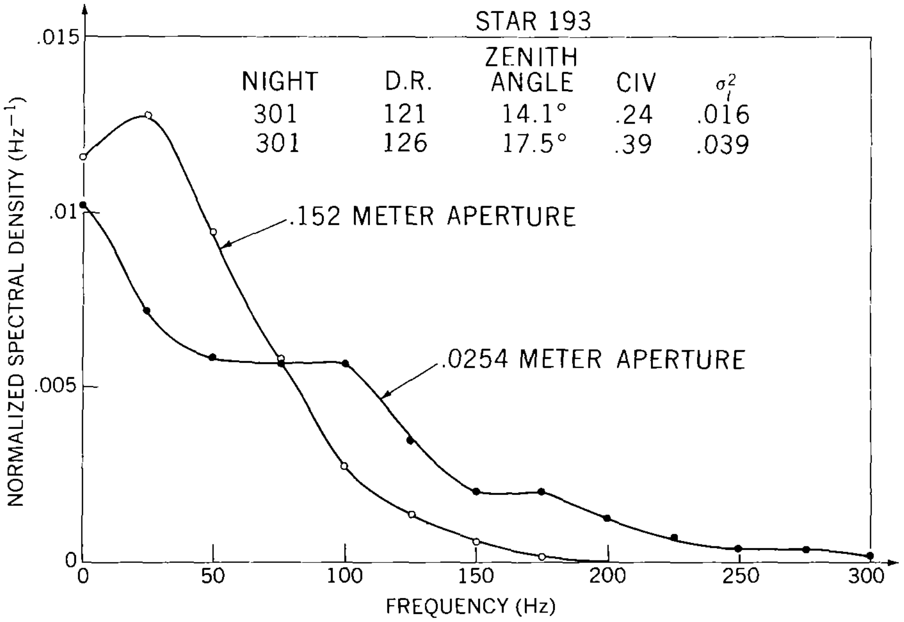

Figure 27. Example of irradiance spectral density aperture dependence

square root secant zenith angle for the two stars. Aperture reduction in bandwidth is about 2:1 in passing from the 0.0245-meter aperture diameter to the full 0.152 meter. No strict power law dependence is expected and this matter will be taken up again in the next chapter. Relationship of bandwidth, B^{-1}, and upper altitude wind velocity is dramatically demonstrated in the following table. Listed here are exponential fit parameter, B^{-1}, and R, correlation coefficient, along with the maximum wind velocity for various nights. All spectral densities were computed for near-zenith observations with the 0.152-meter aperture. This prevented confusion between zenith angle and aperture dependence.

Table 10

Irradiance Bandwidth and Upper Altitude Wind Velocity

Night	Data Run	Zenith Angle	CIV	Exponential Fit Parameters				V_N (max) (meters/second)
				A	B	R	1/-B	
292	61	6	.085	.0135	-.0229	-.930	43.7	21
297	87	7	.112	.0204	-.0187	-.982	53.5	38
301	121	14	.244	.0338	-.0273	-.978	36.6	32
036	424	10	.252	.0102	-.0186	-.931	53.8	54
037	449	7	.220	.0354	-.0263	-.986	38.0	51
063	524	18	.199	.0205	-.0171	-.985	58.5	40
064	547	11	.139	.0317	-.0323	-.991	30.96	18
065	584	18	.135	.0316	-.0149	-.957	67.11	66
077	623	14	.242	.0921	-.0118	-.962	84.5	97
087	633	25	.180	.0257	-.0215	-.978	46.5	38

While irradiance statistics were found to be fairly similar from night to night, image motion and image size statistics changed markedly within even a few hours on a particular night. This was to be expected due to the higher degree of nonstationarity of the lower atmosphere, where these quantities are primarily determined. Increase in statistical errors for the measurement of motion and size also played a large role. Two sets of image motion statistics for night 37 are shown in Figure 28. The first set was taken just after dusk and the second set an hour later. Note the factor-of-two reduction in σ_m^2 for all zenith angles during the later period. Lines drawn through the data represent the best fitting line of the form

$$\sigma_m^2 = M \text{ secant (zenith angle).}$$

Value of the slope m was 1.4 and 0.65 (arc seconds)^2 for the first and second sets of observations respectively. M is the value of σ_m^2 for zenith viewing. For essentially all observations on all nights the range of M was 0.4 to 1.6 (arc seconds)^2. Statistical error bars drawn for a typical point in Figure 28 indicate that nearly all data scatter can be accounted for on this basis alone. Before plotting, each data value of σ_m^2 was corrected for a noise component most probably due to chopper pattern centering error. Fortunately the noise was periodic (8 Hz) and its magnitude could be accurately measured from the spectral density of the voltage output proportional to image motion. Magnitude of the noise was generally such that it contributed 5 to 20 percent of image motion variance. All values of σ_m^2 and spectral densities plotted here have been corrected individually for the noise component.

Data on aperture dependence of image motion was taken simultaneously with the three sets of data on irradiance aperture dependence discussed previously. Each data set was taken over a 15-minute period and consisted of five different aperture diameters evenly spaced from 0.051 to 0.152 meters. As shown in Figure 29 a least squares power curve of the form

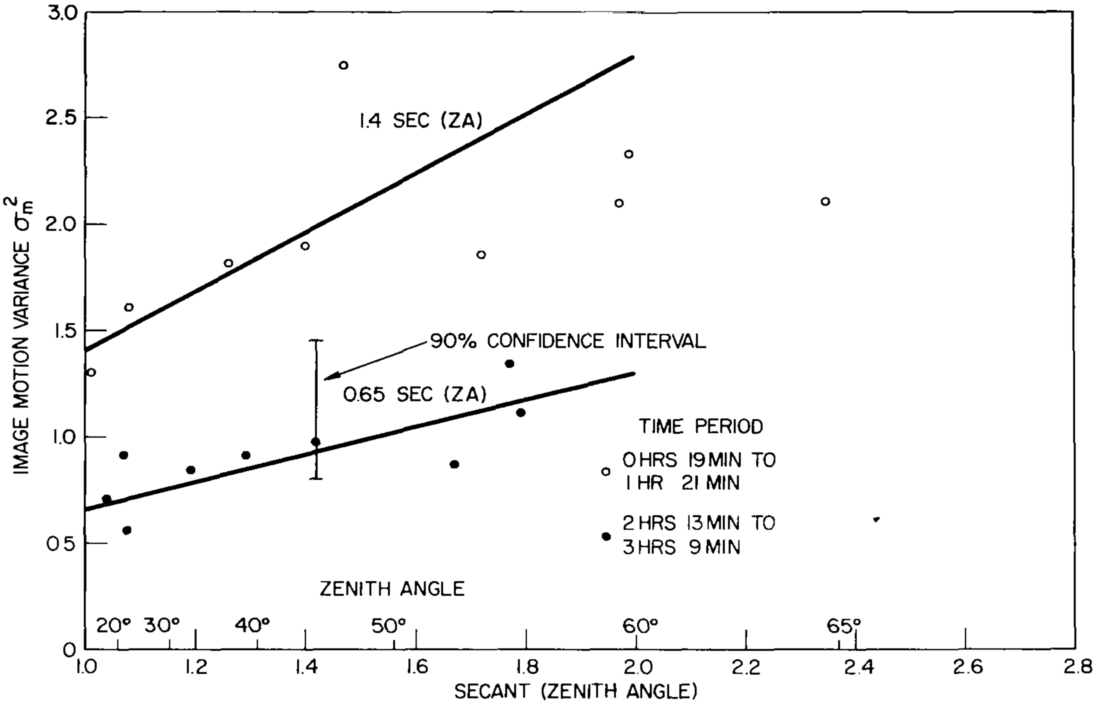

Figure 28. Image motion statistics

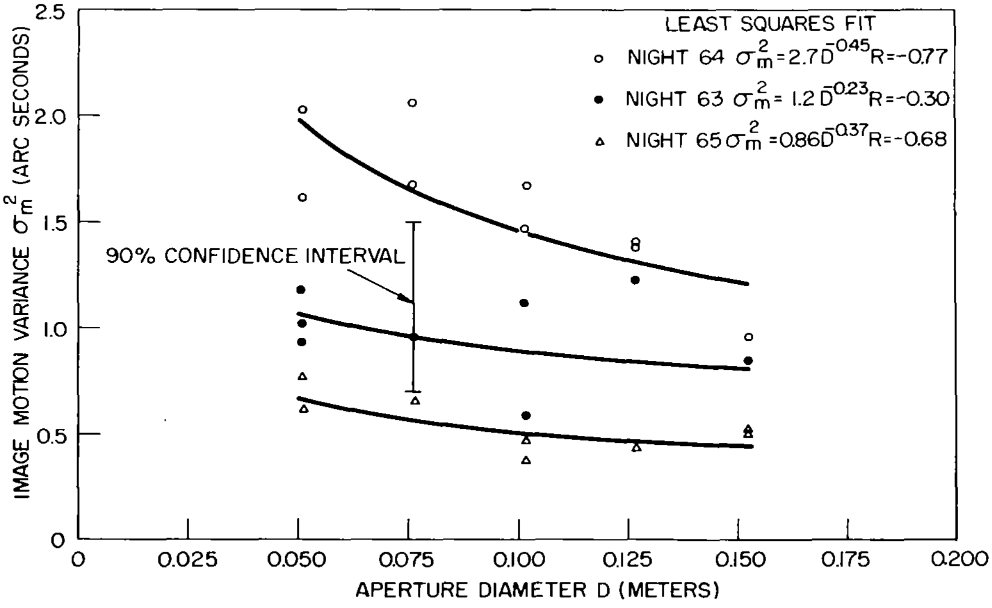

Figure 29. Image motion aperture dependence

$$\sigma_M^2 = A\,(\text{diameter})^B$$

was fit to each data set. The calculated power dependence, B, compares roughly in each set with the theoretical value of -1/3. Correlation coefficient, R, is low, especially for night 63 data, indicating data scatter. Once again, most scatter can be explained by statistical error bars based on the length of each sample and the number of independent samples.

The frequency spectrum of image motion for data taken with a 0.152-meter diameter aperture is characterized by a rapid exponential decrease from zero frequency. Essentially all motion is confined to frequencies below 20 Hz. A typical example is shown in Figure 30 and several more are included in the Figures of Chapter V. A decrease in aperture or zenith angle tends to flatten the spectrum and extend it to somewhat higher frequencies. This data and its relation to strength of turbulence analysis will be examined in greater detail in the next chapter.

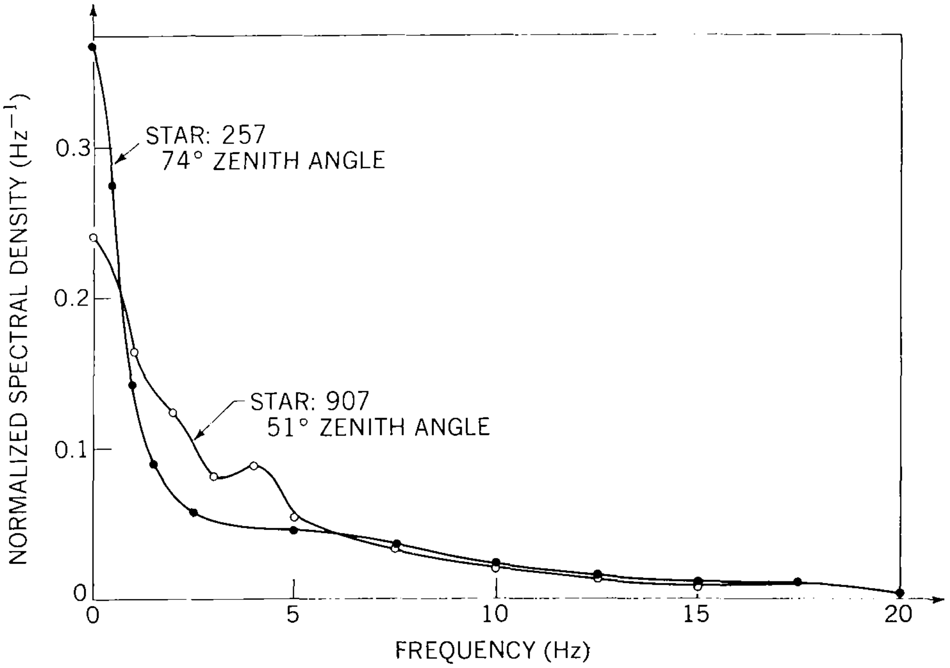

Figure 30. Example of image motion spectral density

Image size information is derived from the measured modulus (MTF) of an optical transfer function. Plotted in Figure 31 are measured MTF values for two sequences of stellar observations on night 65. Each plotted value is determined by the calibration of modulation-index voltage. Observations were taken on each star at five spatial frequencies during a total time period of 15 minutes. A smooth curve was then fitted through the data points and the modulus = 1.0 point at zero spatial frequency. The resultant MTF does not yield information on image fine structure but provides an estimate of the average short-term profile. The profile plotted in Figure 32 is the computer-calculated Fourier transform of the observed MTF for star 193 on night 65, corrected for optical system MTF by division. The calculated profile for star 257 on the same night was not plotted since it fit almost exactly the star-193 result. Observed modulus values for the two stars show a distinct difference (10 to 20 percent) for intermediate spatial frequencies, however. This indicates that a 10 percent error in modulus value would not be reflected in a correspondingly large error in image size. The Airy diffraction pattern for an f/8, 0.152-meter diameter, circular objective in 0.5-micron light is plotted in Figure 32 for comparison. Width of both profiles is measured at the 1/e points. The Airy pattern was generated from the diffraction limited MTF of Figure 17 by the same computer routine used on stellar data. This serves to test the computational approximations used. Note the expected ring structure on the Airy pattern. Ring structure and negative intensities on the stellar profile are caused by truncation of the Fourier Transform at 0.6 cycles per arc second. This is where data on modulus ended. This truncation does not sensibly effect image width, however.

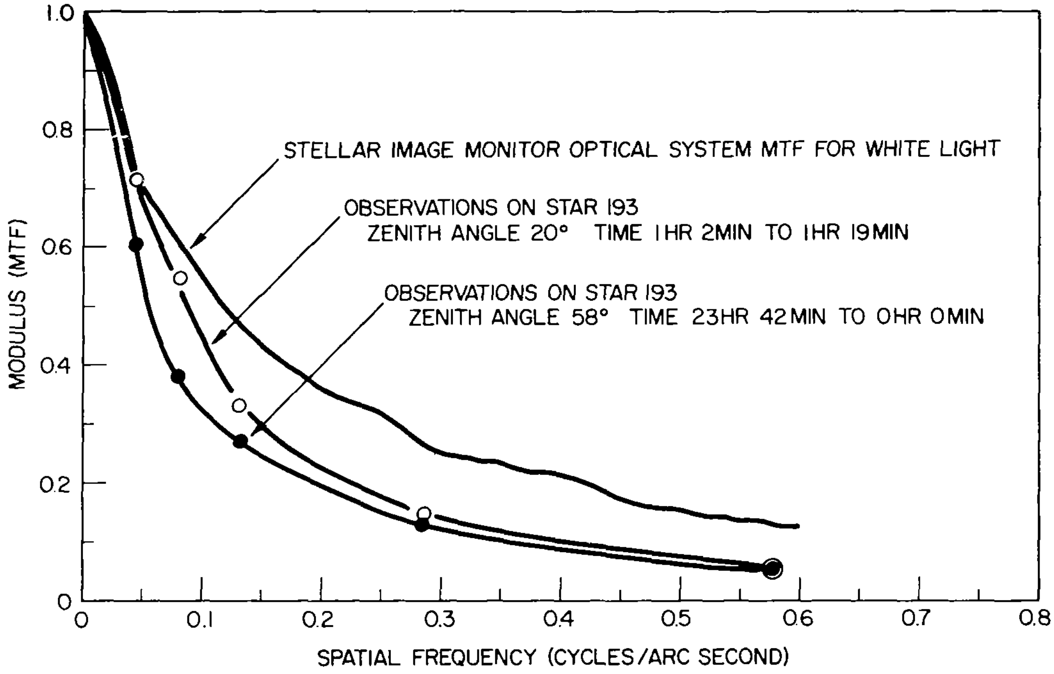

Figure 31. Average short-term transfer functions

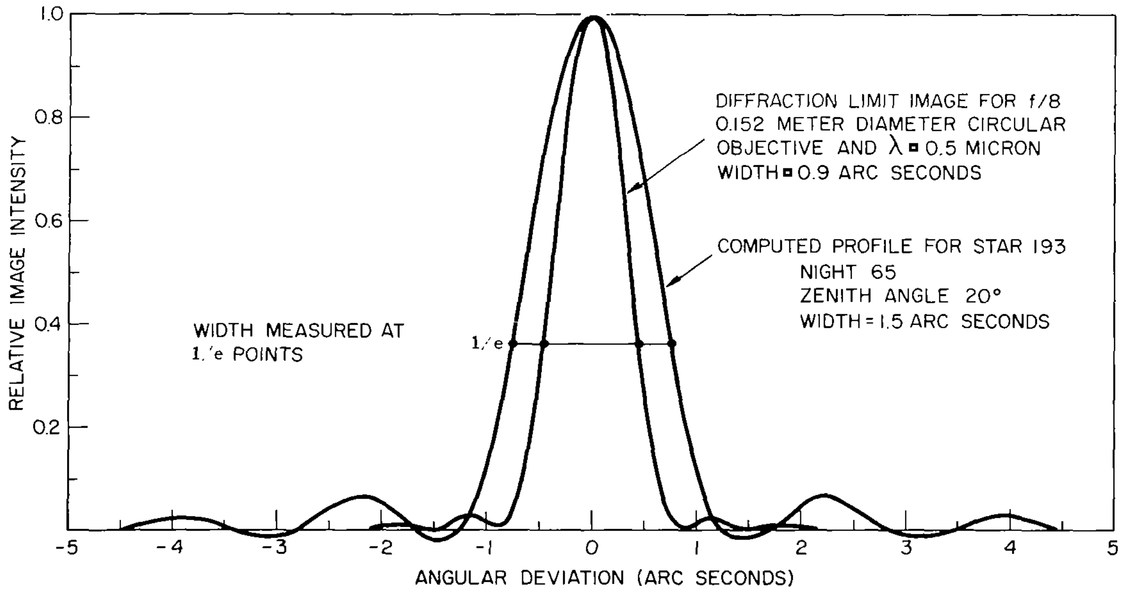

Figure 32. Average short-term image profile

An estimate of long-term profile is obtained as discussed in the previous chapter. For the long term, the key parameter is image motion variance, σ_m^2. Two profiles corresponding to the data sets of star 193 and star 257 from night 65 are plotted in Figure 33. The large difference in profile width reflects the difference in σ_m^2 values for the two stars. Note the disappearance of ring-like structure. This disappearance can be attributed to the smoothing action of the transfer function computed from image motion variance. Variance of image profile, σ_s^2, can here be safely used as a measure of width since there are no false contributions from ring-like structure. Departure of ratio of the two σ_s^2's from the ratio of secant (zenith angle) is expected since σ_m^2 ratio shows this departure. If each profile were strictly Gaussian, its width at the 1/e points would be

$$2\sqrt{2}\,\sigma_s .$$

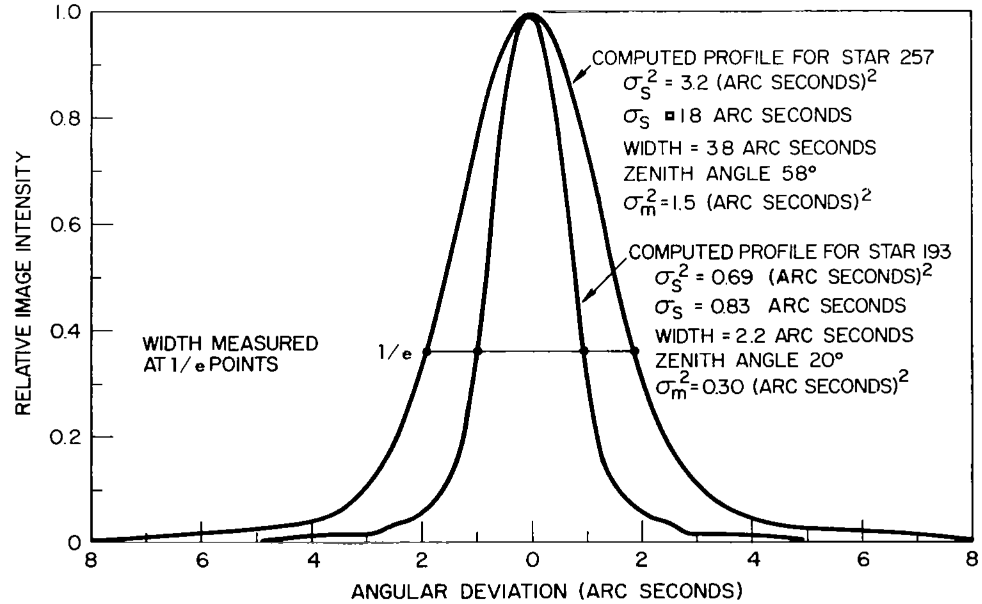

Figure 33. Long-term image profiles

Table 11

Stellar Image Sizes

Night	Star Number	Zenith Angle (degrees)	sec (ZA)	Short-Term Width	Image Motion σ_m^2	Long Term σ_s^2	Long Term σ_s	Long Term Width
63	257	56	1.79	1.6	1.0	2.3	1.5	3.6
	193	20	1.06	1.5	1.2	2.2	1.5	3.5
	257	57	1.84	1.5	0.85	2.3	1.5	3.0
64	257	56	1.79	1.4	1.4	2.9	1.7	3.7
	193	18	1.05	1.4	0.41	1.4	1.2	2.1
65	257	58	1.89	1.5	1.5	3.2	1.8	3.8
	193	20	1.06	1.5	0.30	0.69	0.83	2.2
	257	56	1.79	1.6	0.46	1.3	3.1	3.1
77	257	56	1.79	2.8	2.1	3.6	1.9	4.7
	193	26	1.11	1.4	0.81	2.0	1.4	3.0
87	257	56	1.79	2.8	0.77	2.0	1.4	3.4
	193	26	1.11	1.4	0.43	1.3	1.2	2.0
	257	59	1.94	2.8	0.74	3.6	1.9	3.5

*All variances measured in (arc seconds)^2. Rms and width measured in arc seconds.

This behavior is also roughly confirmed. A summary of all image-size results is given in Table 11. These results reflect the wide variety of conditions present on the various observing nights. Note again the large dependence of the long-term image size on strength of image motion, since the method of obtaining σ_s^2 involves essentially addition of σ_m^2 and the short term σ_s^2.

CHAPTER V

DETERMINATION OF TURBULENT PROFILE

Best Present Estimates of Profile

The common factor for all of the theoretical analysis reported in Chapter III is an integral expression containing $C_N^2(h)$, the refractive index structure constant, as a function of altitude. Lack of both experimental and theoretical knowledge of this profile is the single greatest obstacle to understanding vertical propagation. If the profile were known, optical propagation theory could be tested in any number of interesting experiments. Yet what data there is suggests that no one series of measurements to date has been sufficient to accurately describe the profile. For, as soon as the measurements were taken, the atmosphere changed. This is the old problem of nonstationarity of the turbulent process. Lawrence, Ochs, and Clifford[42] in a series of nighttime measurements with an airborne temperature sensor noted several orders of magnitude fluctuation in $C_N^2(h)$ for essentially the same altitude. All these measurements were taken within four kilometers of ground level and probably reflect the presence of time-varying local disturbances. Turbulence at higher levels should be relatively more stationary. Of course, the average behavior of atmospheric turbulence could be described by a careful series of thermal and optical measurements as a function of altitude. A program to do this would be difficult and costly and would not always generate results when needed. Alternately, if the theoretical dependence on $C_N^2(h)$ is accepted as a working hypothesis, much can be learned from ground-based observations. A useful concept in conjunction with these observations is a turbulent profile model, i.e. a functional dependence for $C_N^2(h)$. Model parameters can then be adjusted for correct prediction of ground-based stellar data. In particular, simultaneous Stellar Image Monitor observations of both irradiance and phase statistics should permit a more accurate determination of model parameters than previous data. Neither direct measurement nor ground-based observations solve the real problem of nonstationarity, but the technique of modeling should make it possible to describe average or at least typical behavior of the turbulent profile.

Any proposed model should reflect probable meteorological factors at the origin of turbulence. As noted previously, essentially all refractive-index variations are accounted for by small-scale temperature fluctuations. These in turn can be related to the pertinent larger scale meteorological parameters. The intent is not to construct an actual profile from meteorological parameters, but merely to show their influence. Equation (13) of Chapter II related $C_N^2(h)$ to $C_T^2(h)$. This can be approximated for visible wavelengths by

$$C_N^2(h) \simeq 10^{-12} \left(\frac{\rho}{\rho_0}\right)^2 C_T^2(h) . \tag{89}$$

In turn, $C_T^2(h)$ can be expressed from turbulence theory[19, 32] in terms of gross meteorological parameters for a particular altitude by

$$C_T^2(h) = A^2 \frac{\epsilon^{2/3} \gamma^2}{\beta^2} , \tag{90}$$

where

ϵ = rate of energy per unit mass dissipated by viscous friction,

γ = average vertical gradient of potential temperature, θ

$= \left\langle \frac{\partial \theta}{\partial h} \right\rangle$,

β = average vertical wind shear,

and

A^2 = empirical constant.

Numerous measurements of ϵ are available for at least the lower altitudes. Typical values, as quoted by Hufnagel[24], show a decrease from 300 $\text{cm}^2/\text{second}^3$

at ground level to 0.07 $cm^2/second^3$ at 10 kilometers and then an abrupt rise, although data is scarce and quite variable in this region. Potential temperature, θ, is defined by

$$\theta \equiv T - \Gamma h,$$

in terms of actual temperature and Γ, the adiabatic lapse rate. For dry air

$$\Gamma = -9.8 \ ^\circ C/\text{kilometer}.$$

The relationship between $\partial T/\partial h$ and Γ is a measure of stability, such that

$$\frac{\partial T}{\partial h} < \Gamma \quad \text{unstable,}$$

$$\frac{\partial T}{\partial h} = 0 \quad \text{neutral,}$$

$$\frac{\partial T}{\partial h} > \Gamma \quad \text{stable,}$$

and

$$\frac{\partial T}{\partial h} > 0 \quad \text{inversion.}$$

Near neutral and unstable conditions favor the development of turbulence. Values of β are the least well known. As Hulett[44] pointed out, small-scale shears between layers a few tens of meters apart tend not to be included in the reported data. Shears of this dimension are probably the most effective in controlling optical effects. The three parameters of equation (90) are height dependent and also a function of one another. Thus it is difficult to isolate a single cause of turbulence. The important information is that the most probable mechanism for turbulence generation, at least in the lower altitudes, is vertical temperature gradient, vertical wind shear, or some combination of the two.

Upper-altitude investigation (above several kilometers) of aircraft size turbulence by Clodman, Morgan, and Ball[45] suggests that wind shear can also combine with a gravity-wave mechanism to yield enhanced turbulence. Gravity waves result from large air mass flow over obstacles such as mountain ranges or even small hills. They are only imperfectly understood at present. It is known that as these waves break down and interact with each other and the main flow of wind itself, severe turbulence may result. These waves tend to propagate to regions of lower density, meaning higher altitudes. During this propagation, gravity wave amplitude tends to build up and at the tropopause quite a strong disturbance could result from interaction with shear-generated turbulence. The tropopause, the region of temperature inversion at approximately the 200-millibar pressure level, has historically been considered a source of turbulence. Whether it acts as a source or permits amplification of existing structure is still unknown. Perhaps the most significant feature of this region is the existance of jet stream flows. Velocities of maximum winds in this flow range from 20 to over 100 meters per second. The jet stream vicinity is a region of strong horizontal and vertical wind shears. This may present the source of turbulence energy input which cascades down to the smaller scale phenomena affecting optical propagation. Observations[45] indicate that the maximum turbulence occurs approximately ±40 millibars from the jet stream core. This roughly corresponds to 1 kilometer below and 2 kilometers above the core. Conditions for turbulence generation at higher altitudes are not very sensitive to diurnal variations, as are conditions in the surface boundary layer. The temperature field is much more stable near the ground at night than during the day and strength of turbulence is often reduced by a factor of 100.

A typical example of vertical profiles of temperature and wind velocity are shown in Figure 46. This is data from a rawinsonde observation for March 6, 1969. The point of observation was, Sterling, Virginia, and time release was 6:15 pm EST. The midpoint of the flight corresponded to the beginning of stellar observations on that particular night. No attempt at smoothing the reported profile was made The temperature profile indicates a small inversion layer at the surface and then an abrupt switch to near by neutral conditions. Stability with little change in the value of temperature gradient is evident in the tropopause at 11.6 kilometers, except for a disturbed temperature layer near 1 kilometer. Above the tropopause the gross temperature profile exhibits fluctuations in the value of temperature gradient. Wind profile maximizes at 10.6 kilometers and a speed of 66 meters per second. This is well-developed jet stream flow and represents almost a linear increase from the surface winds of two meters per second. Above the tropopause wind velocity oscillates in magnitude indicating the presence of strong vertical wind shear. Wind direction remains fairly constant for all levels. Data points above the tropopause are separated by a kilometer or more and thus reveal little about fine structure. Smaller scale wind shears and temperature gradients are most probably associated with these regions of large-scale shears and gradients, however.

There are several important points to be derived from the meteorological theory and data.

(1) Little meteorological evidence exists for a thin, highly turbulent layer responsible for all the observed optical effects.

(2) Mechanisms do exist at nearly all levels of the atmosphere for the development of turbulence. The combined factors of wind shear, potential temperature gradient, and gravity waves are the most likely sources.

(3) A turbulence boundary layer exists near the earth's surface in the first tens to hundreds of meters.

(4) Intermediate altitudes (below the tropopause) are thermally stable in general (especially at night) and less turbulence is expected.

(5) The region of the tropopause and beyond is characterized by conditions of possible instability and a high velocity jet stream flow. Turbulence is expected to increase in this region, yet not surpass the maximum near-ground values.

Solutions for Model Parameters

It is desirable to have a functional dependence on altitude for strength of turbulence, $C_N^2(h)$, in order to facilitate comparison of data with theory. At the outset it should be realized that no model could possibly account for the fine structure and all the disturbed layers that are thought to exist. The model should, however, take into account the gross meteorological factors mentioned above and conform to the average or at least typical behavior of the atmosphere. As a first approach, consider a model that uses an exponential decrease with altitude to describe the envelope of $C_N^2(h)$ fluctuations. Refractive-index varies linearly with density which in turn is proportional to exp (- h/7) for a standard atmosphere. $C_N^2(h)$ goes as density squared, thus could be modeled by

$$C_N^2(h) = C_{N_0}^2 \exp(-h/3.5) , \tag{91}$$

where

and $C_{N_0}^2$ = ground strength of turbulence

h = altitude in kilometers .

The hypothesis is that turbulence due to essentially the same mechanism as that near the ground would be damped out from lack of material at higher altitudes. This certainly does not represent the full behavior of $C_N^2(h)$ and appears[44] to overestimate the contribution from intermediate levels below the tropopause. A more accurate model in the sense of agreement with data can be constructed from the curve supplied by Hufnagel, as shown in Figure 34. His values for a clear evening arise from meteorological relations and stellar observations. The curve is characterized by an exponential type decrease in the lower atmosphere, a gradual leveling off, and a sharp spike at the tropopause. A mathematical approximation to this curve can be written

$$C_N^2(h) = A \frac{\exp(-h/H_0)}{h^{\alpha}} + B\,\delta(h - H_1) , \tag{92}$$

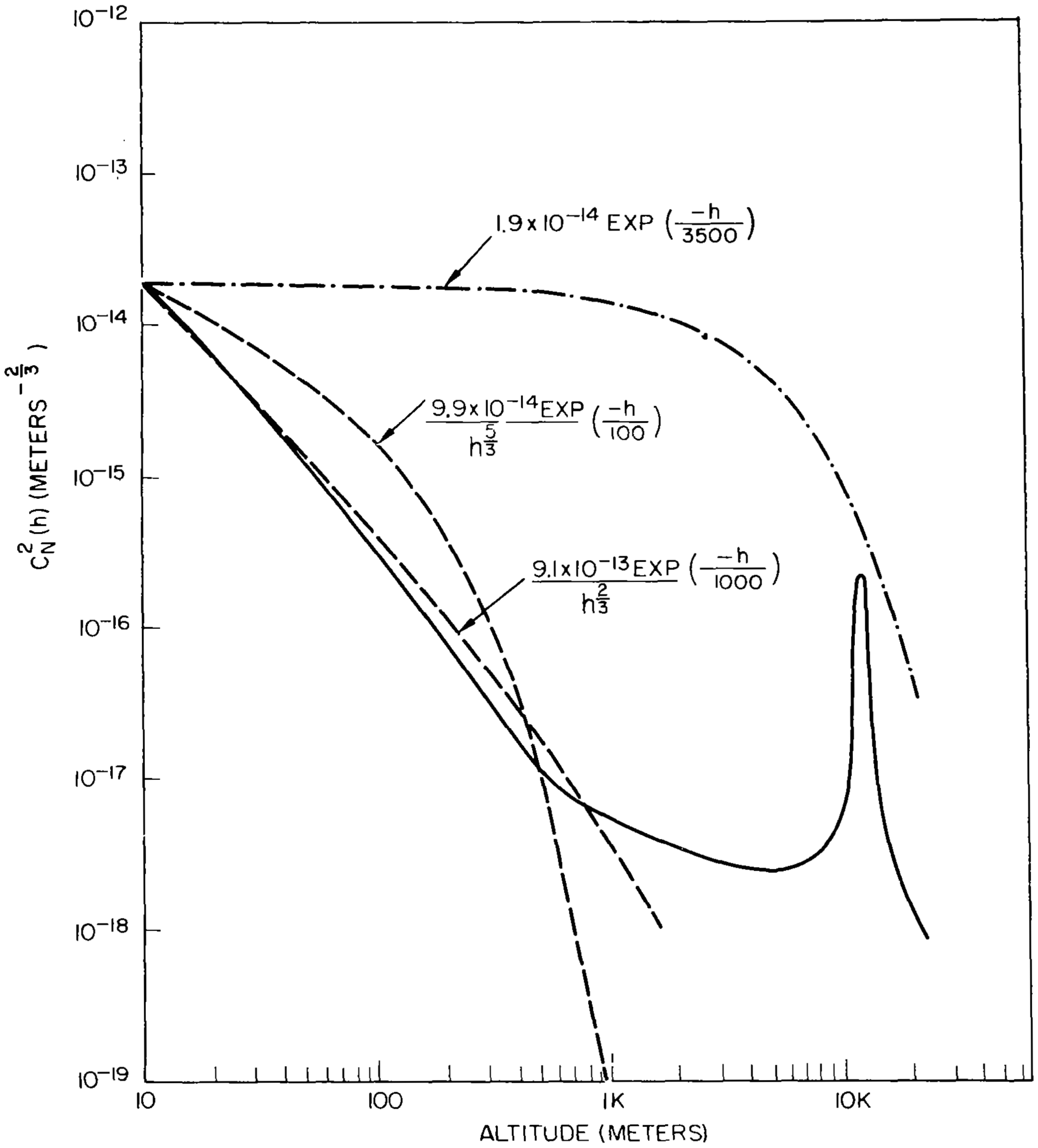

Figure 34. Hufnagel's turbulent profile

where

$A = 9.1 \times 10^{-13}$ meters$^{-2/3}$,

$H_0 = 1$ kilometer ,

$B = 2 \times 10^{-16}$meters$^{-2/3}$,

$H_1 = 12$ kilometers ,

and

$\alpha = 5/3$.

The model of high turbulence at the tropopause represented here by the delta function, was included by Hufnagel to explain stellar irradiance fluctuations. The value of H_0 and the power of altitude in the denominator indicate a more rapid roll-off than the atmospheric density exponential. The density exponential is plotted in Figure 34 for comparison. Hufnagel also presents daytime data which more closely corresponds to the exponential density decrease. There are some scattered data points in the literature that could be added to Figure 34 for comparison. However, these results were most often obtained by inaccurate means and invariably were daytime results. To the author's knowledge one set of useful nighttime results does exsist, at least for the lower atmosphere. This is the set of high-speed temperature measurements made from an aircraft and reported by Lawrence, Ochs, and Clifford[42]. These results seem fairly dependable since system noise level was less than 10^{-18} meters$^{-2/3}$. The average of their measurements agrees well with the Hufnagel model although individual $C_N^2(h)$ values fluctuate orders of magnitude around this average. The net result of the Hufnagel model is a division of $C_N^2(h)$ profile into low-altitude and high-altitude structure and an estimate of the relative contribution of each altitude regime. Hufnagel's quoted result for the integral over the whole profile is 4.3×10^{-13} in units of meters$^{+1/3}$.

The relationship between the two regions of the Hufnagel model and a check on self consistency of the theory can be made by inserting the model into equations developed in Chapter III. All the theoretical expressions for optical statistics depend on an integral over $C_N^2(h)$, the refractive-index structure constant. The form of the integral varies with the statistic being considered. In the case of log-amplitude or irradiance, the integral

$$\int_0^\infty C_N^2(h)\, h^{5/6}\, dh$$

is present and indicates a non-uniform weighting of $C_N^2(h)$ values. The largest contributions to the integral are at higher altitudes where the product $C_N^2(h)\, h^{5/6}$ takes on its largest values. Image motion, modulation transfer function, and image size statistics contain the integral

$$\int_0^\infty C_N^2(h)\, dh,$$

which, of course, takes on its largest values where $C_N^2(h)$ is the largest, presumably near the ground.

Assuming a model of the form fitted to the Hufnagel profile, an estimate of the parameters of this model can be obtained from the theoretical expressions for log-amplitude and image motion. Of these parameters the ground strength of turbulence is the best substantiated at approximately 5×10^{-14} meters$^{-2/3}$.

Even this value can exhibit a large variation with locality and time of measurement. It is generally agreed from various optical and thermal measurements that this value is accurate ± one order of magnitude near the ground at night. The height of the tropopause can also be determined with some assurance from meteorological measurements on a given night. The range is approximately 9 to 14 kilometers. The two remaining parameters, H_0 and B, can be arrived at through the following process. First the analytical expression[92] is inserted in the equations for log-amplitude variance and image motion variance and the integrals are solved. Then the measured values of σ_{ℓ}^2 and σ_m^2 and the assumed values for A and H_1 are inserted. The result is two equations in the two unknowns, H_0 and B, which can be readily solved. Thus a model of the turbulent profile can be constructed for a particular time on a particular night. This model can be checked for self consistency by insertion into the equation for image size. For ease of mathematical treatment the power of the denominator in equation (92) is changed to 2/3. This affects the fit of the model to Hufnagel's curve but still gives order of magnitude results. The integrals are now readily evaluated in terms of gamma functions, as follows:

$$\sigma_m^2 = \kappa_1 \int_0^\infty C_N^2 (h) \, d h , \tag{93}$$

where

$$\kappa_1 = .56 \, D^{-1/3} \, \text{SEC} \, (Z A),$$

and

$$\sigma_{\ell}^2 = \kappa_2 \int_0^\infty C_N^2 (h) \, h^{5/6} \, d h, \tag{94}$$

where

$$\kappa_2 \simeq .09 \, k^{7/6} \, \text{SEC}^{2.4} \, (Z A).$$

Then,

$$\sigma_m^2 = \kappa_1 \int_0^\infty A \frac{\exp(-h/H_0)}{h^{2/3}} \, d h + \kappa_1 \int_0^\infty B \, \delta (h - H_1) \, d h$$

$$= \kappa_1 A H_0^{1/3} \int_0^\infty \exp(-z) \, z^{-2/3} \, d z + \kappa_1 B$$

$$= \kappa_1 \, [A H_0^{-1/3} \, \Gamma (1/3) + B],$$

and

$$\sigma_{\ell}^2 = \kappa_2 \int_0^\infty A \frac{\exp(-h/H_0)}{h^{2/3}} \, h^{5/6} \, d h + \kappa_2 \int_0^\infty B \, \delta (h - H_1) \, h^{5/6} \, d h$$

$$= \kappa_2 A H_0^{7/6} \int_0^\infty \exp(-z)\, z^{1/6}\, dz + \kappa_2 B H_1^{5/6}$$

$$= \kappa_2 \left[A H_0^{7/6}\, \Gamma(7/6) + B H_1^{5/6}\right],$$

where

$$\int_0^\infty \exp(-z)\, z^{\phi-1}\, dz = \Gamma(\phi). \tag{95}$$

As a typical example, consider data run 584 from night 65, for which

diameter, $D = .152$ meters,

$\mathrm{SEC}(ZA) = 1.06$,

$\lambda = .5 \times 10^{-6}$ meters,

$H_1 = 11.6$ kilometers,

and $A = 4 \times 10^{-14}$ meters$^{-2/3}$.

Noting that $\Gamma(7/6) = 0.923$ and $\Gamma(1/3) = 2.68$, the two equations can be solved to obtain

$H_0 = 112$ meters

and $B = 6.7 \times 10^{-16}$ meters$^{-2/3}$.

Equation (76) for image size under the assumption of a Gaussian beam profile is also expressible in terms of these parameters, as follows:

$$\sigma_S^2 = \kappa_3 \int_0^\infty C_N^2(h)\, dh, \tag{96}$$

where

$\kappa_3 = .98\, \lambda^{-1/3}\, \mathrm{SEC}(ZA)$, and

$$\sigma_s^2 = \kappa_3 \int_0^\infty A \frac{\exp(-h/H_0)}{h^{2/3}} + \kappa_3 \int_0^\infty B\, \delta(h - H_1)\, dh$$

$$= \kappa_3 \left[A H_0^{1/3}\, \Gamma(1/3) + B\right].$$

Inserting the above calculated values for H_0 and B yields

$$\sigma_s^2 = 2.9 \text{ (arc seconds)}^2 .$$

This compares with the value of $\sigma_s^2 = 1.1$ (arc seconds)^2 computed from long-term MTF obtained nearly simultaneously with σ_m^2 and σ_ℓ^2. The values of H_0 and B also compare roughly with the Hufnagel fit values of one kilometer and 2×10^{-16} meters$^{-2/3}$. Estimates of $C_N^2(h)$ profile obtained in this fashion are, of course, restricted by the applicability of the model.

Spectral densities of irradiance and image motion provide a more sensitive technique to arrive at an estimate of specific shape of $C_N^2(h)$ profile. As noted in Chapter III both spectral densities are expressible in terms of an integral of the form

$$\int_0^\infty C_N^2(h)\, \mathfrak{J}\{V_N(h), h, D, \theta, f\}\, dh, \tag{97}$$

where $\mathfrak{J}\{\cdot\}$ is a nonlinear function dependent on some or all of the following parameters:

(1) Altitude, h.

(2) Wind velocity profile, $V_N(h)$.

(3) Telescope aperture diameter, D.

(4) Stellar zenith angle, θ.

(5) Temporal frequency under consideration, f.

The $\mathfrak{J}\{\cdot\}$ function in both irradiance and image motion statistics is a fairly complicated integral expression. Peskoff[46] and Fried[47] have solved a simpler version (no frequency dependence) of the irradiance equation. The result in the form of a hypergeometric function is useful only when expressed in a power series approximation and is restricted to the point detector case. Another approach as used in this thesis is numerical integration. The $\mathfrak{J}\{\cdot\}$ equation in each case for a finite aperture and explicit dependence on wind velocity becomes a tabulated function. Reasonably accurate values of wind velocity are available from the Weather Bureau and numerical integration is done by digital computer. The result is a linear integral equation connecting the measured values of σ_m^2 or CIV^2 to the unknown profile, $C_N^2(h)$. If the integrations are replaced by a summation over a number of finite h values, the result is a set of linear simultaneous equations in the unknown $C_N^2(h)$ values. In principle this set could be solved for the desired unknowns by standard mathematical techniques. This approach was tried and very anomalous oscillating solutions were obtained. Apparently there is a problem with data signal-to-noise ratio and, to a lesser extent, with uniqueness of solution. In any event, considering the error bars on spectral density estimates and the wind velocity profiles, it seemed more appropriate to limit the number of degrees of freedom and achieve a rougher estimate of the profile. This was done by using a model for $C_N^2(h)$ based on the Hufnagel curve but containing six unknown parameters

$$C_N^2(h) = A\,\frac{\exp(-h/H_0)}{h^{\alpha}} + B\exp\left[-\frac{(h-H_1)^2}{2\beta^2}\right]. \tag{98}$$

The first term is the familiar combination of exponential roll-off and power of altitude in the denominator. This controls the low-altitude dependence. The second term is inserted to account for the presence of upper altitude disturbances. It is a Gaussian shape with magnitude, B, rms size, β, and centered at height, H_1. The Gaussian shape was chosen arbitrarily as a convenient way of varying the magnitude, size, and position of the representation of upper altitude effects. Another curve or distribution might work just as well and may even be a truer representation of the physical process. In the absence of prior knowledge of the actual physical process, one can well use the Gaussian curve.

Presentation of Data and Construction of Several Profiles

Realizing that image motion effects are due primarily to the strong turbulence of the earth's boundary layer, the parameters, A, H_0, and α were determined through image motion spectral density data. The three parameters were allowed to take on discrete values and a test spectral density was constructed by numerical integration of equation (62). Numerical integration consisted of summing contributions to spectral density from discrete altitude intervals. Each test spectral density was evaluated at a number of discrete frequency values and subtracted from the corresponding data value at that frequency. Absolute value of this difference was used as the measure of accuracy of fit to the data. For image motion, altitude intervals of 10 meters were used in the first 100 meters and then intervals of 100 meters were used to an altitude of one kilometer. The interval range was then broadened to 500 meters and the maximum altitude examined was 9.5 kilometers. Contributions to spectral density were examined every 0.5 Hz from zero frequency to 15 Hz. A test spectral density was computed for the $C_N^2(h)$ profile resulting for every possible combination of the three parameters. In a typical case each parameter was allowed to take on 10 different values. This meant that the results of 1000 combinations were tested. Both the numerical integrations and testing were conducted on a digital computer. The computer was programmed to select the best fit to spectral density data, print it out and also print out the $C_N^2(h)$ profile corresponding to this best fit. Also printed out were the sum of absolute differences for all frequencies for each test case. This enabled an assessment of fit sensitivity to parameter changes. Irradiance spectral density data was used in the same fitting routine to determine the Gaussian shape parameters B, H_1, and β. Since irradiance data was expected to be somewhat more influenced by lower altitude effects than was image motion data by higher altitude effects, the image motion fitting was done first and the best fit parameters used in equation (98) for the full $C_N^2(h)$ profile. Then the irradiance fit was performed to find the remaining three parameters. Altitude intervals for the irradiance data were taken at 100 meters for the first kilometer and then increased to one kilometer up to a maximum altitude of 25 kilometers. This represented the sensible limits of the atmosphere although the formal integration extends from zero to infinity. Contributions to spectral density were examined every 10 Hz from 10 Hz to 250 Hz. At the upper end of the frequency scale irradiance spectral density was usually down at least a factor of 100 from the 10 Hz value.

At first each parameter value was allowed to vary over a wide range. The ranges were than narrowed as it became obvious which values gave the best fits. It was found that a pure exponential decrease, while giving a close fit to image motion data, could not explain the shape of irradiance data. The image motion data required an exponential roll-off typically less than one kilometer while irradiance data favored roll-offs of tens of kilometers without yielding a good shape for even these high values. The implication was clear. Significant contributions to $C_N^2(h)$ were needed at higher altitudes to correctly predict irradiance spectral density. With further analysis it was found that the Gaussian "bump" fit the data quite well. Data and the corresponding fits for six different nights are presented and discussed below. These nights represent a variety of wind conditions and presumably different distributions of turbulence.

The use of the sum of absolute differences between test and data spectral densities was justified on the basis of the desire to obtain a best fit to the shape of the curve. Absolute difference was sensitive to the lower frequencies where spectral density was the largest. This was somewhat desirable since here the signal-to-noise ratio of data was greatest. Statistical error bars were determined in Chapter IV. For irradiance these were ±5 percent and for image motion, ±50 percent. These of course apply to total variance, the integral over the entire spectral density. A relative idea of error distribution with frequency can be obtained by comparison of two consecutive data records, as in Figures 39 and 40. The irradiance spectra exhibit differences of about 10 percent near 10 Hz. Although at frequencies near 200 Hz the relative difference is as high as 100 percent in places, the general shapes of the two curves match well. The two records of image motion show large differences (a factor of four) at the origin, but beyond one Hz, have nearly the same values as well as shape. Discussion of this low-frequency variability in terms of atmospheric, instrumental, and resolution effects is included in Appendix B. A mean square difference statistic was also considered but rejected for its heavy weighting of the lower frequencies. Since a lot of shape information for both types of data is contained in the higher frequency roll-off, it was felt that absolute difference was a reasonable compromise between equal weighting at all frequencies and the mean square approach.

Wind velocity information obtained from weather bureau rawinsonde flights was supplied in terms of speed and direction for a given altitude above the surface. The reported speed was that component parallel to the earth's surface. For spectral density analysis using Taylor's hypothesis, the required speed component is that perpendicular to the optical line of sight, V_N. For horizontal winds of speed V_0 there will obviously be a reduction in V_N for stellar observations at appreciable zenith angles. As Young[18] has pointed out there is also a possible increase in V_N dependent on relationship of wind direction to azimuth of the stellar observation, by the expression

$$V_N = \frac{V_0}{\mathrm{SEC}\,(Z\,A)} \left[1 + \mathrm{TAN}^2\,(Z\,A)\;\mathrm{SIN}^2\,(A\,Z - \theta_0)\right]^{1/2}, \qquad (99)$$

where

V_N = wind component perpendicular to line of sight,

V_0 = horizontal wind speed,

$Z\,A$ = stellar zenith angle,

$A\,Z$ = stellar azimuth angle,

and

θ_0 = direction from which wind is blowing.

Division by secant (ZA) would be the correction factor if only zenith angle effects were considered. The term in brackets represents the interaction of zenith angle, azimuth angle, and natural wind direction. This term is maximum when $(AZ - \theta_0) = 90°$. For this case and a zenith angle of 60° the azimuth correction essentially cancels the zenith angle correction. To eliminate these effects from the spectral density analysis only observations taken within a few degrees of zenith were used. For this situation, $V_N = V_0$ within a few percent regardless of wind direction. Speed, V_0, was itself determined to this same order of accuracy. Although the point of rawinsonde release was some 80 kilometers from the point of stellar observations, the release time and prevailing winds were such that the balloon was essentially overhead for most of the stellar observations. In addition, the upper altitude winds showed little change over a few hours or within a few hundred kilometers of the measurement site. Rawinsonde data for March 6, 1969, taken at stations as diverse as Wallops Island, Virginia; Richmond, Virginia; and Philadelphia, Pennsylvania, and for time separations of up to 6 hours showed correlation within 20 percent with V_0 values obtained at the regular Sterling, Virginia, station. Below 1 kilometer altitude, correlation began to worsen indicating the presence of local terrain effects. Below 150 meters rawinsonde wind velocity was not available. Unfortunately this is the region most effective in determining image motion spectral density. A reasonable approximation to actual wind profile was obtained by linear interpolation from a recorded or estimated surface wind value to the first rawinsonde value at 150 meters. All surface wind values at the point of observation were less than three meters per second, for beyond this value telescope vibration became a serious contribution to image motion and data was not taken.

The six nights for which turbulent profile models were constructed are listed in Table 12 along with the particular data run parameters used on each night. Image motion and irradiance spectral densities from these data runs are plotted in Figures 35 through 41. Ordinate values are σ_m^2/Hz and CIV ^{2}/Hz respectively. Thus the strength of turbulence induced fluctuations at a particular frequency can be compared from one night to the next. Corresponding wind velocity profiles for each night appear in Figures 42 through 47. Note the significant range of maximum wind speeds represented here. The continuous solid line on the spectral density plots is a smooth curve representation of the best computer generated fit to the data points. Turbulence profiles which resulted in these best fits are shown in Figures 48 through 53.

Computer generated fits to image motion spectral density followed the average behavior of the data. In particular the sharp increase below one Hz was well approximated. A disturbing feature of the fit, however, was the one to two Hz oscillation observed in all curves. Oscillation resulted from a truncation of the Fourier transform from the computed autocorrelation function. The maximum lag

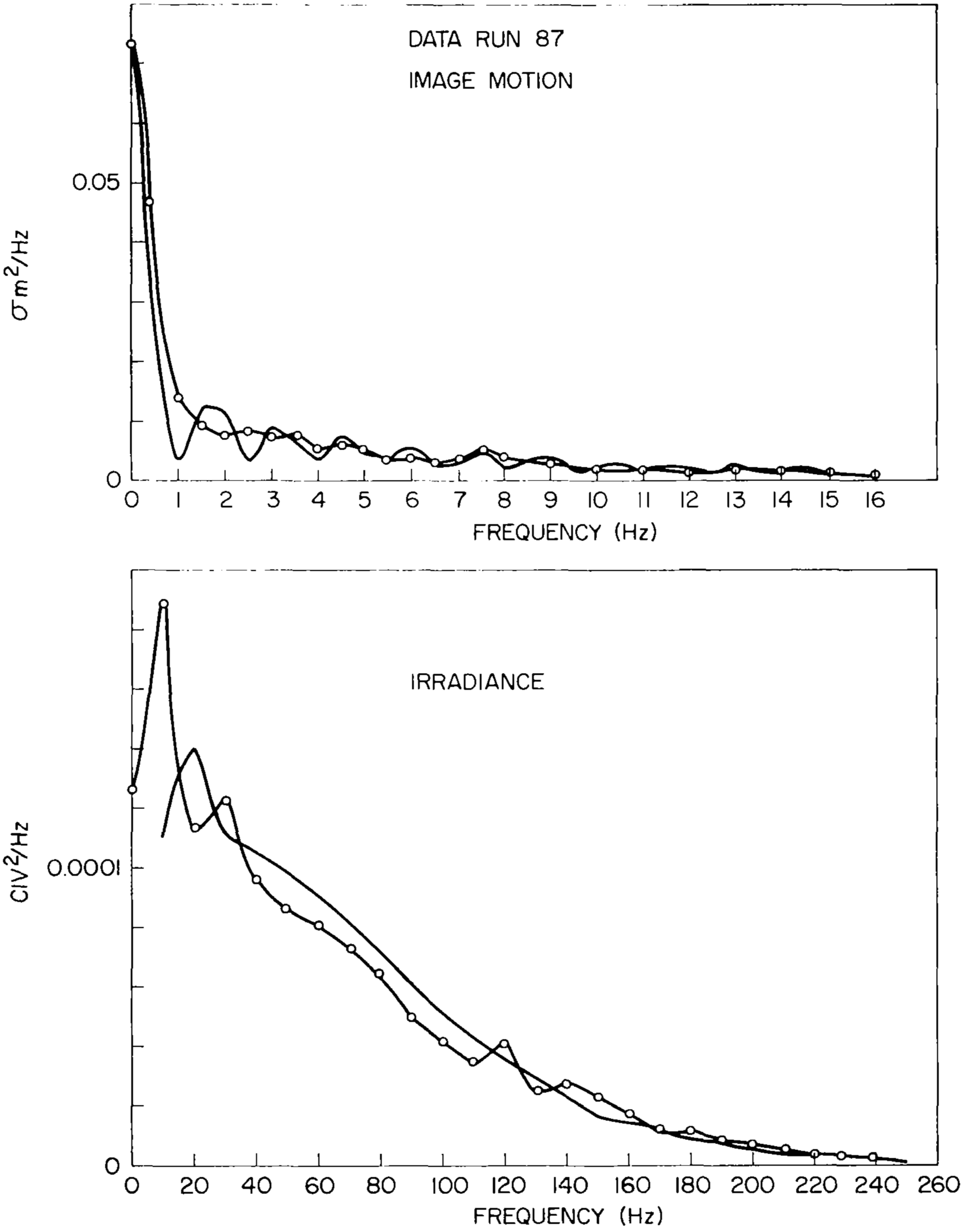

Figure 35. Spectral densities night 297

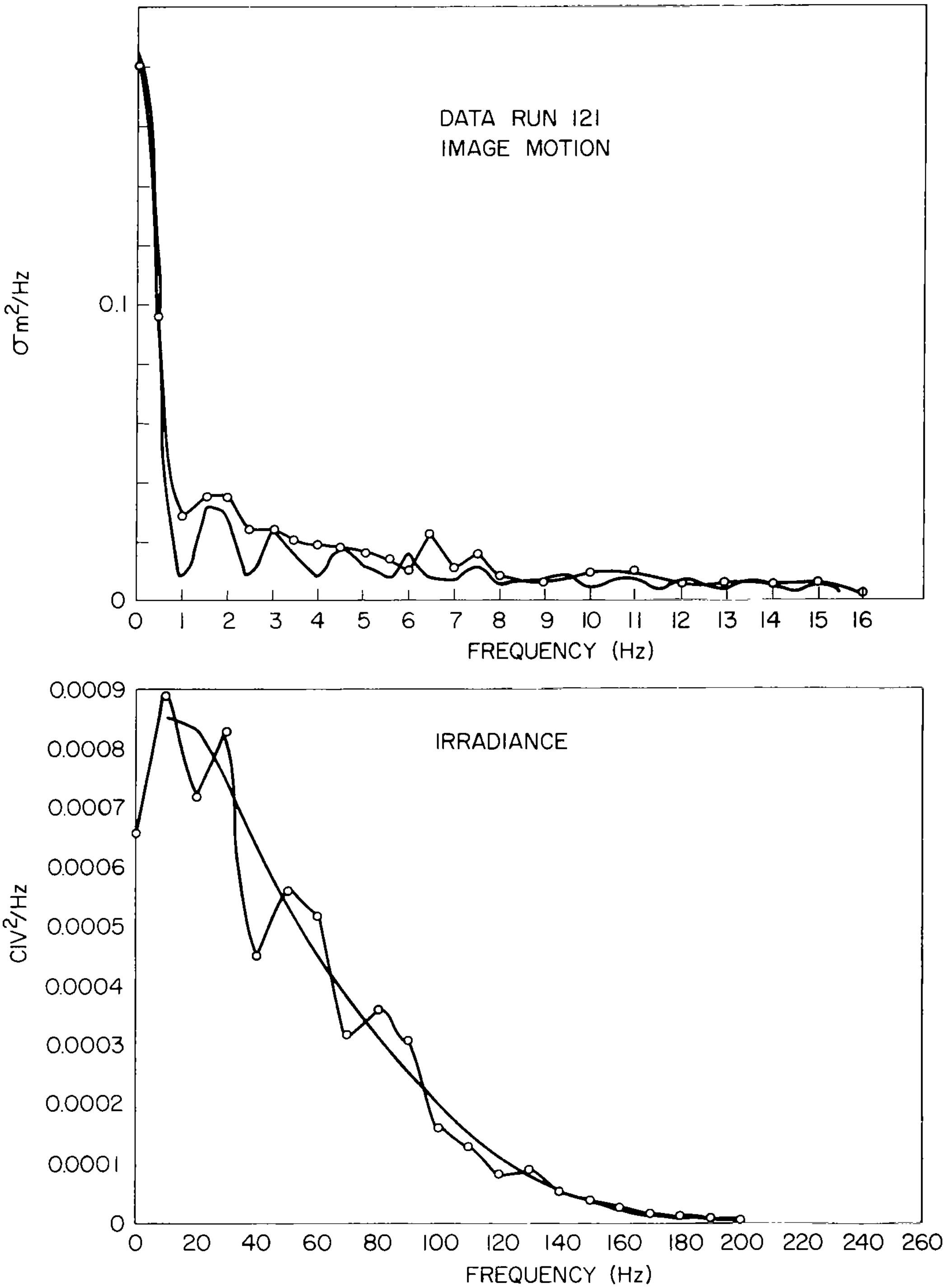

Figure 36. Spectral densities night 301

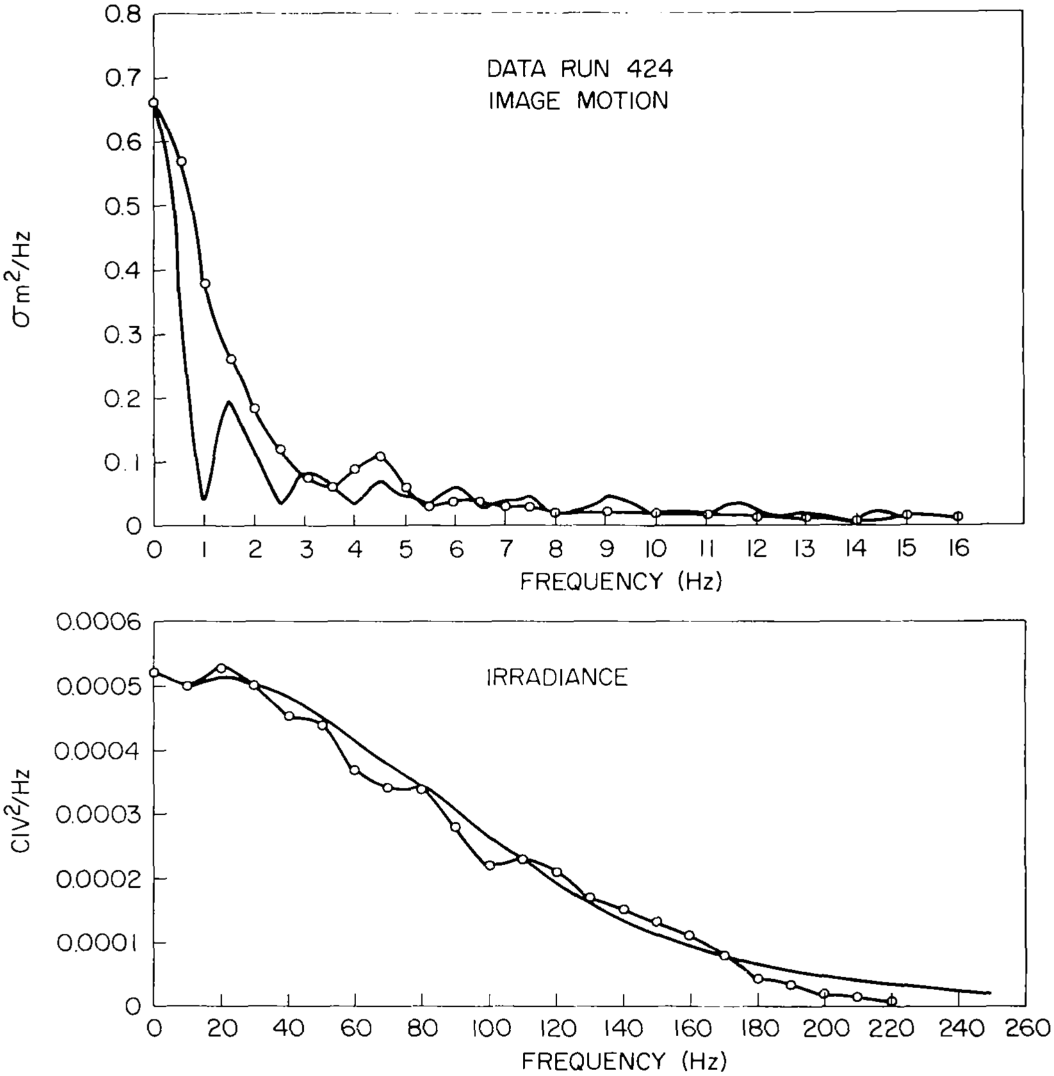

Figure 37. Spectral densities night 36

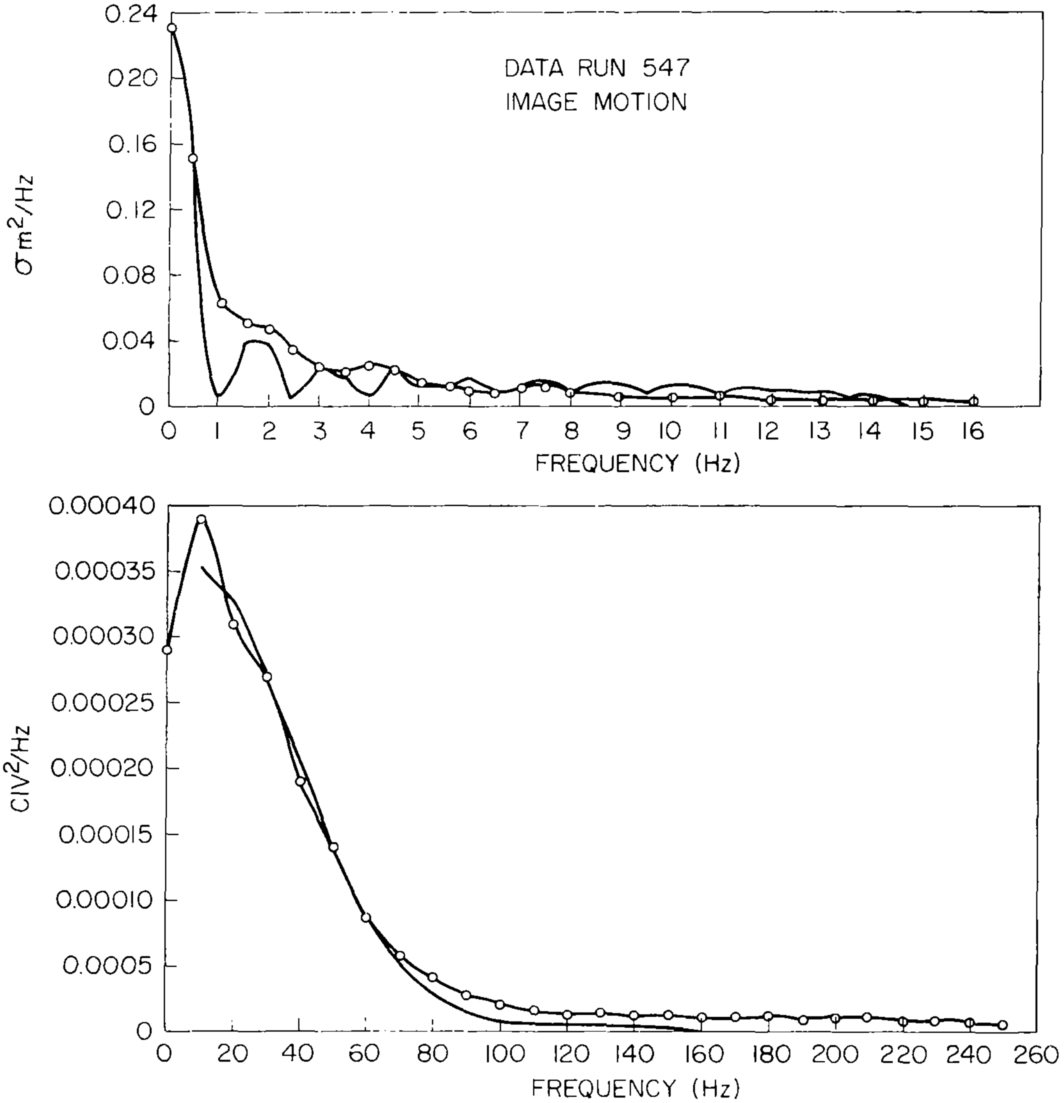

Figure 38. Spectral densities night 64

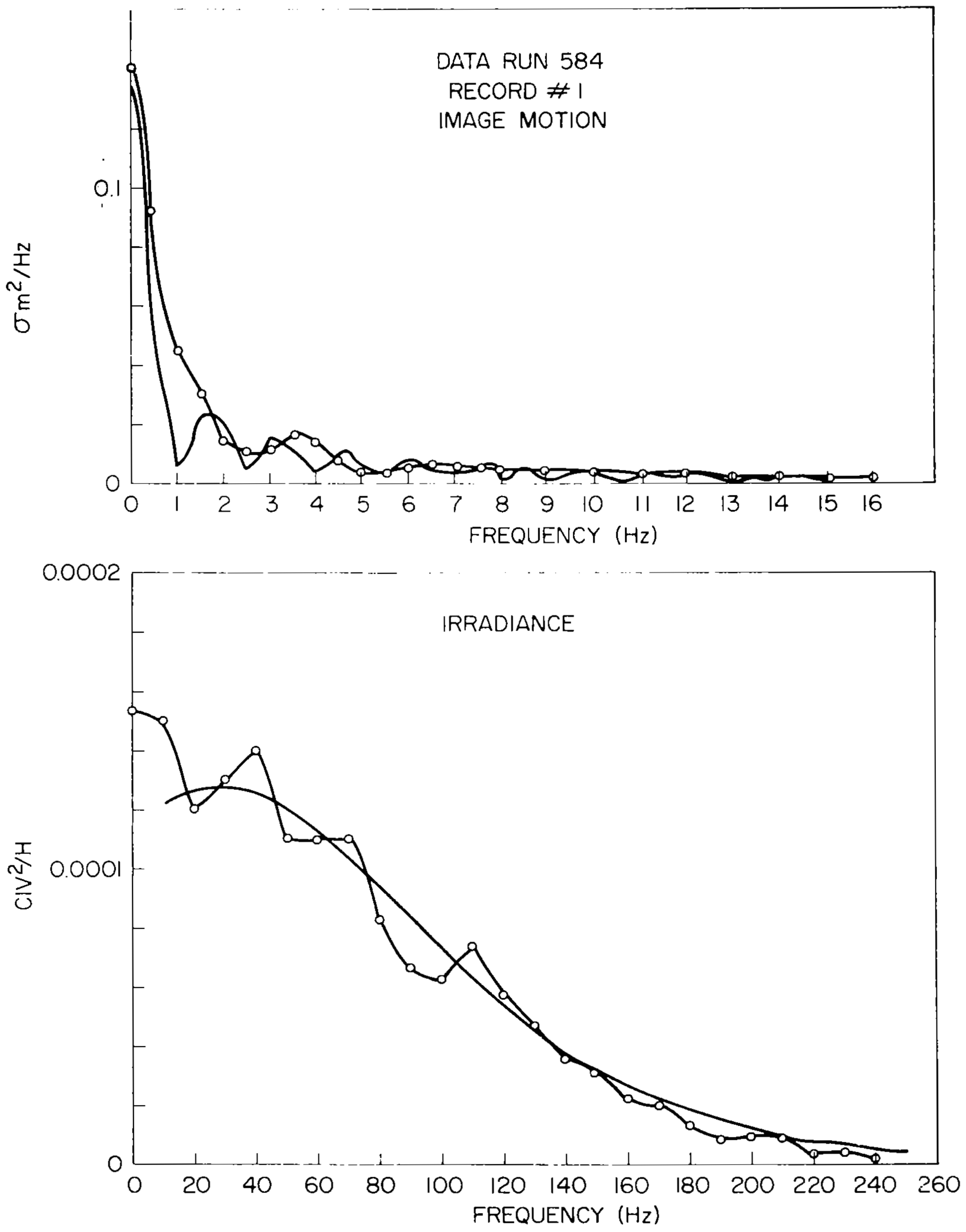

Figure 39. Spectral densities night 65

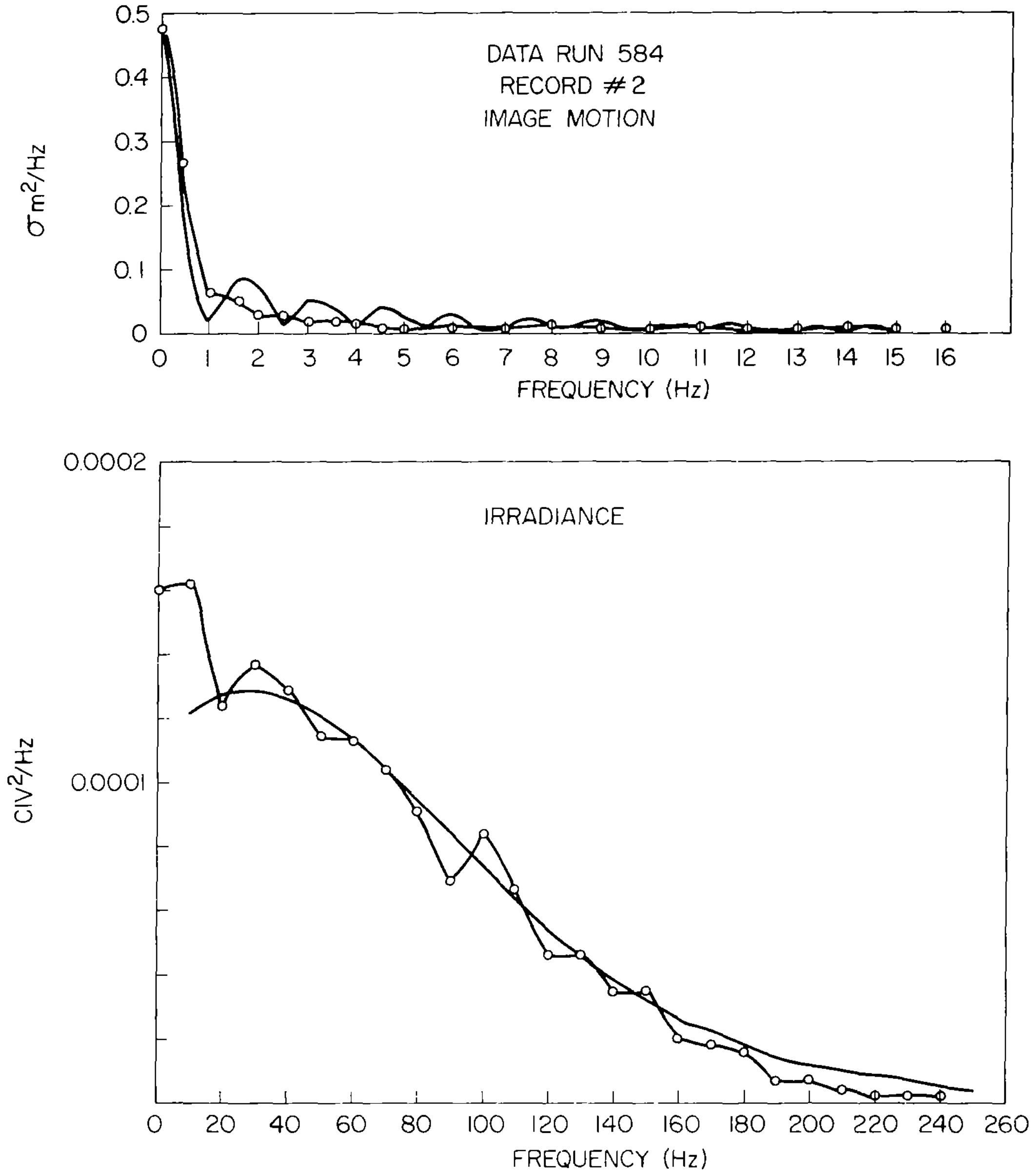

Figure 40. Spectral densities night 65

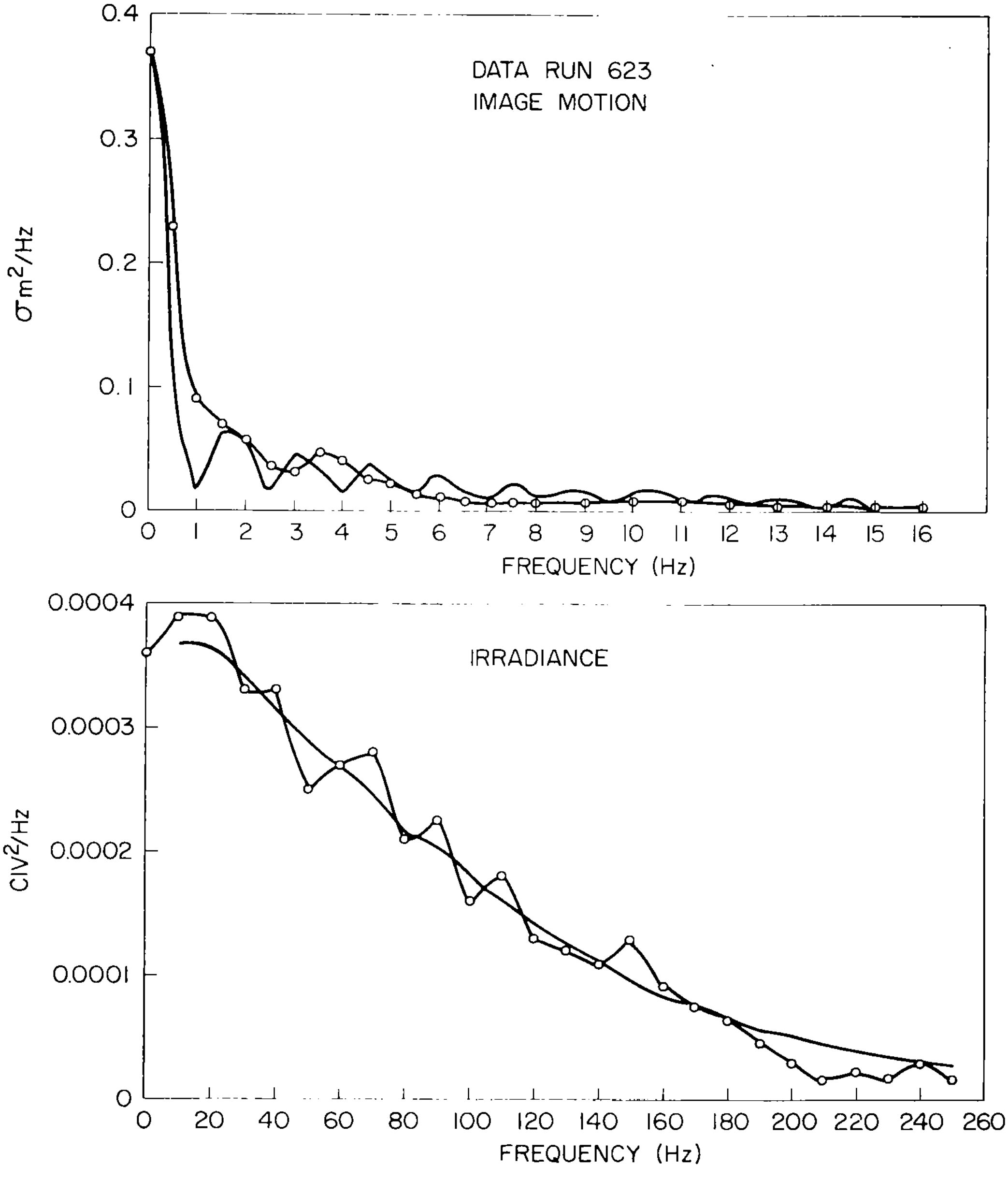

Figure 41. Spectral densities night 77

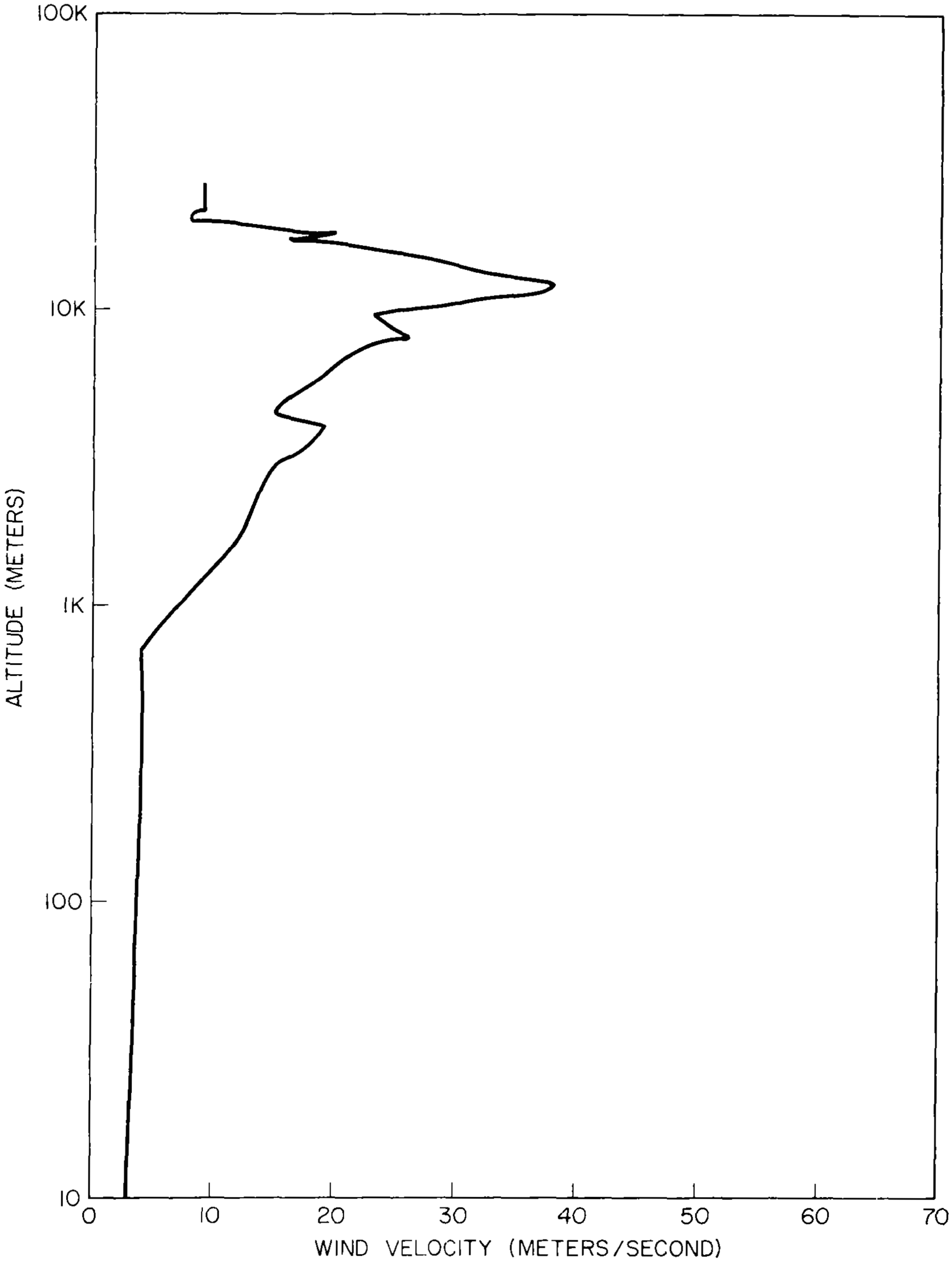

Figure 42. Vertical wind profile night 297

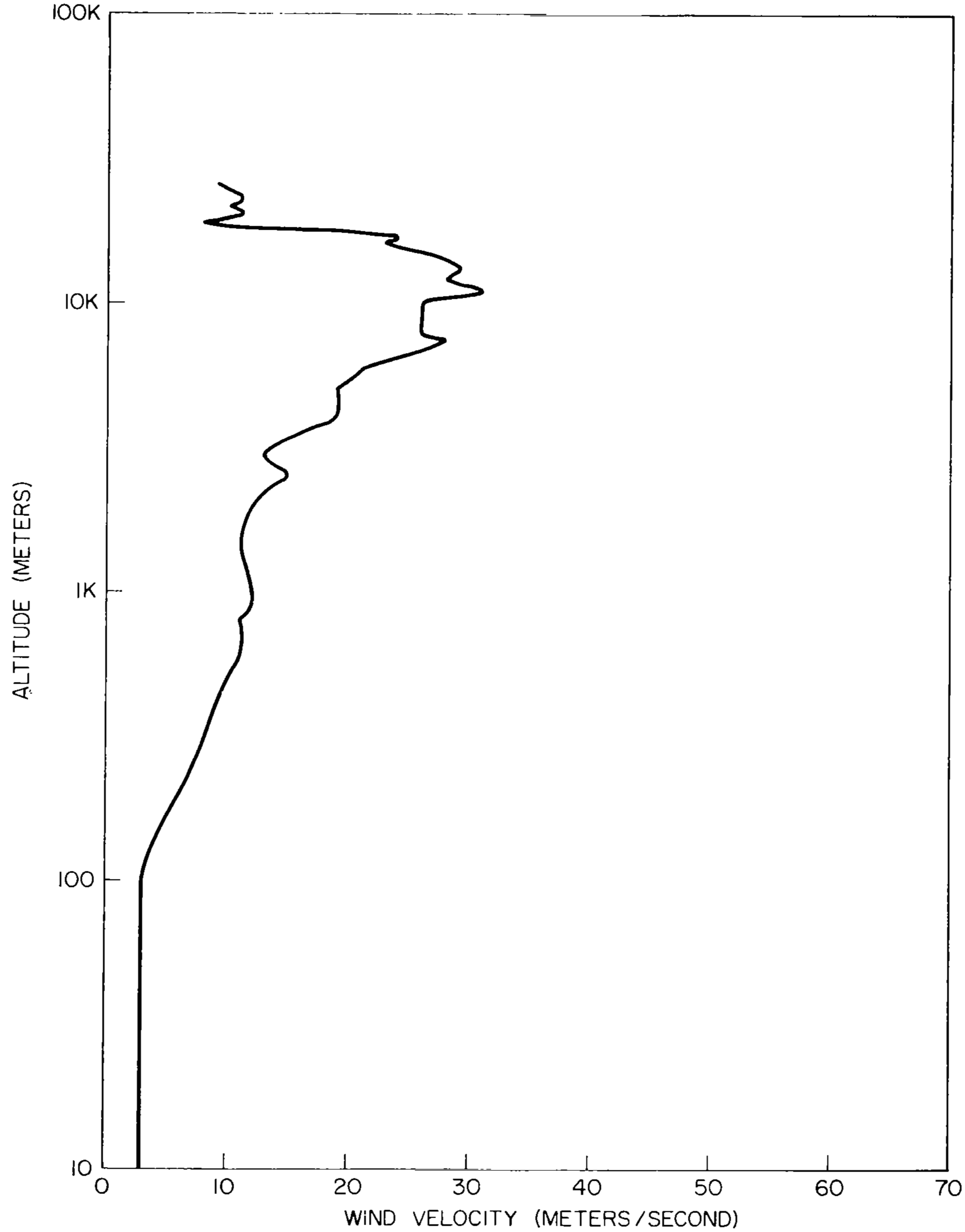

Figure 43. Vertical wind profile night 301

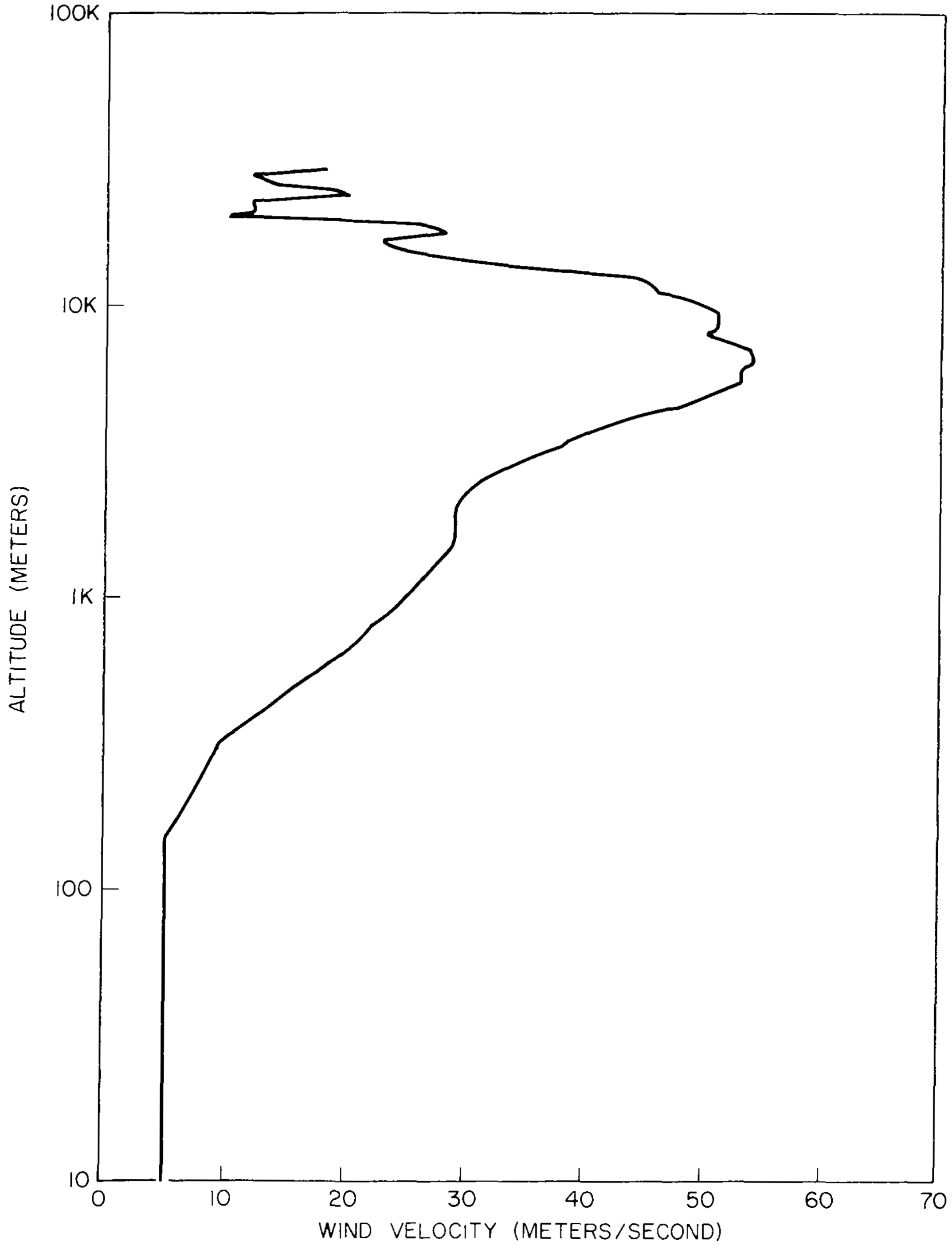

Figure 44. Vertical wind profile night 36

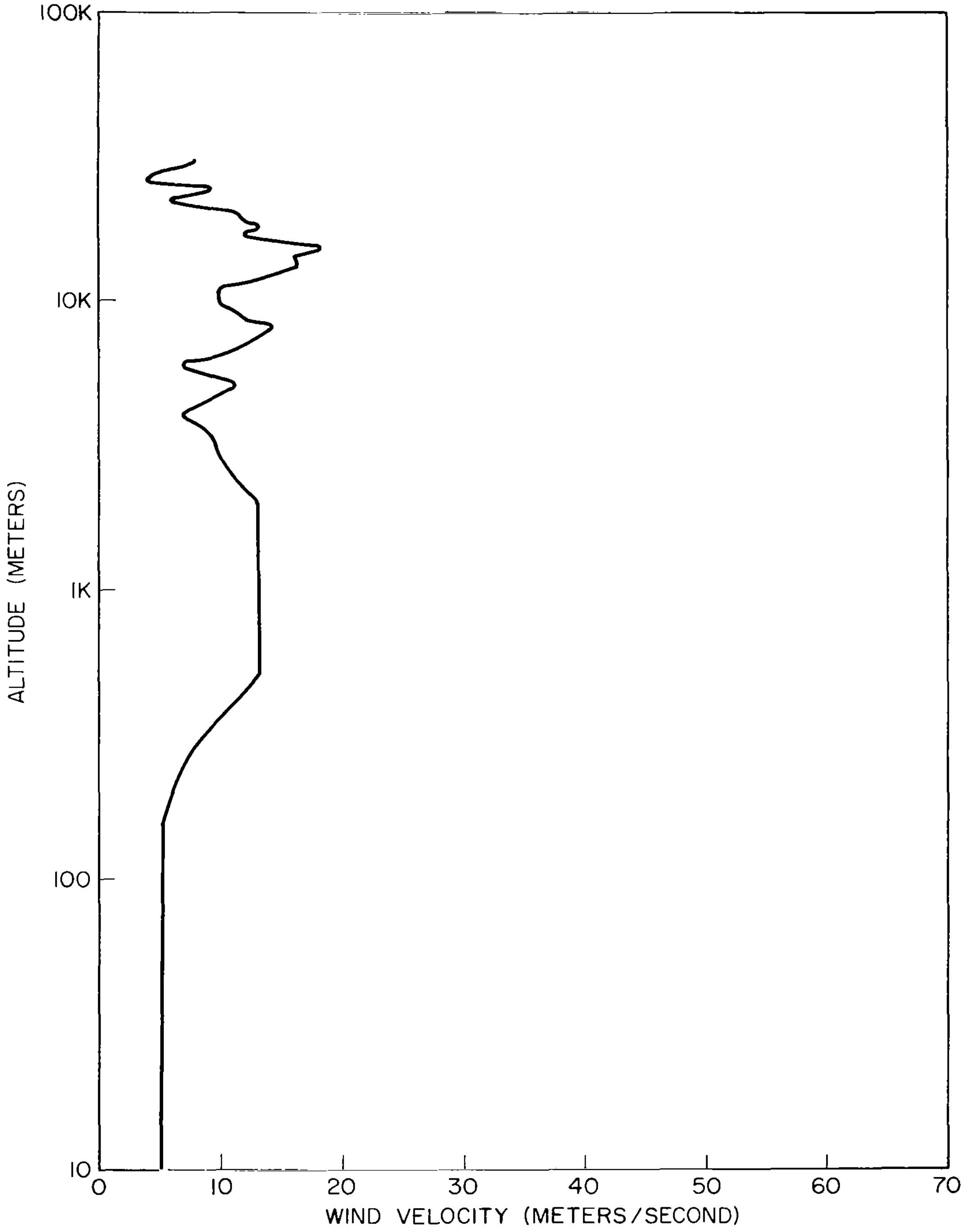

Figure 45. Vertical wind profile night 64

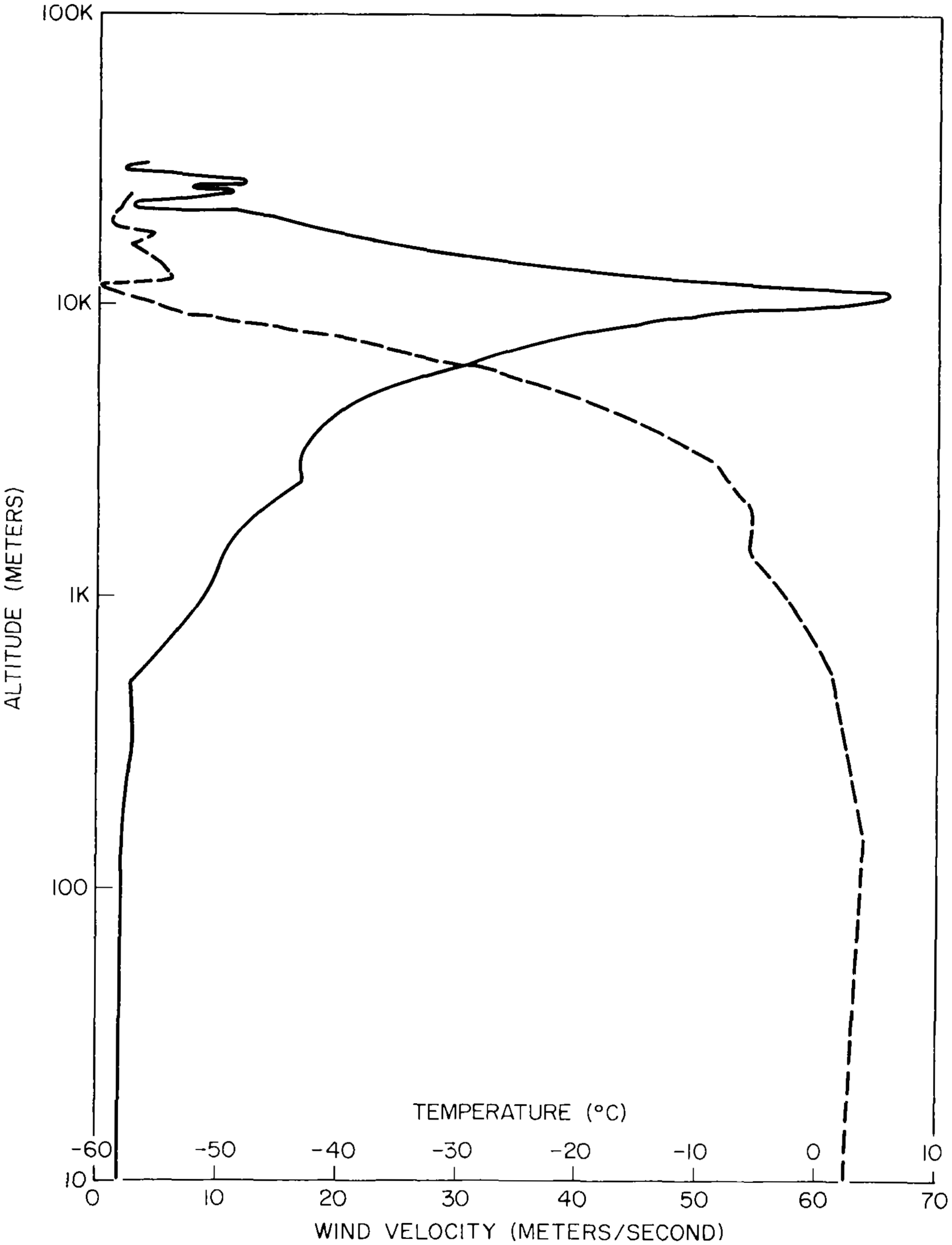

Figure 46. Vertical wind profile night 65

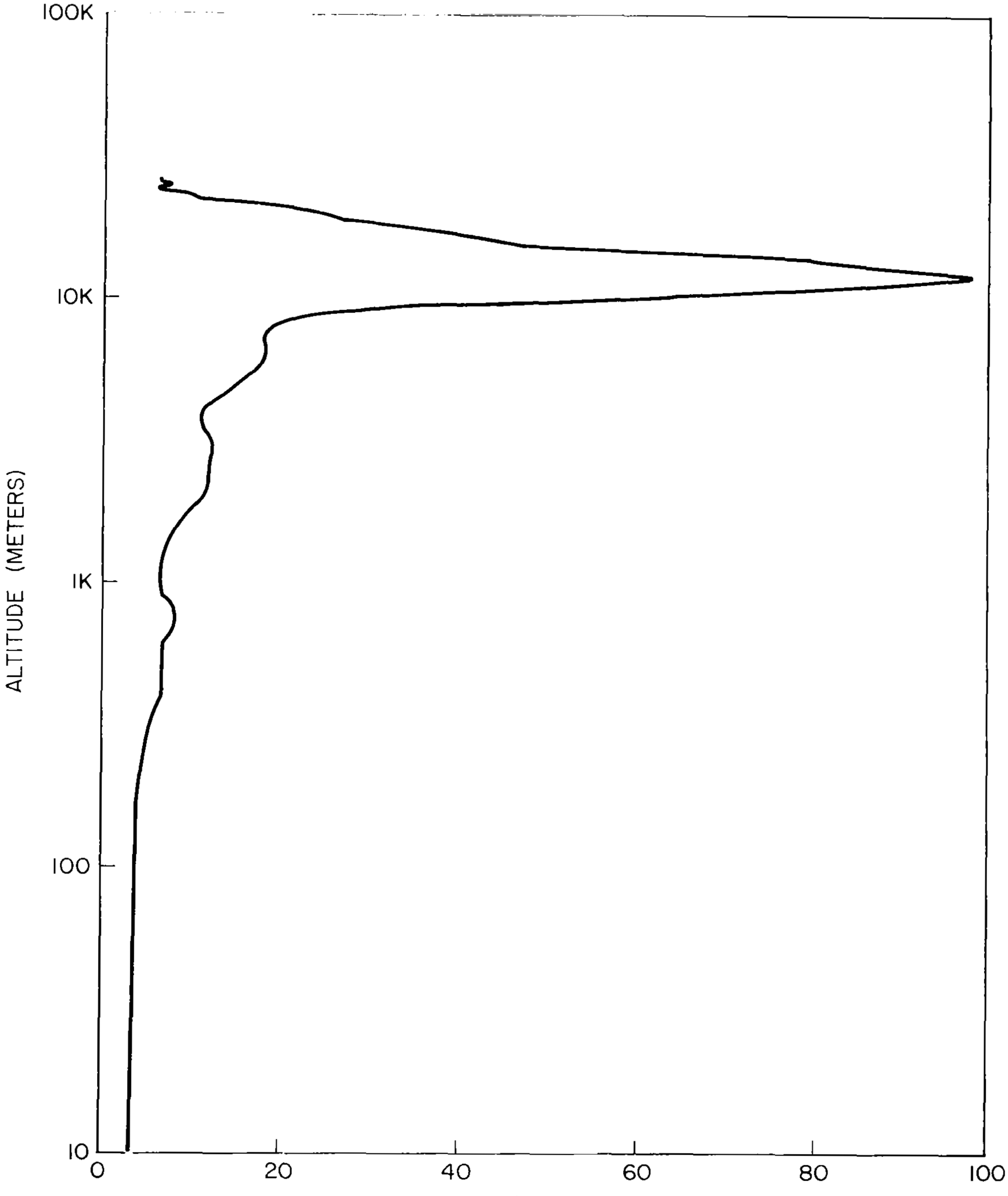

Figure 47. Vertical wind profile night 77

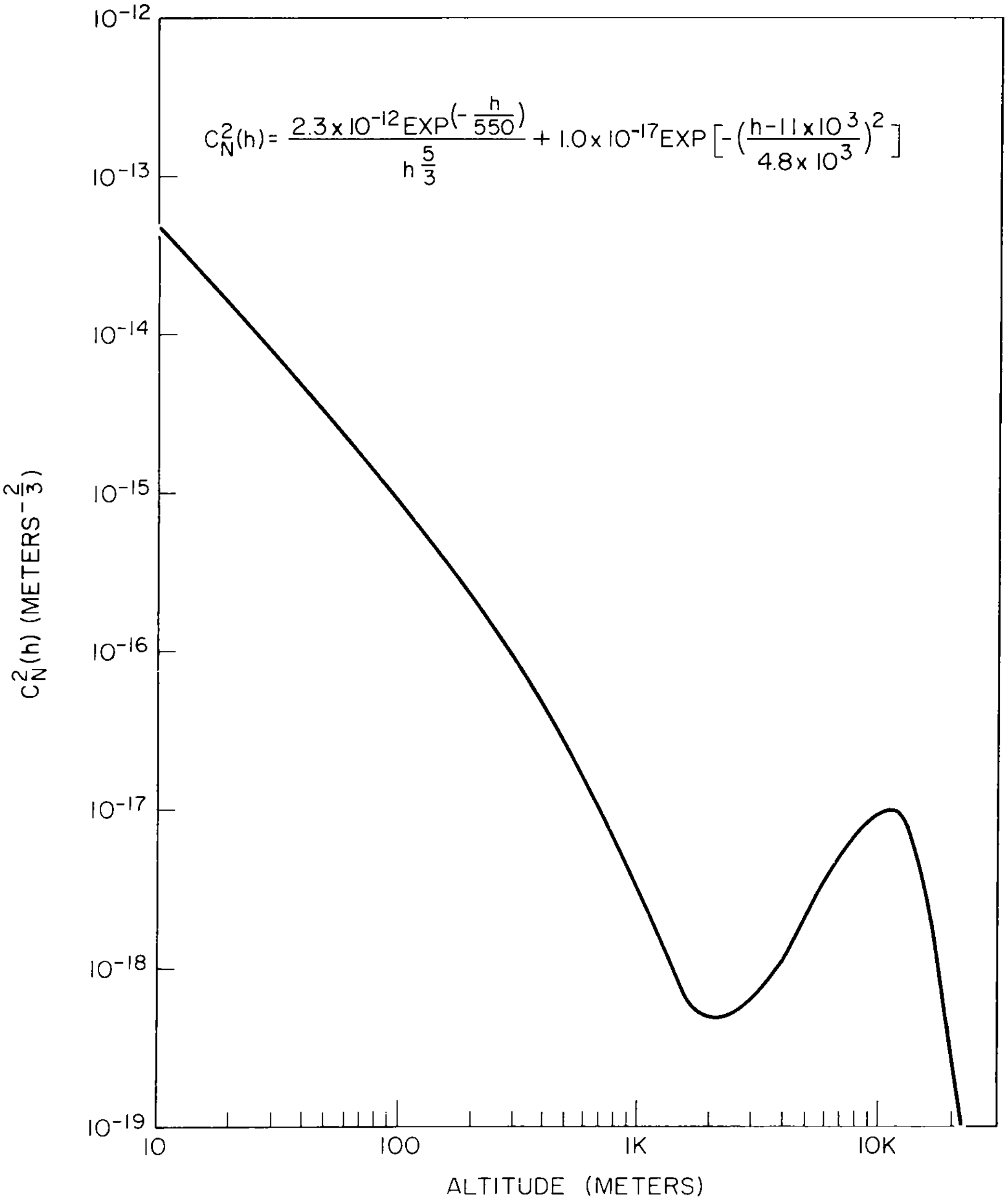

Figure 48. Turbulent profile night 297

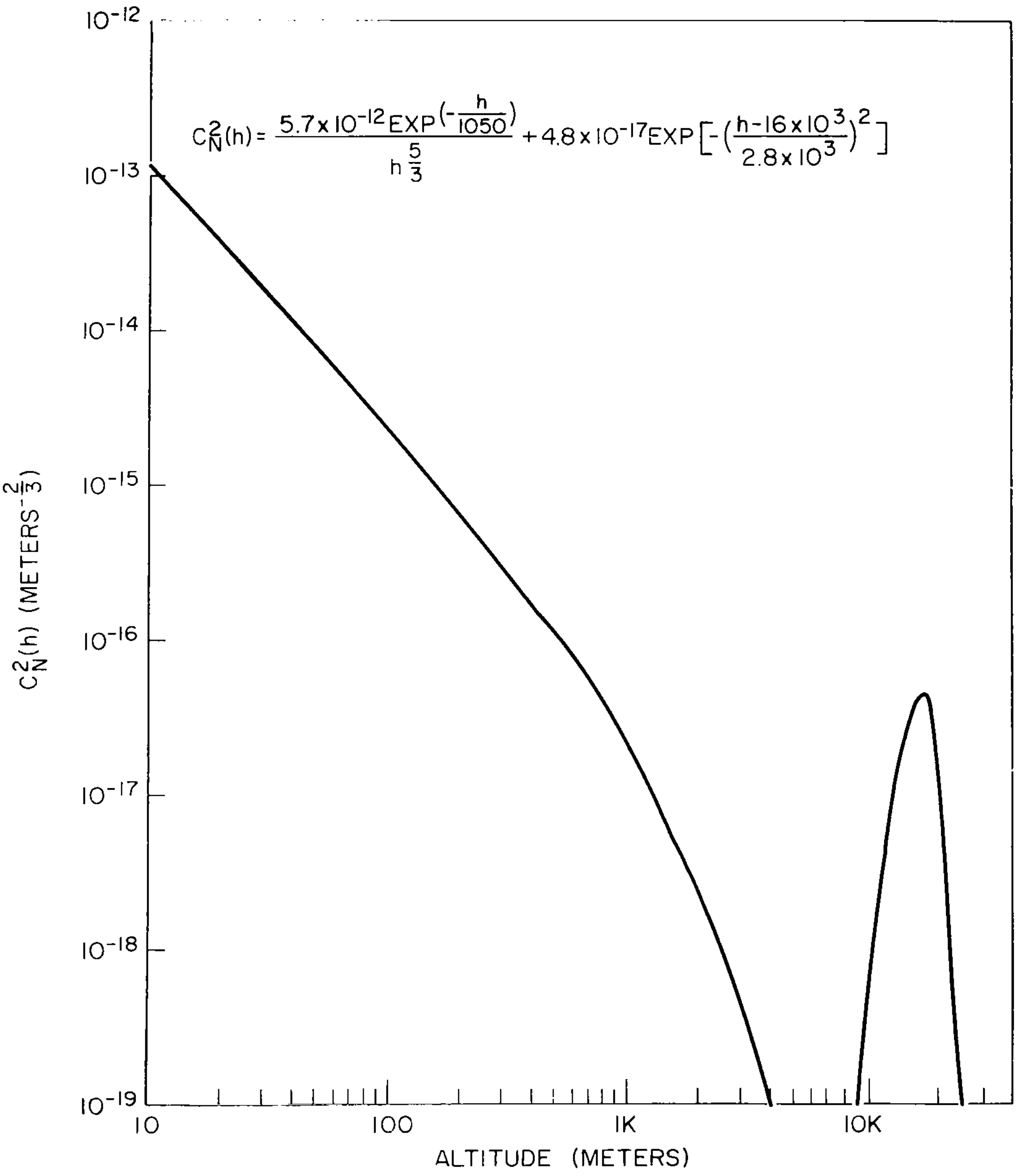

Figure 49. Turbulent profile night 301

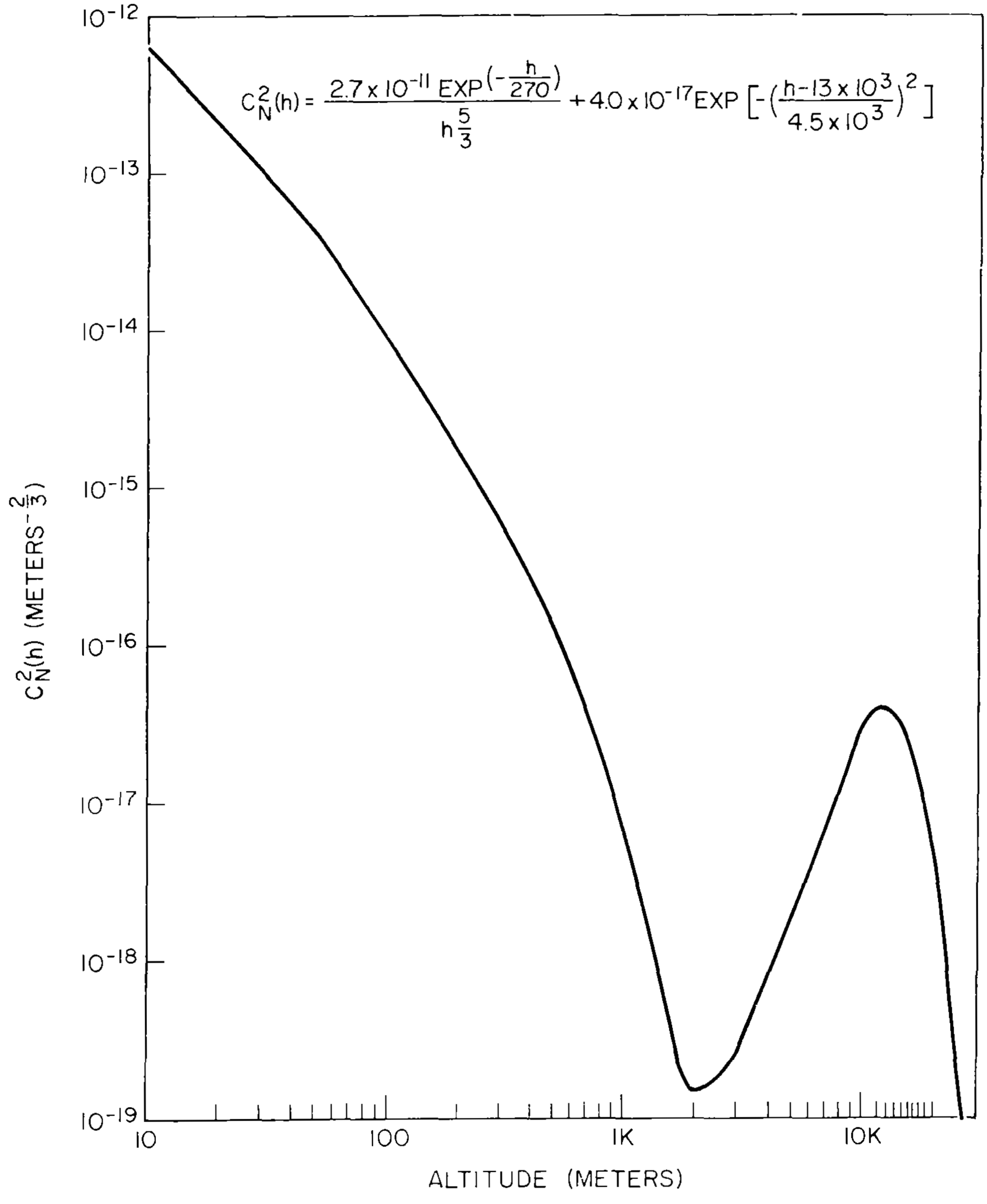

Figure 50. Turbulent profile night 36

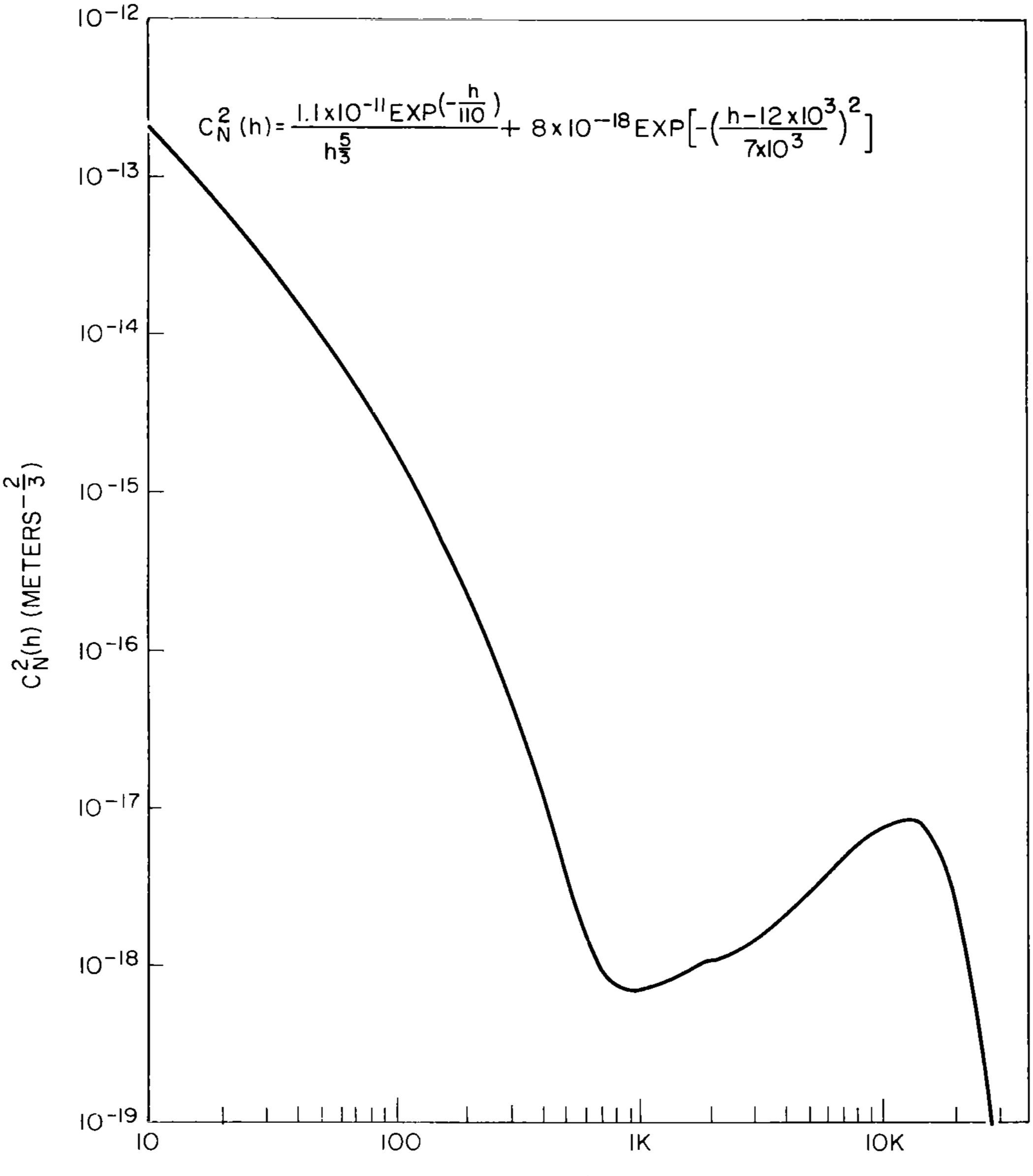

Figure 51. Turbulent profile night 64

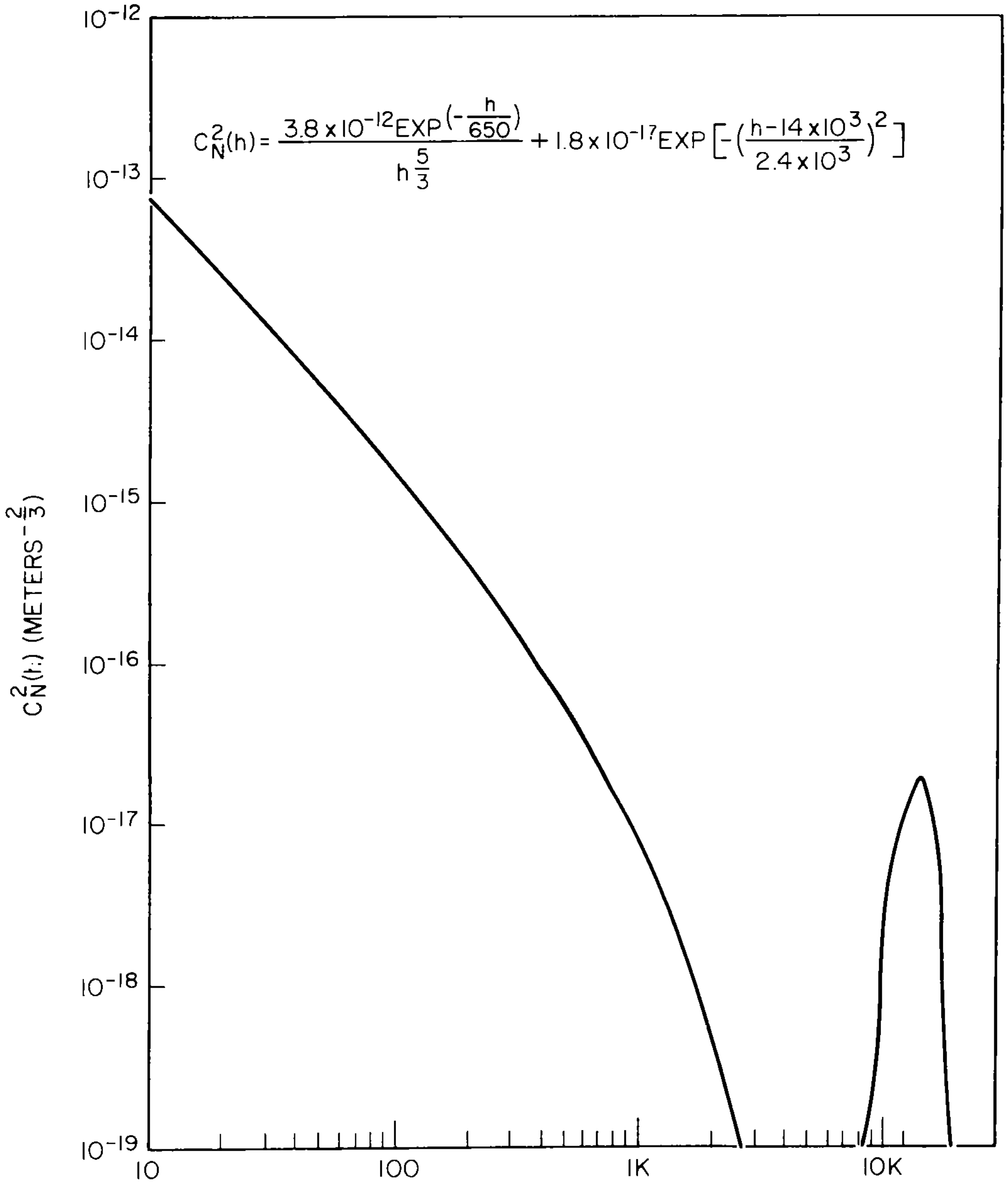

Figure 52. Turbulent profile night 65

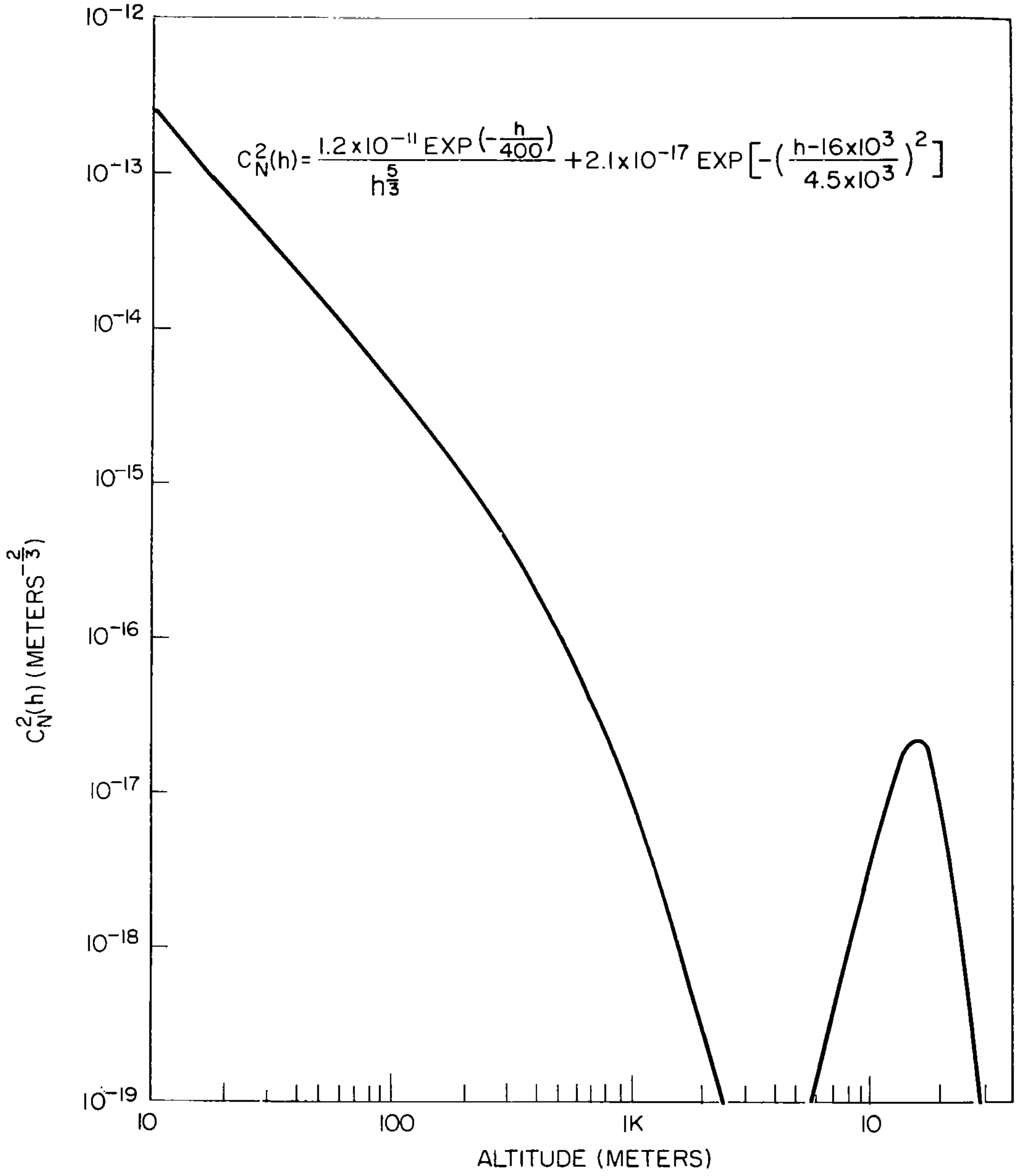

Figure 53. Turbulent profile night 77

Table 12

Data Runs for Calculation of Turbulent Profiles

Night	Data Run Number	Stellar Zenith Angle	Time		CIV^2	σ_m^2
			(hrs)	(mins)		
297	87	7°	23	56	.0127	.13
301	121	14°	09	05	.0596	.37
36	424	10°	00	45	.0635	1.5
64	547	11°	00	21	.0194	.44
65	584	18°	01	02	.0181	.52
77	623	14°	01	53	.0586	.77

value for autocorrelation analysis was allowed to be as high as one second. Yet at even this large lag value the computed autocorrelation showed a residual correlation of 10 to 20 percent. Note that the Fourier transform of a truncated function contains an additional $(\sin \omega f/\omega f)$ term due to the discontinuity. The variable ω is the reciprocal of the lag value (transform variable) at the discontinuity. This explains the observed one to two Hz damped oscillations. Autocorrelation of actual data fell to zero typically within 0.8 seconds. Thus the residual correlation was apparently due to the theoretical analysis, probably the interferometer assumption. Figure 54 is a plot of normalized autocorrelation computed for a single wind velocity, 2 meter/sec, under the interferometer assumption. Note the abrupt switch to nearly constant value for $R_\theta(\tau)$ at a lag value of 0.3 seconds. If contributions from all parts of the aperture were included instead of only two points at the extremes of the diameter, autocorrelation would be expected to go to zero due to an averaging effect. Part of the residual correlation may, however, be due to the 5/3 power

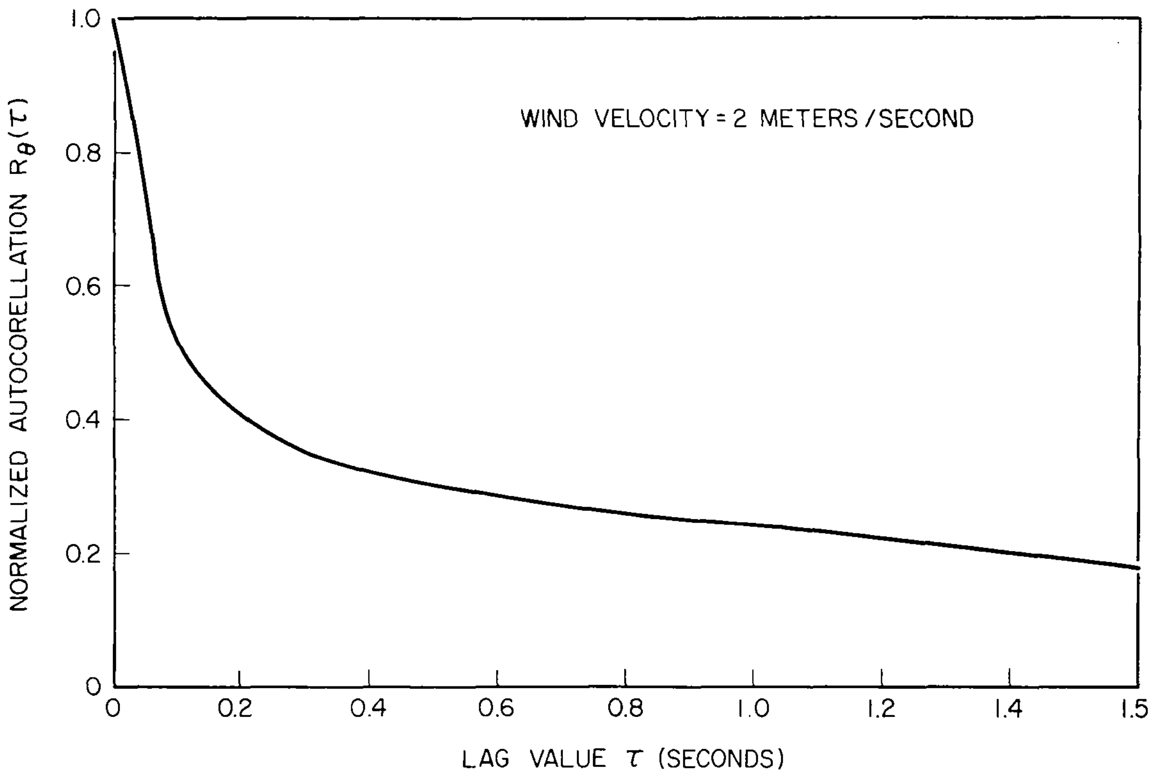

Figure 54. Theoretical autocorrelation for interferometer case

of radial separation in the phase structure function. This arises from the assumption of Obukhov-Kolmogorov turbulence spectra. For large separations, expressed in terms of lag value, and after conversion to image motion autocorrelation by division by $k^2(V_N \tau)^2$ the function decreases only as lag value to the negative one-third power. This results in a long tail to the theoretical autocorrelation function. Despite the oscillating behavior, the envelope of the fit spectral density followed the data well. For higher frequencies the oscillations tended to damp out.

Turbulent profile parameters determined by the fit to image motion data were A, H_0, and α. Early in this process, α was fixed at 5/3. This gave reasonable results and also corresponded to the best fit to the Hufnagel curve. Ground strength of turbulence, A, scaled the computed spectral density to give the correct value of σ_m^2. The exponential controlling parameter, H_0, determined power spectra shape. Typical values were in the range 100 meters to 1 kilometer. It was found that accuracy of fit to the data was not very sensitive to the value of H_0. The test statistic, sum of absolute differences, varied less than 10 percent over this range. This is in sharp contrast to irradiance differences which obtained a sharp minimum at the best fit values of B, H_1, and β. Thus image motion spectral density, at least in this present form, is unable to give an accurate measure of the shape of lower altitude turbulence or else the form of the model does not lend itself to a sensitive test. The dominance of the low-frequency peak may explain this behavior. Uncertainties concerned with the height of this peak and its effect on model parameters are discussed in Appendix B. The present analysis does suggest that image motion effects result primarily from a region of high turbulence within a few hundred meters of the ground. In general, the best value of H_0 was larger for conditions of low wind near the surface, indicating a need to include higher winds available at the higher altitudes. Apparently they were needed to construct the higher frequencies of image motion. Even so, turbulence beyond a few kilometers did not contribute sensibly to image motion. Although wind speeds at the tropopause showed a large variation from night to night, speeds for the first few kilometers were fairly uniform for most nights. This could explain why image motion spectral densities did not have significantly different shapes from night to night. The one exception is night 36 data. For this night, wind speeds as high as 30 meters per second were encountered in the first three kilometers with an unusual concentration of high winds in general at low altitudes. The corresponding image motion spectrum shows at least a factor of two increase in bandwidth and a lessening of the low-frequency peak.

It is apparent that a profile could be chosen to generate data for good fits to all irradiance spectral densities. The computer generated fit, while determined primarily by the low-frequency data, followed the high-frequencies very well and tended to represent the average of the data points all along the curve. Little attempt was made by the computer fit to follow the data fine structure since there were not enough degrees of freedom in the model. Comparison of consecutive 20 second records showed that the fine structure is for the most part a real effect and not statistical error. Note records one and two for data run 584 night 65 (Figures 39 and 40). It is possible that equipment vibration or electronic noise could account for this fine structure, although the appearance of fine structure at different frequencies on different nights and different times argues against this.

Perhaps the most striking feature is the maximum of irradiance spectral density that occurs between 10 and 20 Hz. In some cases, night 297 and night 65, the computer fit exhibits the same behavior. By printing out the tabulated $\mathfrak{I}\{\cdot\}$ function versus altitude for each frequency of interest, it was possible to determine which altitude ranges had the most weight in determining magnitude of spectral density at a particular frequency. Low-frequency behavior, including that interesting maximum, was found to be controlled for all wind profiles primarily by contributions from the very high altitudes (above 15 kilometers). Contributions to the middle and higher frequencies were increasingly weighted to those altitudes where wind velocity maximized. Since low-frequency components were relatively stronger in terms of CIV^2/Hz the turbulence profile was forced to maximize above the region of maximum wind. The maximum of $C_N^2(h)$ appeared at higher altitudes for nights with the largest maximum wind velocities (night 65 and 77) and the Gaussian "bump" was more sharply peaked. Low wind conditions represented by night 64 produced a broadly peaked $C_N^2(h)$ profile. This was to be expected since the lower wind was also more uniform with altitude.

CHAPTER VI

CONCLUDING REMARKS

The spectral density technique for estimating vertical profile of turbulence strength, $C_N^2(h)$, appears to be a significant improvement over previous methods based only on the magnitude of irradiance and image motion variance. The variance technique uses theoretical dependence on moments of the distribution. The spectral density technique also follows this approach with the moments being supplied by wind velocity as a function of altitude. A great deal more information is available, however, since wind velocity structure is not a simple power of altitude but provides a whole series of moments. Wind velocity values are accurately obtained from Weather Bureau rawinsonde flights adjacent to the site of stellar observations. These should be supplemented by local surface and near-surface measurements. By using near-zenith stellar observations the azimuth effects on wind velocity are eliminated. Thus wind velocity does not have to be a limiting factor in the determination of $C_N^2(h)$. The real limiting factors appear to be questions of statistical accuracy and lack of stationarity. In image motion there is an additional problem in separating instrumental from atmospheric effects.

In this report the theoretical base for stellar observations was reported and, where necessary, extended to account for operation of the Stellar Image Monitor apparatus. Certain major assumptions were involved in the theoretical base.

(1) Rytov "approximation" to the scalar wave equation.

(2) Local stationarity and isotropy of optical statistics.

(3) Obukhov - Kolmogorov turbulence spectra.

(4) Taylor's hypothesis regarding the relation of spatial and temporal frequencies through wind velocity.

Assumptions (2) and (3) are the most contested. Nonstationarity effects were noted in the data and resulted in larger error bars as well as a divergence of the data from the theoretical description. Departures from an Obukov-Kolmogorov turbulence spectrum could also be expected for the stable near-surface conditions at night.

Irradiance statistics seem to be well covered by the theory, although more attention is needed to the effects of aperture size and its interaction with zenith angle. Image motion statistics need more work, particularly in the description of image time autocorrelation function for finite apertures. It will be necessary to include phase effects from all regions of the given aperture. This will enable better computer fits to image motion spectral densities with a corresponding improvement in determination of $C_N^2(h)$ profile.

Data collection and reduction procedures should also be strengthened. In general the Stellar Image Monitor apparatus was found to be suitable for the types of data required in this thesis research. Irradiance statistics were measured with good accuracy and were available for the interesting range of aperture sizes near the correlation distance. The use of larger diameter optics would provide new information on image motion. In particular, a test of the weak $D^{-1/3}$ aperture dependence from the Obukhov-Kolmogorov theory could be made. It would also be desirable to record and analyze longer records of image motion data. This would provide more information on low-frequency behavior, narrow the statistical error bars, and tend to average out effects of short-term nonstationarity in the atmosphere. Alternately, if data were taken with higher surface wind velocities, spectral densities would broaden and apparent resolution would improve.

Computed $C_N^2(h)$ profiles as reported in the last chapter, although not incorporating all the accuracy and improvements suggested, do provide valuable information and new insight into the shape of the actual profile. The following conclusions can be drawn from this work:

(1) Nighttime contributions to $C_N^2(h)$ arise primarily from two turbulence regions, one near the earth's surface and another in the vicinity of the tropopause.

(2) Image motion variance and spectral density can be explained adequately by contributions in the first few kilometers above the surface. If an exponential distribution for turbulence is used, the 1/e point is typically a few hundred meters.

(3) The shape of irradiance spectral density and the structure of upper altitude winds require a definite contribution to $C_N^2(h)$ at altitudes near the tropopause. The assumption of a single maximum, Gaussian "bump", fits the data well for different wind profiles and total turbulent strengths.

(4) Parameters of the Gaussian fit tended to give a low, wide maximum for low wind conditions and a sharper, higher peak for high winds. This brings out the association of wind velocity and strength of turbulence implicit in the spectral density theory. Typical maximum values of $C_N^2(h)$ near the tropopause were near $1 \times 10^{-17}\ m^{-2/3}$. These were about three to four orders of magnitude less than the ground strength values, but supplied essentially all the contribution to irradiance statistics.

It is apparent that statements in further detail cannot be made without increasing the model complexity and/or increasing data accuracy. To get most value out of refinements like this it would also be necessary to determine the appropriate number of degrees of freedom of the model, given data accuracy and given the method of model testing.

ACKNOWLEDGMENTS

I would like to express sincere thanks to Dr. Douglas G. Currie, Department of Physics and Astronomy, University of Maryland, for guidance in both the theoretical and experimental aspects of this research.

I also wish to thank Dr. Henry H. Plotkin and Mr. Walter J. Carrion, Optical Systems Branch, Goddard Space Flight Center, for their encouragement and Mr. Peter O. Minott, Dr. Michael W. Fitzmaurice, and Mr. John J. Degnan, Optical Systems Branch, for many helpful discussions.

Additional thanks are due Mr. Sol H. Genatt, Optical Systems Branch, for much help with the stellar observations and Mr. John W. Larmer and Mr. David A. Grolemund, Bendix Field Corporation, for their many contributions to the optics and electronics of the Stellar Image Monitor apparatus.

Goddard Space Flight Center
National Aeronautics and Space Administration
Greenbelt, Maryland, August 18, 1970
125-22-08-01-51

REFERENCES

1. Lord Rayleigh: Philosophical Mag., Vol. 36, 1893.

2. Ratcliffe, J. A.: Reports on Progress in Physics, Vol. 19, Stonebridge Press (Bristol), 1956, pp. 188-267.

3. Chandrasekhar, S.: A Statistical Basis for the Theory of Stellar Scintillation, Monthly Notices Roy. Astron. Soc., Vol. 112, No. 5, May 1952, pp. 475-483.

4. Ramsay, J. V.: On the Transfer Function of a Non-Uniform Atmosphere, Optica Acta, Vol. 6, No. 4, Oct. 1959, pp. 344-353.

5. Handbook of Geophysics, MacMillan Co. (New York), 1960.

6. Obukhov, A. M.: On the Distribution of Energy in the Spectrum of Turbulent Flow, Doklady Akad. Nauk SSSR, Vol. 32, No. 4, 1941, pp. 19.

7. Kolmogorov, A. N.: Dissipation of Energy in Locally Isotropic Turbulence, Doklady Akad. Nauk SSSR, Vol. 32, 1941.

8. Krechmer, S. I.: Methods for Measuring Microfluctuations of Wind Velocity and Temperature in the Atmosphere, Trudy Geofiz. Inst. Akad. Nauk SSSR, Vol. 24, 1954, pp. 43.

9. Lumley, J. L., and Panofsky, H. A.: The Structure of Atmospheric Turbulence, John Wiley and Sons (New York), 1964.

10. Hufnagel, R. E.: An Improved Model Turbulent Atmosphere, Appendix 3, Restoration of Atmospherically Degraded Images, Vol. 2, Woods Hole Summer Study, July 1966.

11. Fried, D. L.: Optical Heterodyne Detection of an Atmospherically Distorted Signal Wavefront, Proc. IEEE, Vol. 55, No. 1, Jan. 1967, pp. 127-137.

12. Chernov, L. A. (R. A. Silverman, Trans.): Wave Propagation in a Random Medium, McGraw-Hill (New York), 1960.

13. Beckmann, P.: Signal Degradation in Laser Beams Propagated Through a Turbulent Atmosphere, Radio Science Jour. of Res., Vol. 69D, No. 4, Apr. 1965, pp. 629-640.

14. Hodara, H.: Laser Wave Propagation Through the Atmosphere, Proc. IEEE, Vol. 54, No. 3, Mar. 1966, pp. 368-375.

15. Taylor, L. S.: Validity of Ray-Optics Calculations in a Turbulent Atmosphere, J. Optical Soc. Am., Vol. 58, No. 1, Jan. 1968, pp. 57-59.

16. Kerr, J. R.: Optical Propagation in a Turbulent Atmosphere, Technical Proposal, Oregon Graduate Center for Study and Research (1968).

17. Reiger, S. H.: Starlight Scintillation and Atmospheric Turbulence, Astronomical J., Vol. 72, No. 7, 1967, pp. 395-406.

18. Young, A. T.: Photometric Error Analysis, VIII The Temporal Power Spectrum of Scintillation, Applied Optics, Vol. 8, No. 5, May 1969, pp. 869-891.

19. Tatarski, V. I. (R. A. Silverman, Trans.): Wave Propagation in a Turbulent Medium, McGraw-Hill (New York), 1961.

20. Fried, D. L.: Optical Effects of Atmospheric Turbulence, Final Report (C7-805/401, ASTIA No. N67-36560), Autonetics Div., North American Aviation, Inc., Apr. 1967. 161

21. Freid, D. L.: Test of the Rytov Approximation, J. Optical Soc. Am., Vol. 57, No. 2, Feb. 1967, pp. 268-269.

22. Tatarski, V. I.: reference 19, ch. 12.

23. Beran, M. J.: Propagation of a Spherically Symmetric Mutual Coherence Function Through a Random Medium, IEEE Trans. on Antennas and Propagation, Vol. 15, Jan. 1967, pp. 66-69.

24. Hufnagel, R. E., and Stanley, N. R.: Modulation Transfer Function Associate with Image Transmission through a Turbulent Media, J. Optical Soc. Am., Vol. 54, No. 1, Jan. 1964, pp. 52-61.

25. Fried, D. L.: Diffusion Analysis for the Propagation of Mutual Coherence, J. Optical Soc. Am., Vol. 58, No. 7, July 1968, pp. 961-969.

26. Fried, D. L.: reference 20, pp. 33-75.

27. Fitzmaurice, M. W., and Bufton, J. L.: Measurement of Log-Amplitude Variance, J. Optical Soc. Am., Vol. 59, No. 4, Apr. 1969, pp. 462-463.

28. Fried, D. L., and Cloud, J. D.: Propagation of an Infinite Plane Wave in a Randomly Homogeneous Medium, J. Optical Soc. Am., Vol. 56, No. 12, Dec. 1966, pp. 1667-1676.

29. Yura, H. T., and Lutomirski, R. F.: *Aperture Averaging of Optical Scintillation*, Technical Memorandum (RM-5902-ARPA, ASTIA No. AD 688411), Rand Corp., Santa Monica, California, Apr. 1969.

30. Protheroe, W. M.: *Preliminary Report on Stellar Scintillation*, Scientific Report 4 (AF 19 (604) - 41, ASTIA No. AD 56040), Physics and Astronomy Dept., Ohio State Univ., Nov. 1954.

31. Gossard, E. E.: Power Spectra of Temperature Humidity and Refractive Index from Aircraft and Tethered Balloon Measurements, *IRE Trans. on Antennas and Propagation*, Vol. 8, Mar. 1960, pp. 186-201.

32. Hufnagel, R. E.: *Optical Propagation Study*, Technical Report (RADC-TR-65-511, ASTIA No. AD 476244), Perkin-Elmer Corp., Jan. 1966.

33. Hosfeld, R.: Comparison of Stellar Scintillation with Image Motion, *J. Optical Soc. Am.*, Vol. 44, No. 4, Apr. 1954, pp. 284-288.

34. Kolchinskii, I. G.: *Optical Instability of the Earth's Atmosphere According to Stellar Observations*, Technical Translation (ACIC-TC-1395, ASTIA No. AD 682665), Academy of Sciences of the Ukrainian SSR, Main Astronomical Observatory, Feb. 1969.

35. Fried, D. L.: Statistics of a Geometric Representation of Wavefront Distortion, *J. Optical Soc. Am.*, Vol. 55, No. 11, Nov. 1965, pp. 1427-1435.

36. Fried, D. L.: Optical Resolution Through a Randomly Inhomogeneous Medium for Very Long and Very Short Exposures, *J. Optical Soc. Am.*, Vol. 56, No. 10, Oct. 1966, pp. 1372-1379.

37. Hufnagel, R. E.: On the Mean Short Term Blur, Appendix 4, Restoration of Atmospherically Degraded Images, Vol. 2, Woods Hole Summer Study, July 1966.

38. Ramsey, J. V., and Kobler, H.: A Stellar Image Monitor, Observatory, Vol. 82, June 1962, pp. 107-111.

39. Lindberg, P. J.: Measurement of Contrast Transmission Characteristics in Optical Image Formation, Optica Acta, Vol. 2, Sept. 1954, pp. 80-89.

40. Coulman, C. E.: Dependence of Image Quality on Horizontal Range in a Turbulent Atmosphere, J. Optical Soc. Am., Vol. 56, No. 9, Sept. 1966, pp. 1232-1238.

41. Coulman, C. E.: Optical Image Quality in a Turbulent Atmosphere, J. Optical Soc. Am., Vol. 55, No. 7, July 1965, pp. 806-812.

42. Lawrence, R. S., Ochs, G. R., and Cifford, S. F.: Measurements of Atmospheric Turbulence Relevant to Optical Propagation, J. Optical Soc. Am., Vol. 60, No. 6, June, 1970, pp. 826-830.

43. Fitzmaurice, M. W., and Bufton, J. L.: Wavelength Dependence of Laser-Beam Scintillation, J. Optical Soc. Am., Vol. 59, No. 1, Jan. 1969, pp. 7-10.

44. Hulett, H. R.: Turbulence Limitations in Photographic Resolution of Planet Surfaces, J. Optical Soc. Am., Vol. 57, No. 11, Nov. 1967, pp. 1335-1338.

45. Clodman, J., Morgan, G. M., and Ball, J. T.: High Level Turbulence, Final Report (AF 19(604) - 5208, AFCRL-TR-60-408), Dept. of Meteorology and Oceanography, New York Univ., Sept. 1960.

46. Peskoff, A.: Theory of Remote Sensing of Clear-Air Turbulence Profiles, J. Optical Soc. Am., Vol. 58, No. 8, Aug. 1968, pp. 1032-1039.

47. Fried, D. L.: Remote Probing of the Optical Strength of Atmospheric Turbulence and of Wind Velocity, Proc. IEEE, Vol. 57, No. 4, Apr. 1969, pp. 415-420.

APPENDIX A

IMAGE INTENSITY PROFILE AND OPTICAL TRANSFER FUNCTION

The diffraction image formed in an optical system is characterized by a normalized intensity distribution called the optical spread function,

$$S = S(x, y; x', y'; \lambda) = S(\vec{x}, \vec{x}'; \lambda), \tag{A1}$$

light flux in $(\lambda + d\lambda)$, which originates in $d\vec{x}'$ and passes through the optics to fall on $d\vec{x}$, divided by $d\vec{x}\, d\vec{x}'\, d\lambda$, where

$\vec{x}$ = two-dimensional vector in object plane

and

$\vec{x}$ = two-dimensional vector in image plane.

The optical spread function is assumed to be time independent and normalized such that

$$\int_{-\infty}^{\infty} S(\vec{x}; \vec{x}'; \lambda)\, d\vec{x} = 1.$$

Use of a transfer function to describe the optical system requires the existence of an isoplanatism patch, an area in the object field over which wave aberrations are effectively constant. This enables the optical spread function to be written

$$S = S(\vec{x} - \vec{x}'; \lambda). \tag{A2}$$

The optical transfer function, $T(\vec{f})$, is defined as the Fourier transform of S. The transform variable is $\vec{f}$, two-dimensional spatial frequency, so that

$$T(\vec{f}) = \int_{-\infty}^{\infty} S(\vec{x} - \vec{x}\,'; \lambda) \exp\left[-2\pi i \vec{f} \cdot (\vec{x} - \vec{x}\,')\right] d\vec{x} \tag{A3}$$

and

$$S(\vec{x} - \vec{x}\,'; \lambda) = \int_{-\infty}^{\infty} T(\vec{f}) \exp\left[2\pi i \vec{f} \cdot (\vec{x} - \vec{x}\,')\right] d\vec{f}\,. \tag{A4}$$

The object intensity distribution, $O(\vec{x}\,')$, can be written in terms of a Fourier integral of spatial frequencies[16] as

$$O(\vec{x}\,') = \int_{-\infty}^{\infty} W(\vec{f}) \exp(2\pi i \vec{f} \cdot \vec{x}\,')\, df \tag{A5}$$

and

$$W(\vec{f}) = \int_{-\infty}^{\infty} O(\vec{x}\,') \exp(-2\pi i \vec{f} \cdot \vec{x}\,')\, d\vec{x}\,', \tag{A6}$$

where

$W(\vec{f})$ = Fourier transform of $O(\vec{x}\,')$.

Image intensity distribution, $I(\vec{x})$, is by definition of the optical spread function, just the convolution of $S(\vec{x} - \vec{x}\,'; \lambda)$ with $O(\vec{x}\,')$, that is,

$$I(\vec{x}) = \int_{-\infty}^{\infty} S(\vec{x} - \vec{x}\,'; \lambda)\, O(\vec{x}\,')\, d\vec{x}\,'. \tag{A7}$$

Equation (A4) for S and equation (A7) for I allow image intensity to be expressed in terms of the transfer function by

$$I(\vec{x}) = \int_{-\infty}^{\infty} S(\vec{x} - \vec{x}\,'; \lambda)\, O(\vec{x}\,')\, d\vec{x}\,' \tag{A8}$$

$$= \iint_{-\infty}^{\infty} T(\vec{f}) \exp\left[2\pi i \vec{f} \cdot (\vec{x} - \vec{x}\,')\right] d\vec{f}\, O(\vec{x}\,')\, d\vec{x}\,'$$

$$= \iint_{-\infty}^{\infty} T(\vec{f}) \exp\left[2\pi i \vec{f} \cdot (\vec{x} - \vec{x}')\right] O(\vec{x}')\, d\vec{x}'\, d\vec{f}$$

$$= \int_{-\infty}^{\infty} T(\vec{f}) \exp(2\pi i \vec{f} \cdot \vec{x}) \int_{-\infty}^{\infty} O(\vec{x}') \exp(-2\pi i \vec{f} \cdot \vec{x}')\, d\vec{x}'\, d\vec{f}$$

$$= \int_{-\infty}^{\infty} T(\vec{f}) \exp(2\pi i \vec{f} \cdot \vec{x})\, W(\vec{f})\, d\vec{f}\, . \tag{A9}$$

If the object is a point source, $O(\vec{x}') = \delta(\vec{x}')$ and

$$W(\vec{f}) = \int_{-\infty}^{\infty} \delta(\vec{x}') \exp(-2\pi i \vec{f} \cdot \vec{x}')\, d\vec{x}' = 1\, .$$

Thus,

$$I(\vec{x}) = \int_{-\infty}^{\infty} T(\vec{f}) \exp(2\pi i \vec{f} \cdot \vec{x})\, d\vec{f}\, . \tag{A10}$$

The variable, $T(\vec{f})$, is, in general, complex and can be written in terms of a modulus and complex argument as

$$T(\vec{f}) = M(\vec{f}) \exp\left[2\pi i\, \phi(\vec{f})\right].$$

For real symmetric images the transfer function is real, $T(\vec{f}) = M(\vec{f})$, and

$$I(\vec{x}) = \int_{-\infty}^{\infty} M(\vec{f}) \exp(2\pi i \vec{f} \cdot \vec{x})\, d\vec{f}\, . \tag{A11}$$

A transformation to polar coordinates for both $\vec{x}$ and $\vec{f}$ allows I to be expressed in a form more suitable for computation. That is, given

$$I(x, y) = \iint_{-\infty}^{\infty} M(f, g) \exp\left[2\pi i (fx + gy)\right] df\, dg\, ,$$

and letting

$$f = \omega \cos\phi , \qquad x = r\cos\theta ,$$

and

$$g = \omega \sin\phi , \qquad y = r\sin\theta ,$$

then,

$$I(r, \theta) = \int_0^\infty \int_0^{2\pi} M(\omega, \phi) \exp\left[2\pi\, i\, r\, \omega \cos(\phi - \theta)\right] \omega\, d\phi\, d\omega .$$

Symmetry arguments require that I be θ independent and M be ϕ independent. Therefore,

$$I(r) = \int_0^\infty M(\omega)\, \omega \int_0^{2\pi} \exp(2\pi\, i\, r\, \omega \cos\phi)\, d\phi\, d\omega ,$$

or

$$\left[I(r) = 2\pi \int_0^\infty M(\omega)\, \omega J_0(2\pi\, r\, \omega)\, d\omega \right] . \qquad \text{(A12)}$$

This is the final form relating image intensity and the transfer function.

The theoretical transfer function for a diffraction-limited optical system with circular aperture has been computed and results in

$$M(\omega) = \frac{2}{\pi} \left\{ \cos^{-1} \frac{\lambda}{D}\, \omega - \frac{\lambda\omega}{D} \left[1 - \left(\frac{\lambda\omega}{D} \right)^2 \right]^{1/2} \right\} , \qquad \text{(A13)}$$

where

λ = wavelength,

D = aperture diameter,

and

ω = spatial frequency in cycles per arc second.

Substitution of this expression into equation (A12) yields the familiar Airy pattern for a diffraction-limited lens:

$$\frac{I(r)}{I_0} = \left[\frac{2\, J_1(\pi D r/\lambda F)}{\pi D r/\lambda F} \right]^2 ,$$

where

F = system focal length.

In angular measure this becomes

$$\frac{I(S)}{I_0} = \left[\frac{2\,J_1\left(\frac{\pi D S}{\lambda}\right)}{\frac{\pi D S}{\lambda}}\right]^2 , \qquad \text{(A14)}$$

with S in radians. This expression is plotted in Figure 25.

APPENDIX B

IMAGE MOTION LOW-FREQUENCY BEHAVIOR

Image motion variance as measured in this research often exhibits larger variability among adjacent data runs than can be explained by electronic signal-to-noise ratios or statistical sample size error bars. In examination of image motion spectral density it is seen that the greatest variability as well as the greatest fraction of total variance (typically 30 to 50 percent) resides in the low frequencies below one Hz. In the consecutive records shown in Figures 39 and 40 this low frequency peak is seen to change by a factor of four. Previously (Chapter IV) this has been attributed to nonstationarity in the atmosphere. This may very well be the case, for gusts of wind mixed with periods of calm could conceivably alter the total variance and low-frequency spectrum quite rapidly. In addition, a change in refraction contributed by the total atmospheric path would show up as a low-frequency effect.

As resolution bandwidth of the spectral density analysis was increased from the nominal value of one Hz the large contribution at low frequencies was found to be concentrated in a smaller region, typically within 0.3 Hz of the origin, and to increase in height. Contributions in this region may be due entirely to an instrument effect, tracking of the star by the telescope drive. The standard computer analysis described in Chapter IV removed any linear component in the image motion data by least squares fitting a straight line to the data. This was done to account for drift in the tracking. It is also possible that improper tracking could contribute curvature to image motion data. This very point is discussed by Kolchinskii[34]. He concludes that, while small, the curvature component could be significant for stars away from the meridian and in the case of image wander caused by changes in total refraction.

To test this assertion, a quadratic term was also removed in a least squares fashion from a sample of data showing a strong low-frequency peak, data run 558 of night 64. This procedure reduced the peak a factor of two and resulted in a more believable shape for spectral density, i.e., a gentle rolling off as zero frequency was approached. Removal of higher order terms did not further significantly reduce the peak, indicating that only the linear and quadratic terms were appreciable in the data. It is still difficult to state how much of this effect is truly an instrument effect. The data could very well contain atmospheric contributions at these low frequencies that would be attenuated by removal of even the linear term. In fact, the theoretical prediction of the Obukhov-Kolmogorov spectrum is that for low winds (less than one meter per second) significant correlation exists to lag values beyond one second of time. This indicates significant contribution at frequencies below one Hz. Evidence of this is supplied in the relative ease with which a computed spectral density was constructed for a reasonable $C_N^2(h)$ profile to fit the low-frequency peak.

For present purposes suffice it to say that for resolution bandwidth of one Hz the spectral density values at zero and 0.5 Hz should be considered accurate only to within a factor of 5 to 10, and are probably a little high in general. The net effect of higher than actual peak on model parameters for $C_N^2(h)$ is to require a smaller H_0 and larger A. This is equivalent to concentrating turbulence at lower altitudes where wind speed is lower and low-frequency image motion can be enhanced. Add to this the large uncertainty and variability of low altitude winds and it is difficult to make more than order of magnitude estimates of the low-altitude turbulence distribution.

APPENDIX C

IMAGE SIZE CALCULATION

The image size determination of equation (75) is greatly simplified mathematically if the approximation of exp $(-cf^2)$ is made for the true exp $(-cf^{5/3})$ MTF factor. To test this approximation a numerical integration of equation (75) was carried out for both cases. This integration was performed for one value of the parameter C which generated an MTF close to that of stellar data. With f expressed in cycles per arc second the value used for C was two. Numerical integration was performed on a digital computer through a standard integration subroutine. The subroutine employed the trapezoidal rule together with Romberg's extrapolation method. Although the formal integration extended from zero to infinity the MTF exponential factor in the integrand enabled the numerical procedure to be truncated at a reasonable value for spatial frequency. Thus the actual integration was carried out over the range zero to 50 cycles per arc second.

The integrals were performed successively for different values of the variable S, arc seconds, and image profiles were constructed for both cases. The square law approximation resulted in a slightly wider image with less intensity in the tail. Despite this behavior the two curves followed each other quite closely and the total error in rms image width was only 7 percent, with the square law case giving the higher value for width. Thus it appears reasonable to employ the square law approximation.

NASA-Langley, 1971 —— 23